Measurement of the Neutron-Neutron Scattering Length

Messung der Neutron-Neutron-Streulänge
Zur Erlangung des Grades eines Doktors der Naturwissenschaften (Dr. rer. nat.)
Genehmigte Dissertation von Marco Knösel aus Lindenfels i. Odw.
Tag der Einreichung: 25.04.2023, Tag der Prüfung: 31.05.2023

1. Gutachten: Prof. Dr. rer. nat. Thomas Aumann
2. Gutachten: Prof. Alexandre Obertelli, Ph.D.
Darmstadt, Technische Universität Darmstadt – D17

TECHNISCHE
UNIVERSITÄT
DARMSTADT

Physics Department
Institut für Kernphysik

Measurement of the Neutron-Neutron Scattering Length
Messung der Neutron-Neutron-Streulänge

Accepted doctoral thesis by Marco Knösel

1. Review: Prof. Dr. rer. nat. Thomas Aumann
2. Review: Prof. Alexandre Obertelli, Ph.D.

Date of submission: 25.04.2023
Date of thesis defense: 31.05.2023

Darmstadt, Technische Universität Darmstadt – D17

Bitte zitieren Sie dieses Dokument als:
URN: urn:nbn:de:tuda-tuprints-241185
URL: http://tuprints.ulb.tu-darmstadt.de/id/eprint/24118

Jahr der Veröffentlichung der Dissertation auf TUprints: 2023

Erklärungen laut Promotionsordnung

§8 Abs. 1 lit. c PromO

Ich versichere hiermit, dass die elektronische Version meiner Dissertation mit der schriftlichen Version übereinstimmt.

§8 Abs. 1 lit. d PromO

Ich versichere hiermit, dass zu einem vorherigen Zeitpunkt noch keine Promotion versucht wurde. In diesem Fall sind nähere Angaben über Zeitpunkt, Hochschule, Dissertationsthema und Ergebnis dieses Versuchs mitzuteilen.

§9 Abs. 1 PromO

Ich versichere hiermit, dass die vorliegende Dissertation selbstständig und nur unter Verwendung der angegebenen Quellen verfasst wurde.

§9 Abs. 2 PromO

Die Arbeit hat bisher noch nicht zu Prüfungszwecken gedient.

Darmstadt, 25.04.2023

Marco Knösel

Abstract

The $^1S_0$ neutron-neutron scattering length a_{nn} characterizes the two-neutron interaction at low energies and therefore is a fundamental quantity in many broad research fields such as nuclear structure physics. There were numerous attempts to determine the scattering length in the past decades, some of them with contradicting results, also including more recent ones. The precise and accurate measurement of a_{nn} still remains challenging and to this day, in contrast to the proton-proton scattering length, no direct measurement via n-n scattering is feasible. In this work, a new approach to measure a_{nn} is presented that makes use of relativistic radioactive ion beams created *at high energies,* in order to investigate n-n scattering *at low energies*.

The experiment will be conducted at the "Radioactive Ion Beam Factory" of the research institute RIKEN in Japan and aims at the investigation of the free two-neutron system using the knockout reactions ^{6}He(p,$p\alpha$)$2n$ and t(p,$2p$)$2n$. Furthermore, single-neutron events resulting from the d(p,$2p$)n reaction will serve for calibration and validation purposes.

In the case of the ^{6}He(p,$p\alpha$)$2n$ reaction, the n-n scattering length is accessible by comparison of the experimentally determined two-neutron relative-energy spectrum to calculations using the effective field theory for halo nuclei, called "Halo EFT". For the t(p,$2p$)$2n$ reaction, the corresponding calculations will instead be based on pionless EFT. For the purpose of this experiment, the new high-resolution neutron detector HIME is currently developed and constructed at the “Institut für Kernphysik” in Darmstadt, Germany. A prototype of that detector has already been built at RIKEN. In this work, it was taken in operation and tested with electronics from “Gesellschaft für Schwerionenforschung” in Darmstadt.

All reactions will take place in inverse kinematics with a beam energy of about $200\,\mathrm{MeV/nucleon}$, resulting in two-neutron systems that move with relativistic velocity in the laboratory system. Thereby, a nearly constant neutron-detection efficiency in the relative-energy region of interest can be achieved. The measurements will be kinematically complete, which allows for a strong background suppression. In order to reach sufficient resolution, the relative-energy spectrum will be reconstructed by direct invariant-mass measurement, requiring coincident two-neutron detection. The analysis methods for the reconstruction of the primary interaction points in the neutron detector, which have been developed in this work, are tested and discussed with simulated data. Due to the limited resolution, efficiency and acceptance of the experimental setup, the measured relative-energy distribution cannot be compared directly to theoretical calculations. Different approaches of solving this issue are presented and discussed with simulated data as well.

Zusammenfassung

Die ${}^1S_0$-Neutron-Neutron-Streulänge a_{nn} charakterisiert die zwei-Neutronen-Wechselwirkung bei niedrigen Energien und ist daher eine fundamentale Größe in vielen umfassenden Forschungsfeldern, wie beispielsweise der Kernstrukturphysik. In den letzten Jahrzehnten gab es bereits zahlreiche Versuche, die Streulänge zu bestimmen, und viele Ergebnisse, einschließlich neueren, widersprechen sich. Die Messung von a_{nn} mit hoher Präzision und Genauigkeit ist auch heute noch ein herausforderndes Problem und im Gegensatz zur Proton-Proton-Streulänge ist bislang noch keine direkte Messung mittels n-n-Streuung realisierbar. In der vorliegenden Arbeit wird ein neuer Ansatz vorgestellt, der *bei hohen Energien* erzeugte relativistische radioaktive Ionenstrahlen nutzt, um damit die n-n-Streuung *bei niedrigen Energien* zu untersuchen.

Das Experiment wird an der „Radioactive Ion Beam Factory“ des Forschungsinstitutes RIKEN in Japan mit dem Ziel durchgeführt, das freie zwei-Neutronen-System unter Nutzung der Knockout-Reaktionen ${}^6\mathrm{He}(p,p\alpha)2n$ und $t(p,2p)2n$ zu untersuchen. Darüber hinaus werden Ereignisse einzelner Neutronen aus der Reaktion $d(p,2p)n$ zu Kalibrierungs- und Validierungszwecken genutzt.

Im Fall der Reaktion ${}^6\mathrm{He}(p,p\alpha)2n$ kann die Neutron-Neutron-Streulänge durch Vergleich der experimentell ermittelten Relativenergieverteilung

mit Berechnungen der effektiven Feldtheorie für Halo-Kerne, der „Halo-EFT“, bestimmt werden. Für die Reaktion $t(p,2p)2n$ werden die entsprechenden Berechnungen stattdessen auf Basis der pionenfreien EFT durchgeführt. Zum Zweck des Experiments wird am „Institut für Kernphysik“ in Darmstadt, Deutschland, ein neuer hochauflösender Neutronendetektor entwickelt und konstruiert. Ein Prototyp dieses Detektors wurde bereits an RIKEN gebaut, der in der vorliegenden Arbeit mit Elektronik der „Gesellschaft für Schwerionenforschung“ in Darmstadt in Betrieb genommen und getestet wurde.

Alle Reaktionen werden in inverser Kinematik bei einer Strahlenergie von etwa $200\,$MeV/Nukleon stattfinden, wodurch im Laborsystem relativistische zwei-Neutronen-Systeme produziert werden. Dies gewährleistet eine nahezu konstante Effizienz im relevanten Relativenergiebereich. Die Messungen werden kinematisch vollständig durchgeführt, was eine starke Unterdrückung des Untergrundes ermöglicht. Um eine ausreichende Auflösung zu erreichen, wird das Relativenergiespektrum über die direkte Messung der invarianten Masse bestimmt, was die koinzidente Messung zweier Neutronen erfordert. Die Analysemethoden für die Rekonstruktion primärer Wechselwirkungspunkte im Neutronendetektor wurden im Rahmen dieser Arbeit entwickelt und werden auf Grundlage simulierter Daten getestet und diskutiert. Aufgrund der begrenzten Auflösung, Effizienz und Akzeptanz des experimentellen Aufbaus kann die gemessene Relativenergieverteilung nicht unmittelbar mit theoretischen Berechnungen verglichen werden. Mögliche Lösungsansätze dieses Problems werden in dieser Arbeit aufgezeigt und ebenfalls anhand simulierter Daten diskutiert.

Contents

1. Introduction

1.1. The Discovery of the Neutron

First hints on the existence of the neutron came in 1930. W. Bothe and H. Becker reported on the observation [1] of secondary radiation emitted by light nuclei like lithium, beryllium and boron, after they have been hit by α particles from a polonium source. In order to classify the secondary radiation, they measured its strength of absorption in lead and came to the conclusion that photons have been created. As possible creation mechanisms, they proposed two different explanations:

1. The α particles might scatter inelastically and lead to excitations of the target nuclei. Consequently, the photons could have been emitted during de-excitation.

2. Nuclear reactions could have taken place, during which α particles were absorbed by the target nuclei. The reaction products could be created in excited states, which again de-excite by photon emission.

From the penetration power of the radiation emitted by the beryllium target, a gamma energy was concluded that surpassed the energy of the incident alpha particles. Therefore, the second explanation was favored.

A similar measurement (see review in Ref. [2]) has been conducted by I. Curie and F. Joliot, who used an ionization chamber to detect the secondary radiation. They confirmed that photons would have a higher energy than the α particles, which supported the previous interpretation of W. Bothe and H. Becker. Besides, the setup was extended by placing various substances in front of the ionization chamber [2, 3]. It was found that the ionization current remained the same for carbon, aluminum, copper and others, but was doubled when materials containing hydrogen were used, such as paraffin. However, a different important observation was made by H. C. Webster [2], who found that the penetration strength of the secondary radiation is larger in forward direction, *i.e.*, in the direction of the α particles' motion. This finding was incompatible with the previous interpretations.

J. Chadwick further improved the setup by connecting a linear amplifier to the ionization chamber [2], so that even single strongly ionizing particles (such as α particles and protons) could be detected. With this modification, recoil ions from helium, lithium, beryllium, air and argon that resulted from the secondary radiation could be observed. Considering the high energy of these recoil particles, the theory of photons as secondary particles was rejected, as a consequence of energy and momentum conservation. By assuming the existence of an electrically neutral particle that carries a mass similar to the proton, it was possible to resolve these contradictions. The momentum transfer of the α particles to the secondary radiation also explained the increased penetration depth in forward direction as discovered by H. C. Webster. After publishing his findings in 1932 [4], Chadwick received the Nobel prize in 1935. His publication is considered as the document that attests the discovery of the neutron and changed the view on the structure of atoms and atomic nuclei (see *e.g.* Ref. [5]).

1.2. Investigation of Light Neutron Clusters

The lightest example of neutron clusters is the so-called *di-neutron*, a correlated system composed of two neutrons. In the last few decades, there have been many observations of two-neutron clusters within the binding potential of various nuclei. For instance, O. V. Bochkarev *et al.* observed in 1985 [6] the di-neutron emission from excited ^{6}He nuclei that were created in ^{7}Li(d,^{3}He)^{6}He* reactions. Another example is the publication by P. G. Hansen and B. Jonson [7] about the di-neutron as a constituent of the halo nucleus ^{11}Li. Besides, K. K. Seth and B. Parker observed di-neutrons [8] by analyzing the missing-mass spectra of the breakups of neutron-rich nuclei which were created in the reactions ^{6}Li(π^{-},π^{+})^{6}H, ^{9}Be(π^{-},p)^{8}He and ^{6}Li(π^{-},p)^{5}H. Moreover, A. Spyrou *et al.* claim to have found experimental evidence for the di-neutron decay of ^{16}Be in its ground state, although their publication [9] raised controversial discussions [10, 11].

In contrast to that, the question about the existence of a bound di-neutron outside of any nuclear binding potential is not answered conclusively yet. Although neither older [12, 13] nor newer [14] searches for such a state were successful to this day, it was not possible to explicitly disprove its existence either [14, 15]. Still, due to the negative searches even down to small binding energies such as in Ref. [14], it is assumed that two free neutrons are incapable of forming a bound state. This implicates a negative neutron-neutron scattering length with a large absolute value (see Sec. 1.4 for experimental results).

As a consequence of the observation that nuclei near the neutron drip line are stabilized by the pairing of neutrons, a cluster of three neutrons, the *tri-neutron*, is less likely to exist [16]. Still, there were searches for resonant or bound states of the tri-neutron (see *e.g.* Refs. [17–19]), but no evidence for such states has been found until now.

Starting from the early 1960's, experiments have been performed searching for the *tetra-neutron*, a resonant or bound state composed of four neutrons. However, none of them resulted in an indication for its existence. In the 1980's, the research field of experimental nuclear structure physics was widened by radioactive ion beams becoming available in the laboratory [20]. Using a radioactive ^{14}Be beam, F. M. Marqués *et al.* [21] studied its breakup reaction into ^{10}Be and four neutrons and interpreted the results as an indication for a bound tetra-neutron. Later it was shown [22] that the result could match to a resonance at an energy of $\lesssim 2\,$MeV as well. These findings are consistent with results from K. Kisamori *et al.* [23], published in 2016: from the analysis of the $4n$ missing-mass spectrum of the knockout reaction ^{8}He(^{4}He,^{8}Be)$4n$, a candidate resonance with the energy 0.83 ± 0.65(stat.) ± 1.25(syst.) MeV and an upper threshold for the width of $2.6\,$MeV were deduced.

Recently, it was reported on the observation of a resonance-like structure in the four-neutron missing-mass spectrum of the reaction ^{8}He$(p, p\alpha)4n$ in Ref. [24]. The results are consistent with a tetra-neutron resonance at an energy of 2.37 ± 0.38(stat.) ± 0.44(syst.) MeV and with a width of 1.75 ± 0.22(stat.) ± 0.30(syst.) MeV. However, the theoretical interpretation of the data [25] is still ongoing.

1.3. Applications of the Neutron-Neutron Scattering Length

The neutron-neutron scattering length is a fundamental quantity of the broad research field of nuclear physics. In this section, several of its numerous important applications are pointed out. Thereby, natural units are used, *i.e.*, $\hbar = c = 1$. Sections 1.3.1, 1.3.2 and 1.3.3 follow Ref. [26].

1.3.1. Effective Range Expansion

The Hamiltonian for non-relativistic quantum mechanical scattering of two nucleons is given by

$$H = \frac{\vec{P}_1^2}{2m_1} + \frac{\vec{P}_2^2}{2m_2} + V, \tag{1.1}$$

where m_i and P_i are the masses and momentum operators of particle $i \in \{1, 2\}$, respectively, and V is the sum of the strong nucleon-nucleon potential V_{NN} and the electromagnetic potential. Therefore, V depends on the distance of the particles, their spins, masses and charges. Usually, scattering problems with two particles are treated by introducing operators for the center-of-mass (CM) position and the relative position

$$\vec{X}_{\text{CM}} = \frac{m_1\vec{X}_1 + m_2\vec{X}_2}{m_1 + m_2} \quad \text{and} \quad \vec{X}_{\text{rel}} = \vec{X}_1 - \vec{X}_2, \tag{1.2}$$

respectively, where X_i is the position operator of particle i. Corresponding to that, the operators of the CM and relative momenta are

$$\vec{P}_{\text{CM}} = \vec{P}_1 + \vec{P}_2 \quad \text{and} \quad \vec{P}_{\text{rel}} = \frac{m_2\vec{P}_1 - m_1\vec{P}_2}{m_1 + m_2}, \tag{1.3}$$

respectively. The advantage of this definition is that the Hamiltonian in Eq. 1.1 can be rewritten as

$$H = \frac{\vec{P}_{\text{CM}}^2}{2M} + \frac{\vec{P}_{\text{rel}}^2}{2m} + V, \tag{1.4}$$

where total mass M and reduced mass m are given by

$$M = m_1 + m_2 \quad \text{and} \quad m = \frac{m_1 m_2}{M}. \tag{1.5}$$

This results in two separate Hamiltonians

$$H_{\text{CM}} = \frac{\vec{P}_{\text{CM}}^2}{2M} \quad \text{and} \quad H_{\text{rel}} = \frac{\vec{P}_{\text{rel}}^2}{2m} + V, \tag{1.6a}$$

$$\textit{i.e.}, \quad H = H_{\text{CM}} + H_{\text{rel}}, \tag{1.6b}$$

describing the CM and the relative motion, respectively. These two Hamiltonians commute, as they act on different spaces, and the corresponding time-evolution operators factorize. The operator H_{rel} has the same form as the full Hamiltonian for the scattering of a single particle off a fixed potential, which means that the two-particle problem essentially reduces to a single-particle problem, just by rewriting H.

To parameterize V_{NN}, different forms are used, but each of them must satisfy the symmetries of the nucleon-nucleon interaction, including invariance under the following transformations:

- spatial translation (implying momentum conservation),
- spatial rotation (implying angular momentum conservation),
- time translation (implying energy conservation),
- Galilean transformation[1],

---

[1] In relativistic scattering, this point changes to invariance under Lorentz transformation. In the present work however, typical kinetic energies in the CM system are in the order of $0.1\,\%$ of the neutron mass only (see Secs. 1.5 and 1.6), which means for the scattering process to be clearly non-relativistic.

- parity transformation[2] (*i.e.*, point reflection) and
- time reversal.

These symmetries allow to draw conclusions on the *scattering amplitude* $f(p,\theta)$ without knowledge on the precise form of the Hamiltonian H. The scattering amplitude is connected to the differential cross section $\mathrm{d}\sigma/\mathrm{d}\Omega$ via

$$\frac{\mathrm{d}\sigma}{\mathrm{d}\Omega} = |f(p,\theta)|^2\,, \tag{1.7}$$

where p is the absolute value of the eigenvalue of $\vec{P}_{\mathrm{rel}}$, Ω the solid angle and θ the polar scattering angle[3] in the CM frame.

Due to the rotational invariance, it is useful to expand the scattering amplitude in the quantum number l of the orbital angular momentum, leading to the *partial wave series*

$$f(p,\theta) = \sum_{l=0}^{\infty} (2l+1)\, f_l(p)\, P_l(\cos\theta), \tag{1.8}$$

where $P_l(\cos\theta)$ are the Legendre polynomials and $f_l(p)$ denotes the *partial-wave amplitude*. Making use of its unitarity, the partial-wave amplitude can be parameterized as

$$f_l(p) = \frac{\exp\left(i\delta_l\right)}{p}\sin\left(\delta_l\right) = \frac{1}{p\cot\left(\delta_l\right) - ip}. \tag{1.9}$$

For each l, also called *scattering channel* l, there is a phase shift δ_l of the outgoing wave relative to the incoming one.

---

[2] As shown experimentally by C. S. Wu *et al.* [27], the invariance under parity transformation is violated by the weak interaction. However, in two-nucleon systems, the parity-conserving components of the interaction are assumed to be dominant [28].

[3] For polarized beams, the scattering amplitude can show a dependence on the azimuthal angle φ in addition to p and θ.

In 1947, J. Schwinger has shown [29, 30] that the expression $p^{2l+1}\cot(\delta_l)$ can be written as an analytic expansion in the square of the relative momentum, named *effective range expansion* (ERE). For a partial wave carrying the angular momentum l, it is given by

$$p^{2l+1}\cot(\delta_l) = -\frac{1}{a_l} + \frac{1}{2} r_l p^2 + \mathcal{O}\left(p^4\right), \tag{1.10}$$

where a_l is the *scattering length*. The quantity r_l is called *effective range parameter*. Parameters that are much larger than the corresponding powers of the typical range R of the interaction are called *unnatural*.

From the S-wave ERE, *i.e.*, Eq. 1.10 with $l = 0$, one obtains

$$\delta_0(p) \to -pa_0 \quad \text{for small } p, \tag{1.11}$$

i.e., the slope of the phase shift δ_0 at small p is determined by a_0 alone, implying that the potential is repulsive for $a_0 < 0$ and attractive for $a_0 > 0$.

The ERE shows that at low p one only needs a few parameters to describe the interaction between two nucleons. In particular, the knowledge of the exact form of the nuclear potential is not required. However, knowing the parameters of the ERE with small uncertainties can be helpful to determine the parameters of the potential at higher precision.

1.3.2. Cross Section

The ERE has shown the significance of a_0 for the interaction at low relative energies. This can be further emphasized with the scattering cross section, which exclusively depends on a_0 and the relative momentum p in the low-energy regime.

For low relative momenta, the differential cross section can be approximated by

$$\frac{\mathrm{d}\sigma}{\mathrm{d}\Omega} \approx |f_0(p,\theta)|^2 . \tag{1.12}$$

Following Eq. 1.9, the scattering amplitude for $l = 0$ is given by

$$\begin{aligned} f_0(p,\theta) &= \frac{1}{p \cot(\delta_0) - ip} && (1.13a) \\ &\approx \frac{1}{-\frac{1}{a_0} - ip} \quad \text{for small } p. && (1.13b) \end{aligned}$$

By combining the low-energy approximations from Eqs. 1.12 and 1.13b, the integrated cross section evaluates to

$$\begin{aligned} \sigma &= \frac{4\pi}{\frac{1}{a_0^2} + p^2} && \text{with} && (1.14a) \\ \sigma &\to 4\pi a_0^2 && \text{for } |a_0| \ll p^{-1} \text{ and} && (1.14b) \\ \sigma &\to \frac{4\pi}{p^2} && \text{for the so-called } \textit{unitary limit } |a_0| \to \infty. && (1.14c) \end{aligned}$$

1.3.3. Bound States, Virtual States and Resonances

In order to determine if the two-particle system has bound states, virtual states or resonances, one has to search for poles in the energy-related momentum of the full off-shell T matrix which describes the scattering process in momentum space. In the case of elastic scattering, its matrix elements are proportional to the scattering amplitude defined in Eq. 1.8.

In the complex momentum plane, bound states and virtual states appear on the positive and the negative imaginary axis, respectively, as shown in Fig. 1.1a. Furthermore, if resonances are present, they can be found on the negative imaginary half-plane. Resonances always occur in pairs: if one of them is located at the momentum $p_{\text{res},1}$, another one can be found at the negative complex conjugate $p_{\text{res},2} = -p^*_{\text{res},1}$.

As the energy corresponding to that momentum is given by $E_p = \frac{p^2}{2m}$, both bound and virtual states are mapped onto the negative real E_p axis, which is depicted in Fig. 1.1b. In contrast to that, resonances of the width Γ are mapped to

$$E_p = E_{\text{res}} - i\frac{\Gamma}{2}, \tag{1.15}$$

which is on the positive real energy half-plane, leading to an increased scattering cross section at the resonance energy E_{res}.

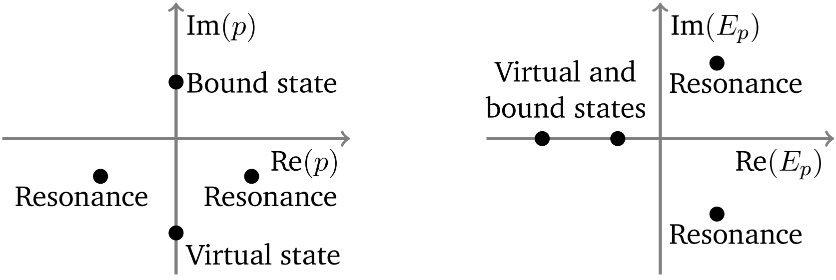

(a) Complex p plane.

(b) Complex E_p plane.

Figure 1.1.: Bound states, virtual states and resonances in the complex planes of p and $E_p = \frac{p^2}{2m}$.

If the S-wave contribution dominates and a_0 is the only unnatural parameter of the ERE, the positions of the poles can be calculated with Eq. 1.13b. Then, the T matrix has a pole at i/a_0, which implies a virtual state in the case of $a_0 < 0$ and a bound state for $a_0 > 0$. If higher orders of the ERE cannot be neglected, the two-particle system can have resonances.

In the case of neutron-neutron scattering, $a_{nn} = -18.63 \pm 0.27$ (expt.) $\pm$ 0.30 (theo.) fm [31] is the most widely used value of the scattering length (see Sec. 1.4). Its absolute value is much larger than the typical range $R \approx 1$ fm of the strong interaction. This implies that there should exist a virtual state in which the di-neutron is close to be bound. If the sign of a_{nn} was positive instead, but its absolute value still large, the di-neutron would have a weakly bound state. The existence of more strongly bound di-neutron states has been excluded experimentally (see *e.g.* Ref. [14] and references therein).

1.3.4. Charge Symmetry Breaking

In comparison to the typical energy scales of strongly interacting systems, *i.e.*, around 1 GeV, the masses[4] m_u and m_d [32, 33] of the lightest two quarks, the up- and the down-quark, are very similar:

$$m_u = \left(2.16^{+0.49}_{-0.26}\right) \text{ MeV} \quad \text{and} \quad m_d = \left(4.67^{+0.48}_{-0.17}\right) \text{ MeV}. \tag{1.16}$$

A consequence of this fact is the approximate *symmetry in isospin* [34]. Although not yet named like that, the concept of isospin has been introduced by W. Heisenberg in 1932 [5], the same year as the discovery

---

[4] Unlike other elementary particles like electrons or muons, quarks are confined inside hadrons and therefore cannot be observed as separate particles. Thus, it is not possible to measure their masses directly. Instead, the masses have to be derived using theoretical models and consequently, the dependence of the resulting quark masses on the underlying theoretical framework has to be kept in mind. The values given in Eq. 1.16 are weighted averages of different approaches as described in [32, 33] and references therein.

of the neutron. In 1936, the similarity of the interactions between two protons and two neutrons, when the Coulomb force is removed, was discussed in Ref. [35]. The similar behavior with respect to the strong interaction is called *charge symmetry* (CS), which is a special case[5] of *charge independence*, and its violation is referred to as *charge symmetry breaking* (CSB) [37]. The reasons for CSB are the electromagnetic properties of the quarks and their small, but nonzero, mass difference. One of the most important implications is the mass difference of the neutron and the proton.

Another one is the difference between the proton-proton and the neutron-neutron scattering lengths a_{pp}^{N} and a_{nn}^{N}, which provides a direct measure of the strength of CSB. The superscript N (for "nuclear part") indicates that contributions from electromagnetic interactions are not included in the respective scattering lengths. The difference $a_{nn}^{N} - a_{pp}^{N}$ is very sensitive even to small changes of the nuclear potential, due to the large absolute values of the scattering lengths in comparison to typical ranges of the strong interaction (around 1 fm). It is estimated [36] that a relative change of the nuclear potential results in a 10 to 15 times larger relative change $(a_{nn}^{N} - a_{pp}^{N})/a_{nn}^{N}$ of the scattering lengths a_{nn}^{N} and a_{pp}^{N}.

---

[5] Charge independence can be understood as an invariance under arbitrary rotations in isospin space, of which a rotation of 180° around the 2-axis is a special case. If the positive direction of the 3-axis is associated with positive charge, an invariance under such rotations corresponds to charge symmetry [36].

1.4. Former Experiments

One of the difficulties in the determination of the proton-proton and neutron-neutron scattering lengths is the correction for electromagnetic interactions[6] between the respective nucleons. In the former case, this correction is extremely large: while the bare experimental value has been determined to $a_{pp} = -7.8063(26)$ fm [38], the corrected value is $a_{pp}^N = -17.3(4)$ fm [39]. In the case of a_{nn}, an additional difficulty arises due to the lack of pure dense neutron targets. To this day, there is no direct experimental determination of a_{nn} from free neutron-neutron scattering. Instead, there have been many attempts [40] using indirect methods. A selection of them is listed in the following and their results are shown in comparison in Fig. 1.2.

The most widely used value of the neutron-neutron scattering length is $a_{nn} = -18.63 \pm 0.27\,\text{(expt.)} \pm 0.30\,\text{(theo.)}$ fm [31], as indicated by the blue band in Fig. 1.2, which results after removal of the electromagnetic effects in $a_{nn}^N = -18.9(4)$ fm [31]. This value of a_{nn} is an average calculated from data of three different experiments that are based on the pion-capture reaction $d(\pi^-,n\gamma)n$ (blue data points in Fig. 1.2). The individual final values[7] of these experiments are $-18.5(4)$ fm [42] (reanalysis of Ref. [41]), $-18.7(6)$ fm [43] and $-18.63(48)$ fm [31] (reanalysis of Ref. [44]). This reaction has the advantage that aside of the two neutrons, there exist no hadrons in the final state.

Furthermore, recent measurements of a_{nn} are based on the purely

---

[6] In the case of neutrons, corrections are necessary due to the magnetic interaction and in the case of protons mostly due to the Coulomb interaction [34].

[7] The values are quoted here exactly as given in the respective publications. As a consequence of various reanalyses of the experimental data, the corresponding values in Ref. [31], on which the final average result for a_{nn} is based, slightly differ.

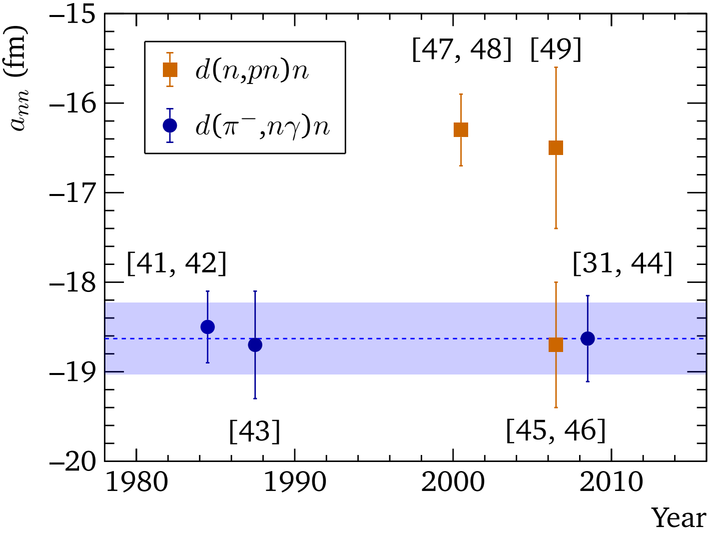

Figure 1.2.: Overview on a selection of the recent measurements of a_{nn}. The orange squares are for the purely hadronic reaction $d(n,pn)n$ and the blue circles for the pion-capture reaction $d(\pi^-,n\gamma)n$. The blue band shows the most widely used value of a_{nn} as published in Ref. [31], which is based on data from Refs. [41, 43, 44], where the free two-neutron pair was created by the $d(\pi^-,n\gamma)n$ reaction in all cases.

hadronic reaction $d(n,pn)n$ (orange data points in Fig. 1.2): a group from Bonn determined $-16.3(4)$ fm [47, 48] using an absolute cross-section measurement by coincident detection of one of the neutrons and the proton in the final state, which is in significant contradiction to the most widely used value of a_{nn}. In comparison to detecting the two neutrons, this method allowed for a larger distance between the detectors and thereby suppressed scattering of particles from one detector to the other. Besides, neutron-proton scattering was observed simultaneously, which allowed for the determination of a_{nn} using a relative cross-section measurement, resulting consistently in $-16.1(4)$ fm [47, 48].

However, using the same reaction and the same theoretical framework, a group from the “Triangle Universities National Laboratory” (TUNL) found $a_{nn} = -18.7(7)$ fm [46] (reanalysis of Ref. [45]), which is consistent with the most widely used value of a_{nn}. In this experiment, all three nucleons in the final state were measured.

Later, the group from Bonn confirmed [49] its measurement, using again the reaction $d(n,pn)n$, but this time detecting only the proton in the final state.

The values determined by the groups from Bonn and TUNL contradict each other significantly and the difference $\left|a_{nn} - a_{nn}^{N}\right|$ is smaller than the differences of the measurements of a_{nn} itself. As of today, there is no reason to mistrust any of the mentioned experiments. The contradicting results might be an indication for a systematic experimental uncertainty that is not yet understood, which motivates the experiment presented in this work.

1.5. New Experimental Approach

In 2020, a new experiment to determine the $^1S_0$ neutron-neutron scattering length has been proposed [50] and accepted at the research facility "Rikagaku Kenkyūjo" (RIKEN) in Japan. The two-neutron system will be produced using the knockout reactions ^{6}He(p,$p\alpha$)$2n$ and t(p,$2p$)$2n$ in inverse kinematics at beam energies of about $200\,\mathrm{MeV/nucleon}$. As an advantage of such high energies in the laboratory frame, the relative-energy dependent corrections for the neutron-detection efficiency are extremely small. With the two different reactions, the robustness and reliability of the experimental method and the analysis can be demonstrated. The experiment will be conducted kinematically complete, which allows for a strong suppression of background.

The neutron-neutron relative-energy spectrum will be determined experimentally in the range from 0 to roughly $1\,\mathrm{MeV}$. At these low relative energies, the final-state interaction of the two-neutron system is dominated by the neutron-neutron scattering length a_{nn}. Hence, by comparison to theoretical calculations (see Sec. 1.6), the shape of the nn relative-energy spectrum allows for a determination of the value of a_{nn}. For the spectrum resulting from the ^{6}He(p,$p\alpha$)$2n$ reaction, recent developments in the effective field theory for halo nuclei (halo EFT) [51] are available. In the case of the t(p,$2p$)$2n$ reaction, calculations will be based on the well-established pionless EFT for the triton [52]. In addition, for calibration and validation purposes of the data analysis, single-neutron events will be available from the d(p,$2p$)n reaction.

In order to reach sufficient resolution, the neutron momenta will be measured with the new neutron detector "high-resolution detector array for multi-neutron events" (HIME), which is currently under construction at "Institut für Kernphysik" (IKP) in Darmstadt, Germany. This will allow to directly determine the relative energy spectrum from an invariant-mass measurement, so that no missing-mass analysis will be required.

The high momentum transfer in the knockout process leads to a distinct separation of the two-neutron system from the charged reaction products, minimizing final state interactions between them. The kinematical completeness allows to confirm this experimentally: in the data analysis, the relative-energy spectrum can be determined after selecting different momenta of the charged reaction products. At higher momentum transfer, the shape of the spectrum should not change anymore, since the binding potential of the proton (in the case of $t(p,2p)2n$) or the ^{4}He core (in the case of ^{6}He$(p,p\alpha)2n$) suddenly vanishes in the knockout reaction without further affecting the remaining two-neutron system. For this purpose, especially the $t(p,2p)2n$ reaction is well-suited due to its large cross section (see Sec. 2.4).

1.6. Theoretical Framework

The relative-energy distribution of the two neutrons emerging from the knockout reaction ^{6}He$(p,p\alpha)2n$ is calculated [51] with the effective field theory for halo nuclei, called *halo EFT* (hEFT) [53]. The hEFT formalism includes a consistent treatment of the structure of the ^{6}He nucleus and of the final-state interaction (FSI) of the two-neutron system after the knockout reaction. As degrees of freedom, there are only the two halo neutrons and the α core, *i.e.*, the inner structure of the core is not resolved, which is useful because the first excited state of the alpha particle (20.21 MeV [54]) is very high in comparison to the two-neutron separation threshold of ^{6}He (975.46 keV [55]). As ^{5}He is unbound and there exist most likely no bound states of the free di-neutron either

[14], ^{6}He has no bound two-body subsystem. For this reason, it is called *Borromean* halo nucleus in analogy to the Borromean rings[8], as depicted in Fig. 1.3. Together, the three rings are linked, but they all become unlinked as soon as only a single one is removed.

The hEFT approach is based on a systematic expansion in the ratio of the size R_{core} of the α core and the size R_{halo} of the whole ^{6}He system, which is $R_{\mathrm{core}}/R_{\mathrm{halo}} \approx 0.2$ [50]. With each order, the precision of the result is increased and the uncertainties can be estimated systematically. The ground-state wave function of ^{6}He and the effects of the FSI of the two neutrons after the α-knockout reaction on various observables can be calculated. For verification, the calculated observables can be compared to three-body cluster calculations with the well-established code “Faddeev with core excitation” (FaCE) [56].

In Fig. 1.4, the two-neutron relative-energy spectra are shown for different values of the $^1S_0$ neutron-neutron scattering length a_{nn}, calculated in hEFT to leading order. The dependence of the spectrum on the neutron-neutron scattering length mainly enters through the two-neutron FSI. For larger $|a_{nn}|$, the peak position slightly shifts to smaller relative energy T_{rel} and the rising and falling edges of the curve become steeper. In particular, the peak height relative to the tail of the distribution is increased. These features of the calculated spectrum allow for the determination of a_{nn} via invariant-mass measurement of the two-neutron system. The calculation of the nn relative-energy spectrum will be performed to at least next-to-leading order.

In order to extract the nn scattering length from the $t(p,2p)2n$ reaction, the ground-state wave function of the triton can be calculated with pionless EFT [52], where the proton and the neutron are the only degrees

---

[8] The term “Borromean” comes from the Italian Borromeo family, whose coat of arms shows a drawing of that kind of linked rings.

of freedom at low energies. The two-neutron separation energy of 8.48 MeV [57] leads to a larger expansion parameter and thereby to a higher uncertainty in each order in comparison to hEFT with ^{6}He. However, the pionless EFT for the triton is already established up to next-to-next-to-leading order [58].

From a purely experimental point of view, the $t(p,2p)2n$ reaction is more advantageous, as its cross section is much higher in comparison to ^{6}He$(p,p\alpha)2n$ (see Sec. 2.4). However, ^{6}He has a lower $2n$-separation threshold than the triton, which improves the separation of scales and thereby simplifies the theoretical treatment in comparison to the $t(p,2p)2n$ reaction.

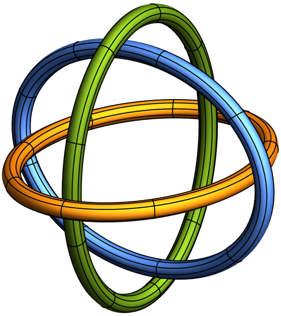

Figure 1.3.: Borromean rings.

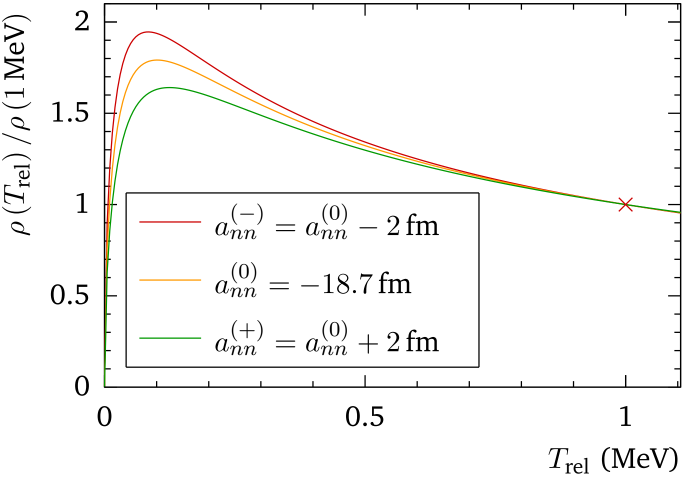

Figure 1.4.: Probability distribution ρ of the two-neutron relative-energy T_{rel} plotted for three different values of the ${}^1S_0$ neutron-neutron scattering length. Modified from Ref. [51]. The spectra are normalized to the value 1 at $T_{\text{rel}} = 1\,\mathrm{MeV}$, as indicated by the red cross.

2. Experimental Details

The beam is provided by the “Radioactive Ion Beam Factory” (RIBF) [59] at RIKEN (see Fig. 2.1). The RIBF can accelerate stable and long-lived nuclei from deuterons to ^{238}U to beam energies of a few hundred MeV [60, 61]. Using in-flight fragmentation and magnetic separation techniques, it can provide access to secondary beams of numerous different nuclides, including certain rare ones at the driplines and beyond. Thus, it allows to experimentally investigate nuclei with large isospin asymmetry and to test nuclear theories under extreme conditions.

2.1. Beam Production

2.1.1. Primary Beam Production

The electron cyclotron resonance (ECR) ion source [62] creates the primary beam of free stable ions, which are pre-accelerated in the 16 MV variable-frequency linear accelerator “RIKEN Linear Accelerator” (RILAC). For further acceleration, there are four cyclotrons available at RIBF. Which ones are operated depends on the desired energy and the kind of experiment that is to be conducted. An important property of cyclotrons is the so-called K-value, which is defined as the highest kinetic energy a proton can reach in the non-relativistic approximation inside a cyclotron, *i.e.*,

$$K = \frac{e^2}{2m_p} \left(B\rho\right)^2 , \tag{2.1}$$

where e is the elementary charge, m_p the proton mass and $B\rho$ the corresponding magnetic rigidity. The cyclotrons at RIBF and their K-values are

- RIKEN ring cyclotron (RRC), $540\,$MeV,
- fixed-frequency ring cyclotron (fRC), $570\,$MeV,
- intermediate ring cyclotron (IRC), $980\,$MeV and
- superconducting ring cyclotron (SRC), $2500\,$MeV.

For the present experiment, the fRC, the IRC and the SRC will be used to accelerate a primary ^{18}O beam to $230\,$MeV/nucleon. The SRC was the world-wide first superconducting cyclotron.

2.1.2. Secondary Beam Production

The production of the secondary beam, a radioactive ion beam (RIB), is based on in-flight[1] fragmentation and subsequent fragment separation. The primary beam impinges onto a fragmentation target, resulting in a mixture of various nuclei with high velocity in the laboratory frame,

---

[1] An alternative to the in-flight method of producing RIBs is "isotope separation on line" (ISOL). In ISOL, a light *driver beam* impinges on a target in order to induce spallation, fragmentation or fission. The reaction products are ionized and re-accelerated. Finally, the nuclei of interest are selected in a mass spectrometer.

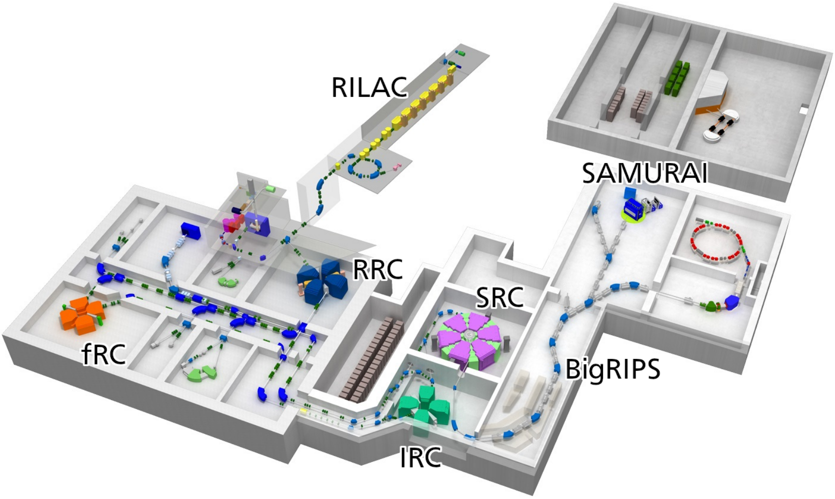

Figure 2.1.: Schematic drawing of the “Radioactive Ion Beam Factory” at RIKEN. Modified from Ref. [63].

often called *cocktail beam*. With the superconducting “RIKEN Projectile Fragment Separator” (BigRIPS) [64], the particles of the desired mass and charge numbers A and Z, respectively, can be selected. BigRIPS is an achromatic fragment separator consisting of a system of dipole magnets, degraders and collimators. Combinations of dipole magnets and collimators only let particles of a specific magnetic rigidity

$$B\rho = \frac{\gamma m v}{q} \propto \frac{A}{Z} \tag{2.2}$$

pass, so that a certain magnetic rigidity $B\rho$ is selected, which is proportional to the ratio of mass m over charge q. Consequently, for a constant beam velocity v, the ratio A/Z is fixed. The degraders serve to apply an additional constraint on the energy loss

$$\Delta E \propto Z^2, \tag{2.3}$$

which finally allows for the selection of unique Z and A. Due to the typical arrangement of magnets and degraders, this procedure is called $B\rho$-ΔE-$B\rho$ method.

The secondary beam is directed towards the experimental area “superconducting analyzer for multi particles from radioisotope beams” (SAMURAI) [65]. There, the reactions of interest take place and various detectors measure all particles that are involved in these reactions.

2.2. SAMURAI Setup

The SAMURAI experimental area (see Fig. 2.2) is a versatile setup [66] consisting of various detectors that allow for the measurement of positions, flight times and momenta of particles that are involved in the reaction. The arrangement of all detectors can be changed, which makes the investigation of a large variety of reactions possible. In the following, an overview on important components of SAMURAI is given.

The “superconducting triplet quadrupole” (STQ) 25 [68] is the last quadrupole magnet of BigRIPS that is crossed by the secondary beam before it enters the SAMURAI area. There, it traverses at first two sets of thin plastic scintillators, called “scintillators for beam time of flight” (SBT1, SBT2) [65]. To each scintillator, two photomultiplier tubes (PMTs) are connected. The detectors send a trigger signal, called *beam trigger*, if all PMTs coincidently detected scintillation light, ensuring that secondary-beam particles have reached the SAMURAI experimental area. In order to minimize straggling and the reaction probability inside the scintillation material for secondary beams of different charge numbers, there are scintillator sheets of various thicknesses available.

For the size of the coincidence window opened by the SBTs, typically about 100 ns are sufficient, as the experiment is performed in inverse kinematics. Since the maximum intensity of the secondary beam is $I = 10^6$ particles per second (pps), probability of random coincidences with cosmic or terrestrial background is very low.

Behind the SBTs, the two “beam drift chambers” (BDC1, BDC2) are located, which serve to measure the position of the beam spot as well as the spread and the profile of the beam. The reactions take place in the cryogenic liquid hydrogen target, which will probably have a thickness of about 30 mm and a diameter of 20 mm.

In experiments with radioactive ion beams, low reaction rates often constitute a strong limitation on the accuracy of experimental results. In order to reduce the statistical uncertainties, a target with larger thickness can be chosen, which will lead however to larger position uncertainties

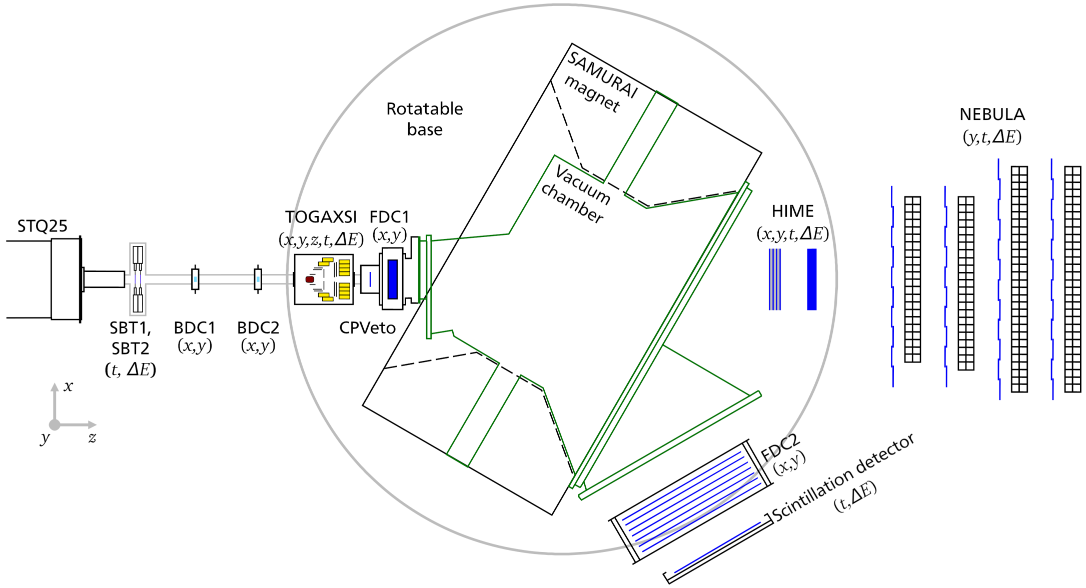

Figure 2.2.: Schematic drawing of the SAMURAI setup at RIKEN. In parenthesis, the quantities are given that are determined by measurement in the individual detectors. Measurements of ToF and energy deposition are marked with t and ΔE, respectively. Position measurements are indicated by x, y and z. The z axis follows the direction of the beam, the y axis points towards the ceiling of the SAMURAI area and the x axis forms a right-handed coordinate system with the other two axes. Modified from Refs. [65, 67].

of the reaction vertices. In the present case, the invariant-mass resolution would be affected.

This issue is addressed by the development of the device “Total energy measurement by GaGG and vertex measurement by Si strips” (TOGAXSI) [69], which is currently under construction at RIKEN. It will consist of two layers of silicon strip detectors (SSDs) that are surrounded by scintillators of gadolinium aluminum gallium garnet, chemical formula $Gd_3Al_2Ga_3O_{12}$, doped with cerium (GAGG:Ce). The design of TOGAXSI in optimized for cluster-knockout experiments in inverse kinematics. It will cover the ranges $[8°, 30°]$ and $[35°, 70°]$ [67] of the scattering angles in the laboratory frame measured relative to the beam axis. In azimuthal direction, the angular coverage will amount to about $60\,\%$. When the target is placed inside the detector, the array of SSDs will be able to measure the scattering angles of the charged reaction products, which will allow for the reconstruction of the reaction vertices. Thereby, one can take advantage of high reaction rates due to the large target thickness without having to accept a low invariant-mass resolution. The GAGG:Ce scintillators serve for energy-deposition measurements of the reaction products.

The measurement of the charged reaction products plays a crucial role in the experiment, as it allows for the selection of the reaction channel of interest. An example for a competing reaction is the single-neutron knockout ^{6}He(p,pn). It leads to the unbound ^{5}He, which instantly decays to ^{4}He and a neutron. The cross sections for that knockout process and the ^{6}He(p,$p\alpha$) reaction are of similar magnitudes [70]. The (p,pn) knockout will most likely prevent the first neutron from reaching the neutron detectors, the second neutron however is likely to be detected. Consequently, the T_{rel} spectrum would be strongly contaminated by events that are misidentified as two-neutron events in the data analysis (see Sec. 3.3). However, with the coincident detection of a proton and an

α particle with TOGAXSI, such competing reactions can be suppressed effectively. Moreover, by selection of different ranges of scattering angles in the analysis, the dependence of the invariant-mass measurement on the magnitude of momentum transfer in the knockout reactions can be investigated.

Usually, the positions of the charged particles are measured behind the target in the "forward drift chamber" 1 (FDC1) [65]. However, since the expected rate is too high and the charged particles are measured in TOGAXSI at relatively large scattering angles (see Sec. 2.3), FDC1 will not be in operation. Instead, a $3\,\mathrm{mm}$ thin plastic scintillator sheet will be installed behind the target, called "charged particle veto detector" (CPVeto). The rejection of events in which a charged particle is detected in CPVeto allows for a cleaner selection of the desired reaction channel.

The SAMURAI beam line leads to the vacuum chamber of an H-type[2] dipole magnet [71, 72], called "SAMURAI magnet". An important property of the vacuum chamber is its large acceptance due to its height of $0.8\,\mathrm{m}$ and its width of $3.24\,\mathrm{m}$ in the most narrow region. Corresponding to the maximal magnetic field strength of $3.08\,\mathrm{T}$, a bending power of up to $7.05\,\mathrm{T\,m}$ (calculated from the field integral) can be reached. In the present experiment, the field will probably be set to $2\,\mathrm{T}$ in center of the SAMURAI magnet. On its downstream side, the vacuum chamber is bounded by two windows through which the particles can leave the magnet. One of them is for neutrons and consists of stainless steel with a thickness of $3\,\mathrm{mm}$. In order to remain stable under atmospheric pressure, it is shaped like a cylinder segment that is bent towards the middle of the vacuum chamber. The window for charged particles consists of a combination of Mylar and a synthetic fiber out of poly-paraphenylene

---

[2] The letter "H" refers to the shape of the iron yoke of the magnet. Common are also O- and C-types.

terephthalamide (trademark Kevlar).

The SAMURAI magnet serves to separate particles according to their magnetic rigidities (see Eq. 2.2). This allows to identify the reaction products and the unreacted beam particles in detectors that are optimized for the particle type of interest. Using information about time-of-flight (ToF) and measured positions of charged particles, as well as the field map of the dipole magnet, the flight tracks can be reconstructed and the corresponding momenta can be determined. To reconstruct neutron momenta, the field map of the SAMURAI magnet is not required, but instead there arises the additional complication of reconstructing the primary interaction points of neutrons in the neutron detectors, which is discussed in Sec. 3.1.

In the second forward drift chamber (FDC2), the positions of the deflected particles are measured. Finally, the charged particles are detected in an array of plastic scintillators behind the magnet, which serves for the determination of ToF and energy loss. In the present case, FDC2 and the plastic-scintillator array are only used for the detection of the unreacted ^{6}He particles.

The neutrons continue their straight flight paths towards the neutron detectors “high-resolution detector array for multi-neutron events” (HIME) and “neutron detection system for breakup of unstable nuclei with large acceptance” (NEBULA) [73, 74].

At the moment, only a prototype of HIME is in operation at RIKEN, called HIME JP in the following. It consists of two separate cross-shaped arrays of plastic-scintillator bars, which will be re-assembled to a single cuboid-shaped one. The individual arrays of scintillators are called *detector walls* in the following. Another detector wall, called HIME DE, is currently under construction at IKP in Germany. All scintillator bars of HIME are made of EJ-200 [75] and to each one, two PMTs are connected. The combination of a scintillator and its two PMTs will be called *module* in the following. When a neutron enters the detector, it can scatter off a nucleus which creates light flashes as it moves through the scintillators. In order to avoid that light flashes leave the individual modules before reaching the PMTs, each one is wrapped in two layers of aluminized Mylar with a thickness of 6 µm thickness. As its name suggests, HIME is optimized in terms of resolution, which is accomplished by smaller scintillator-bar sizes to improve position resolution, and new electronics for a higher time precision. HIME is discussed in detail in Chapter 4.

Table 2.1.: Number of layers, modules per layer and veto modules per layer for all neutron-detector walls.

Detector wall	number of layers	number of modules per layer	number of veto modules
HIME JP	4	24	0
HIME DE	7	24	0
NEBULA 1	2	22	7
NEBULA 2	2	23	10
NEBULA 3	2	30	12
NEBULA 4	2	30	12

Just like HIME, NEBULA is a modular plastic-scintillator based neutron detector. NEBULA consists of vertically aligned BC-408 [76] plastic-scintillator bars that are mounted vertically in four separate detector walls. Each wall contains a layer of thin veto bars that is followed by two thicker layers serving for neutron detection. The veto scintillators are used to prevent charged particles from triggering the detection system. The dimensions of the neutron-detection and veto bars are 1800 mm (length) × $120\,\mathrm{mm}$ (width) × $120\,\mathrm{mm}$ (depth) and $1900\,\mathrm{mm}$ (length) × $320\,\mathrm{mm}$ (width) × $10\,\mathrm{mm}$ (depth), respectively. All scintillators are wrapped in two layers of $10\,\mu\mathrm{m}$ thick aluminized Mylar, covered by two layers of black tape with a thickness of $100\,\mu\mathrm{m}$ to prevent light from other sources from triggering the PMTs. Recently, NEBULA has been extended from two separate detector walls to four ones. The newer ones have less scintillator bars per layer than the older ones and are closer to the SAMURAI magnet.

For each neutron-detector wall, the number of layers, scintillator bars per layer and veto bars per layer is listed in Tab. 3.1. The number of veto bars is given as it is implemented in the simulation presented in Sec. 3.1. As the construction of HIME ongoing and the NEBULA walls 1 and 2 have been added only recently, these numbers might be different in the experiment.

2.3. Reaction Kinematics

If the momentum transfer in the reactions $^6\mathrm{He}(p,p\alpha)2n$ and $t(p,2p)2n$ is sufficiently small, FSI of the two-neutron system with the charged particles can become significant for the reaction mechanism. The momentum transfer is directly connected to the scattering angle θ_{CM} in the CM system of the two particles that are involved in the respective knockout reactions, *i.e.*, the α particle and the proton in the former case and the two protons in the latter. The angle θ_{CM} can be obtained from its Lorentz transform in the laboratory system, θ_{lab}, which can be measured with TOGAXSI. If the energy that is transferred to a nucleon or a cluster of nucleons is much larger than the separation energy in its nucleus, the reaction is called “quasi-free scattering” (QFS). Typically, QFS is reached for $\theta_{\mathrm{CM}} \gtrsim 50°$.

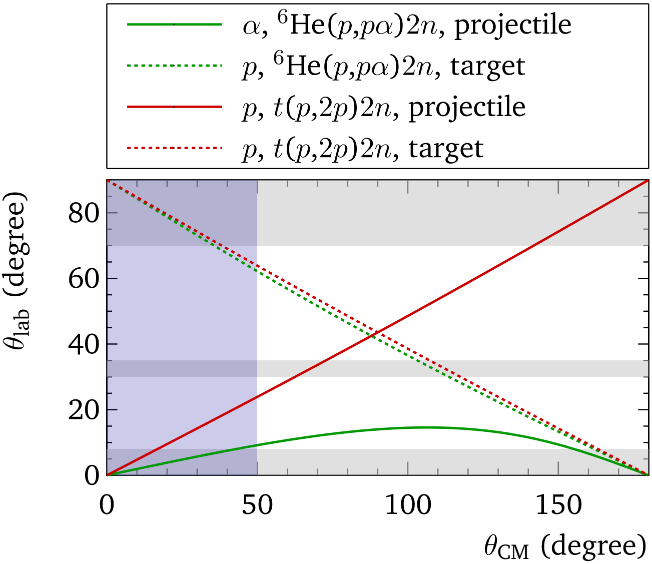

Figure 2.3.: Dependence of θ_{lab} on θ_{CM}, denoting the scattering angles relative to the beam axis measured in the laboratory system and the CM system, respectively. The function $\theta_{\mathrm{lab}}\,(\theta_{\mathrm{CM}})$ is shown for the charged products of the ^{6}He(p,$p\alpha$)$2n$ (green) and t(p,$2p$)$2n$ (red) reactions. The gray bands indicate the ranges of θ_{lab} that are not covered by TOGAXSI [69] and the blue filled area represents the θ_{CM} range where the momentum transfer is too low for QFS.

In Fig. 2.3, θ_{lab} is shown as a function of θ_{CM}. The calculations are conducted with the software package “Ligne d’Ions Super Epluchés” (LISE^{++}) [77], approximating the kinematics of the knockout reactions ^{6}He(p,$p\alpha$)$2n$ and t(p,$2p$)$2n$ with free elastic α-p and p-p scattering, respectively. The kinetic energy of the projectile is $200\,\mathrm{MeV/nucleon}$ in both cases. In the experiment, the internal motion of nucleons inside their respective binding potentials will lead to a broadening of the function $\theta_{\text{lab}}\,(\theta_{\text{CM}})$.

Figure 2.3 shows that TOGAXSI covers most of the relevant ranges of scattering angles, which is important to maximize the rate of successfully reconstructed $^6\text{He}(p,p\alpha)2n$ and $t(p,2p)2n$ events, as presented in Sec. 2.4, and to study the momentum-transfer dependence of the measurement results.

2.4. Rate Estimation

The rate estimation follows Ref. [67], where a similar setup is required. The maximum intensity of the secondary beam is expected to be $I_{\text{beam}} = 10^6$ pps, impinging onto a target of thickness $d_{\text{tgt}} = 3\,\text{cm}$ and mass density $\rho_{\text{tgt}} = 71\,\text{mg}\,\text{cm}^{-3}$.

The differential knockout cross section σ_{knockout} of the reactions $^6\text{He}(p,p\alpha)2n$ and $t(p,2p)2n$ is approximated with the corresponding cross sections of elastic scattering, $(\mathrm{d}\sigma/\mathrm{d}\Omega)^{\text{(elastic)}}_{p-\alpha}$ and $(\mathrm{d}\sigma/\mathrm{d}\Omega)^{\text{(elastic)}}_{p-p}$, where the former was previously measured in Ref. [78] and the latter, which is assumed to be isotropic [79], is taken from Ref. [80]. Since a coincident measurement of the charged reaction products is required to select the reaction channel of interest, the differential cross sections are integrated over the angles covered by TOGAXSI, which yields $\sigma^{\text{(elastic)}}_{p,\alpha} = 0.5\,\text{mb}$ and $\sigma^{\text{(elastic)}}_{p-p} = 4.3\,\text{mb}$.

Moreover, various detection efficiencies have to be taken into account. For the measurement of charged particles, $\epsilon_{\text{charged}} = 40\,\%$ [67] is estimated for both reactions, including the detection efficiency and the geometrical acceptance. The coincident measurement and successful reconstruction of two neutrons amounts to $\epsilon_{2n} = 0.32\%$ and $\epsilon_{2n} = 2.0\%$ for detection in HIME alone and combined with NEBULA, respectively, according to the simulation results discussed in Secs. 3.5.1 and 3.5.2. In order to give a conservative rate estimation, an additional efficiency $\epsilon_{\mathrm{DAQ}} = 0.5$ is assumed, accounting for limitations that are related to the data acquisition (DAQ).

Table 2.2.: Estimated rates for the reactions ^{6}He(p,$p\alpha$)$2n$ and t(p,$2p$)$2n$ for coincident two-neutron detection in HIME alone and combined with NEBULA.

Detectors	Reaction	Rate (10^3 events/day)
HIME	^{6}He(p,$p\alpha$)$2n$	0.89
	t(p,$2p$)$2n$	7.6
HIME and NEBULA	^{6}He(p,$p\alpha$)$2n$	5.5
	t(p,$2p$)$2n$	48

As shown in Fig. 1.4, the sensitivity to the neutron-neutron scattering length is mainly in the low-energy region of the T_{rel} spectrum. Furthermore, the acceptance of the setup (see Secs. 3.5.1.2 and 3.5.2) decreases at higher relative energies, so that only two-neutron events with relative energies below a certain $T_{\mathrm{rel}}^{\mathrm{max}}$ contribute significantly to the value of a_{nn}. The fraction of two-neutron events in that T_{rel} range is given by

$$f_{2n}\left(T_{\mathrm{rel}}^{\mathrm{max}}\right) = \frac{\int_0^{T_{\mathrm{rel}}^{\mathrm{max}}} \rho\left(T_{\mathrm{rel}}\right)\, \mathrm{d}T_{\mathrm{rel}}}{\int_0^{\infty} \rho\left(T_{\mathrm{rel}}\right)\, \mathrm{d}T_{\mathrm{rel}}}, \tag{2.4}$$

where $\rho\left(T_{\mathrm{rel}}\right)$ denotes the relative-energy probability distribution. For

$T_{\text{rel}}^{\text{max}} = 1\,\text{MeV}$, $f_{2n}\,(1\,\text{MeV}) \approx 25\,\%$ is obtained consistently [81] from hEFT [51] and FaCE [56] calculations.

Finally, the rate is estimated with

$$\begin{aligned} \dot{N}_{\text{events}} = I_{\text{beam}} \cdot d_{\text{tgt}} \cdot \rho_{\text{tgt}} \cdot \frac{N_A}{M_H} \cdot \sigma_{\text{knockout}} \\ \cdot \epsilon_{\text{charged}} \cdot \epsilon_{2n} \cdot \epsilon_{\text{DAQ}} \cdot f_{2n}\,(1\,\text{MeV})\,, \end{aligned} \tag{2.5}$$

where N_A/M_H is the Avogadro constant divided by the molar mass of hydrogen. The results are listed in Tab. 2.2.

3. Analysis Methods

As mentioned in Sec. 1.5, the determination of the two-neutron relative-energy spectrum is accomplished by direct invariant-mass measurement. It is shown in Sec. 3.2 that the relative energy can be written as a function of only three variables, the velocities of the neutrons in the laboratory system and the opening angle enclosed between the corresponding momentum vectors. These quantities will be determined by ToF and position measurements with the neutron detector HIME. A challenging part of the analysis is the reconstruction of the primary interaction points of the neutrons with the scintillator material, which includes in particular preventing the misidentification of single-neutron events as two-neutron events. For this purpose, a reconstruction algorithm has been developed, which is presented in detail in Sec. 3.3. The performance of the neutron reconstruction with simulated data is discussed in Sec. 3.5. In order to compare the reconstructed relative-energy distributions with hEFT spectra, it is necessary to either distort the latter with the response of the experimental setup, or to try removing the effects of the setup response from the measurement. Possible realizations of these methods are described and discussed in Secs. 3.4 and 3.6, respectively.

3.1. Simulation and Analysis Frameworks

The simulation code used in this work is based on the ANAROOT software toolkit [82] for the analysis of RIBF data, which has been developed at RIKEN and uses the simulation software “Geometry and Tracking” (Geant4) [83–85]. In order to model the particle transport in the simulation, the physics list QGSP_INCLXX_XS [86], which is based on the “Intranuclear Cascade Model”, is used in most cases. Only in Sec. 3.5.3, results from QGSP_BERT_XS [87, 88], which implements the “Bertini Cascade Model”, are discussed as well. Both physics lists include the scattering of neutrons and protons at intermediate and high energies, using the “Quark-Gluon-String Model”. For the present simulations, they are extended by additional libraries for neutron scattering at energies below $20\,\mathrm{MeV/nucleon}$. The analysis of all data is conducted using the programming language C++ together with the data-analysis framework ROOT [89].

A major advantage of using the ANAROOT code in this work is that it already has been tested and validated with experimental data and that it includes the geometry of the SAMURAI area and the instruments therein, such as the SAMURAI magnet or the NEBULA neutron detector. In this work, this code has been modified and extended to include the new HIME neutron detector, which has smaller scintillator-bar dimensions than NEBULA and a higher time resolution. The coordinates of hits in the neutron detectors that result from the simulation are randomized in order to account for the limited resolution in position and time measurements.

In each event, two neutrons are generated in the region of the target cell and directed towards the SAMURAI magnet and the HIME and NEBULA neutron detectors. Although neutrons carry no electrical charge, the magnet is of high relevance due to its iron yoke which limits the acceptance. Many important properties of the experimental setup can be derived from the simulation, such as the efficiency for the reconstruction of two-neutron events or the relative-energy resolution. In addition, by simulating single neutrons, the probability for their misidentification as neutron pairs can be determined.

In the experiment, the beam spot on the target has a certain spatial extent and there exists a non-zero beam spread, *i.e.*, the momentum vectors of the incoming particles can point to different directions. It is important to reproduce these conditions in the simulation to ensure the comparability to experimental data. Besides, in the case of a perfect point-like beam spot without any divergence of the beam, artifacts might occur in the simulated data that have no physical relevance.

Therefore, the neutrons are generated in the laboratory system at random positions within the cylindrical volume of the target. In longitudinal and radial direction, the initial positions follow a uniform distribution and a Gaussian one with a standard deviation of $6.4\,\mathrm{mm}$, respectively. The beam spot has circular shape, *i.e.*, there is no dependence of the position distribution on the polar angle. In the case of two-neutron events, relative energies are added following either one of the hEFT calculations [51] or a uniform distribution in the range $[0\,\mathrm{MeV}, 1.5\,\mathrm{MeV}]$.

The resulting system is Lorentz boosted, where the kinetic energy amounts to $200\,\mathrm{MeV/nucleon}$. In order to account for the beam spread, the azimuthal angle defining the direction of the Lorentz boost follows a Gaussian distribution with a standard derivation of $7\,\mathrm{mrad}$.

In order to define the distances between all instruments in the SAMURAI area, a cartesian coordinate system is used, where the origin is located in the center of the magnet. The orientation of the coordinate axes is as shown in Fig. 2.2, *i.e.*, the z axis points in beam direction. Relative to that coordinate system, the center of the LH_2 target is at $z = -4600\,\mathrm{mm}$. Right in front of the magnet, FDC1 is located. However, as it will most likely not be used in the experiment, it is not filled with gas in the simulation.

Table 3.1.: Positions of the upstream sides of all neutron-detector walls. The position of HIME DE is closer to HIME JP in simulations where NEBULA is added to the setup.

Detector wall	Position (mm)
HIME JP	3500
HIME DE (with NEBULA)	4100
HIME DE (without NEBULA)	4700
NEBULA 1	8028.2
NEBULA 2	8878.2
NEBULA 3	9728.2
NEBULA 4	10579.4
NEBULA 1 veto	7839.2
NEBULA 2 veto	8689.2
NEBULA 3 veto	9518.9
NEBULA 4 veto	10370.1

As only neutrons are generated, the SAMURAI magnet is mainly important due to its influence on the acceptance of the setup. However, since the secondary particles can have a non-zero electrical net charge, a magnetic field is included in the simulation. The field map is taken from Refs. [71, 90]. It defines a magnetic vector field in the ranges $-6\,\mathrm{m} \leq x \leq 6\,\mathrm{m}$, $-0.4\,\mathrm{m} \leq y \leq 0.4\,\mathrm{m}$ and $-6\,\mathrm{m} \leq z \leq 6\,\mathrm{m}$ with a maximum field strength of about $2\,\mathrm{T}$.

While in Sec. 3.5.1 both neutrons are detected in HIME only, the combination of HIME and NEBULA is studied in Sec. 3.5.2. The distance between the downstream side of HIME JP and HIME DE is $1000\,\text{mm}$ in the former case and $400\,\text{mm}$ in the latter. The z coordinates of the downstream sides of all neutron-detector walls are listed in Tab. 3.1. For the individual HIME modules, the time resolution is set to $100\,\text{ps}$ in the simulation, which is a rather conservative estimation. For the NEBULA modules, it is set to $178\,\text{ps}$. Besides the modules for neutron detection, each NEBULA wall includes two layers of veto modules (see Fig. 2.2), which partially overlap each other to avoid gaps between the individual scintillators. In Tab. 3.1, only the position of the first layer of each veto-module array is given. The position of the second one is larger by $20\,\text{mm}$ in all cases.

3.2. Invariant-Mass Spectroscopy

In the experimental method presented in this work, the relative kinetic energy T_{rel} of the two-neutron system is determined via measurement of the neutron velocities β_{n_1} and β_{n_2} in the laboratory system as well as the angle $\vartheta_{n_1 n_2}$ that is enclosed between the corresponding momentum vectors. In the following, an expression for T_{rel} that exclusively depends on these three quantities is derived (from Ref. [91]).

The invariant mass M_{inv} of a system of particles is proportional to the CM energy E_{CM}. For N massive particles, it is defined as

$$M_{\text{inv}} = \frac{E_{\text{CM}}}{c^2} = \frac{1}{c^2}\sqrt{\left(\sum_{i=1}^{N} cP_i\right)^{\mu}\left(\sum_{i=1}^{N} cP_i\right)_{\mu}} \tag{3.1a}$$

$$= \frac{1}{c^2}\sqrt{\left(\sum_{i=1}^{N} E_i\right)^2 - \left(\sum_{i=1}^{N} c\vec{p}_i\right)^2}\,, \tag{3.1b}$$

where P_i denotes the four-momentum of particle i, *i.e.*,

$$P_i = \begin{pmatrix} \frac{E_i}{c} \\ \vec{p}_i \end{pmatrix}. \tag{3.2}$$

Total energy and three-momentum of particle i with mass m_i are given by

$$E_i = \gamma_i m_i c^2 \quad \text{and} \quad \vec{p}_i = \gamma_i m_i \vec{v}_i, \tag{3.3}$$

respectively, where $\gamma_i = \left(1 - \beta_i^2\right)^{-1/2}$ is the Lorentz factor of particle i moving with the velocity $\beta_i = |\vec{v}_i|/c$. Using the identity

$$\vec{v}_i \cdot \vec{v}_j = |\vec{v}_i|\,|\vec{v}_j| \cos\vartheta_{ij} = c^2\beta_i\beta_j \cos\vartheta_{ij}, \tag{3.4}$$

where ϑ_{ij} denotes the angle enclosed between the velocity vectors $\vec{v}_i$ and $\vec{v}_j$, one obtains[1]

$$\left(\sum_{i=1}^{N} E_i\right)^2 = \sum_{i=1}^{N} \gamma_i^2 m_i^2 c^4 + \sum_{\substack{i,j \\ i\neq j}} \gamma_i\gamma_j m_i m_j c^4 \quad \text{and} \tag{3.5a}$$

$$\left(\sum_{i=1}^{N} c\vec{p}_i\right)^2 = \sum_{i=1}^{N} \gamma_i^2 m_i^2 \vec{v}_i^2 c^2 + \sum_{\substack{i,j \\ i\neq j}} \gamma_i\gamma_j m_i m_j c^2 \vec{v}_i \cdot \vec{v}_j \tag{3.5b}$$

---

[1] The expression $\sum\limits_{\substack{i,j \\ i\neq j}}$ is a short notation for $\sum\limits_{i=1}^{N}\sum\limits_{j=1}^{N}(1-\delta_{ij})$.

$$\overset{\text{Eq. 3.4}}{=} \sum_{i=1}^{N} \gamma_i^2 m_i^2 \beta_i^2 c^4 + \sum_{\substack{i,j \\ i \neq j}} \gamma_i \gamma_j m_i m_j \beta_i \beta_j c^4 \cos\vartheta_{ij}. \tag{3.5c}$$

Inserting Eqs. 3.5a and 3.5c in Eq. 3.1b yields

$$M_{\text{inv}} = \sqrt{\sum_{i=1}^{N} \gamma_i^2 m_i^2 \left(1 - \beta_i^2\right) + \sum_{\substack{i,j \\ i \neq j}} \gamma_i \gamma_j m_i m_j \left(1 - \beta_i \beta_j \cos\vartheta_{ij}\right)} \tag{3.6a}$$

$$\overset{\gamma^2(1-\beta^2)=1}{=} \sqrt{\sum_{i=1}^{N} m_i^2 + \sum_{\substack{i,j \\ i \neq j}} m_i m_j \gamma_i \gamma_j \left(1 - \beta_i \beta_j \cos\vartheta_{ij}\right)}. \tag{3.6b}$$

This expression for the invariant mass M_{inv} holds for an arbitrary set of massive particles. Note that the production of photons has not been considered in this derivation.

In the special case of a two-neutron system, i and j will only run over the neutrons n_1 and n_2, so that from Eq. 3.6b follows

$$M_{\text{inv}} = \sqrt{2m_n^2 + 2m_n^2 \gamma_{n_1} \gamma_{n_2} \left(1 - \beta_{n_1} \beta_{n_2} \cos\vartheta_{n_1 n_2}\right)} \tag{3.7a}$$

$$= m_n \sqrt{2\left(1 + \gamma_{n_1} \gamma_{n_2} \left(1 - \beta_{n_1} \beta_{n_2} \cos\vartheta_{n_1 n_2}\right)\right)} \tag{3.7b}$$

with neutron mass m_n. Using

$$M_{\text{inv}} c^2 = E_{\text{CM}} = 2m_n c^2 + T_{\text{rel}}, \tag{3.8}$$

the relative energy of the two-neutron system finally evaluates to

$$\frac{T_{\text{rel}}}{m_n c^2} = \sqrt{2\left(1 + \gamma_{n_1} \gamma_{n_2} \left(1 - \beta_{n_1} \beta_{n_2} \cos\vartheta_{n_1 n_2}\right)\right)} - 2. \tag{3.9}$$

The determination of unique T_{rel} values with Eq. 3.9 requires the knowledge of the first interaction points of the neutrons with the scintillation material. An approach to event-wise reconstruct them from the distributions of hits in the neutron detectors HIME and NEBULA is presented in Sec. 3.3.

3.3. Neutron-Reconstruction Algorithm

The different reactions that primary neutrons undergo can lead to different secondary particles, possibly causing avalanches of hits in the detector walls. The information available about each hit is position, ToF, energy deposition and the identification number of the scintillator module that has registered a particle (see Sec. 4.1). For an event-wise reconstruction of the primary interaction points of the neutrons with the detector material from this information, an algorithm has been developed in Ref. [91] and improved in this work. From the time and position coordinates of the reconstructed points, the momentum vectors of the neutrons can be calculated, which finally allows for the determination of relative energies with Eq. 3.9. In this section, the working principle of the neutron-reconstruction algorithm is presented and in Sec. 3.4, a simple approach of comparing theoretical calculations to the resulting relative-energy spectrum is described. The performance of the neutron reconstruction is discussed in Sec. 3.5.

3.3.1. Forming Groups of Hits

When a neutron passes through the scintillation material of HIME, it can undergo a variety of reactions and thereby create many different secondary particles. For instance, quasi-free scattering off one of the nucleons of a ^{12}C atom, or scattering off the whole nucleus itself are possible. In the ideal case however, the incoming neutron scatters off a proton that belongs to a hydrogen atom with a large scattering angle in the CM frame, transferring a large fraction of its kinetic energy. Compared to heavier nuclei, protons have the largest range in the scintillation material and create the strongest light output. Depending on the direction of movement and the kinetic energy, the proton can pass through multiple layers of the detector, creating hits in different scintillator bars. Besides, from the interaction of moving charged particles with the scintillation material, photons are created which can cross multiple modules as well.

As a first step, all hits with an energy deposition below 2 MeV are removed from the data, as a poor resolution is expected at such low energies. Besides, the systematic uncertainties that arise from the differences of the physics lists QGSP_INCLXX_XS and QGSP_BERT_XS (see Sec. 3.5.3) are largest in the low-energy region. Next, the neutron-reconstruction algorithm groups all hits in the same detector wall which are close to each other with respect to spatial distance and time difference. This process is called *clustering* and the resulting groups of hits are referred to as *clusters* in the following.

The first hit of a cluster always is the most important one, because it gives the first known interaction point of a neutron with the scintillation material. Building clusters is helpful to distinguish background from neutron hits, but for the calculation of relative energies, only the knowledge of the first interaction points is required. Therefore, when the terms “ToF”, “velocity” or “position of a cluster” are used, they refer to the respective properties of the first hit of this cluster.

In Fig. 3.1, correlations of time differences and spatial distances are shown for all pairs of hits in HIME DE that are found in the same event. To decide which pairs of hits are to be added to the same cluster, the condition

$$\sqrt{\left(\frac{\Delta r}{r_0}\right)^2 + \left(\frac{\Delta t}{t_0}\right)^2} < 1 \tag{3.10}$$

is checked (similar to Ref. [92]). This inequality defines the region enclosed by an ellipse with the semi axes r_0 and t_0. A segment of this ellipse is drawn as a solid line in Fig. 3.1. As mentioned above, scattered protons are most desirable for the identification of primary neutron hits. Therefore, it is useful to choose the conditions for hits to be part of the same cluster in accordance to typical proton energies. Besides, the geometry of the detector and its resolution should be taken into account. The choices of r_0 and t_0 for the individual detector walls are listed in Tab. 3.2. For HIME JP, there occur multiple local maxima at multiple different positions as a result of the gaps between the individual layers.

Table 3.2.: Parameters r_0 and t_0 of Eq. 3.10 for HIME JP, HIME DE and NEBULA.

Detector wall	r_0 (mm)	t_0 (ns)
HIME JP	280	3
HIME DE	150	2.5
NEBULA	280	2

The dashed lines in Figs. 3.1a and 3.1b represent a linear function that is fit to the maxima of all projections of constant Δr in the interval $[250\,\mathrm{mm}, 350\,\mathrm{mm}]$ onto the Δt axis. As a result of the fit procedure, the inverse slope of the line is determined to $300.2(20)\,\mathrm{mm\,ns^{-1}}$, which corresponds to the speed of light. This indicates that the correlation of Δt and Δr is caused by photons that are scattered inside of HIME DE and interact multiple times with the scintillation material.

3.3.2. Cross-Talk Suppression

The result of the first step of neutron reconstruction is a set of clusters, distributed over the two detector walls of HIME. Since all hits that are close to each other in space and time are added to the same cluster, small relative energies would be suppressed preferentially, if both neutrons interacted in the same HIME wall. Therefore, the reconstruction algorithm exclusively aims at the detection of neutrons in different walls. Consequently, the choice of the gate in the space of Δr and Δt, as shown in Fig. 3.1, does not change the sensitivity for relative energies in a certain range, which guarantees a certain freedom in choosing the values r_0 and t_0 of Eq. 3.10. Still, if the conditions are too strict, there is nearly no difference to an analysis without clustering so that the resolution will decrease. On the other hand, if they are too relaxed, more noise will occur in the relative energy spectrum.

If less than two clusters are found, there is no other possibility than to skip the event, since there is not enough information left to calculate a relative energy. In the case of more than one cluster in each wall of HIME, only the cluster with the smallest ToF in each wall will be kept for the further analysis.

Unfortunately, the presence of a cluster in each detector wall does not guarantee that two different neutrons interacted with the scintillator material in HIME, since a single primary neutron or any of its secondary particles can deposit energy in the wall closer to the target and interact a second time in the other one, which is called *cross talk* in the following. To exclude such events from the analysis, the velocities β_1 and β_2 of

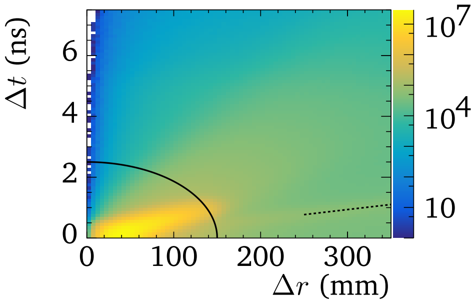

(a) The solid line represents the gate that is applied to the simulated data: each pair of hits leading to an event inside of the enclosed area is assigned to the same cluster.

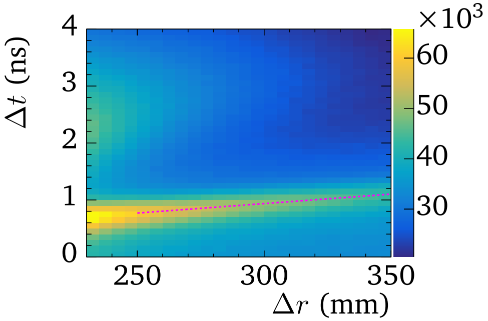

(b) In smaller ranges of Δr and Δt, the photon line is visible more clearly.

Figure 3.1.: Time difference vs. spatial distance for all pairs of hits in HIME DE. The dashed lines represent a linear fit through the maxima of all projections of constant Δr in the interval $[250\,\mathrm{mm}, 350\,\mathrm{mm}]$ onto the Δt axis. Counts around this line result from photons that are scattered multiple times in the detector. Figures (a) and (b) are based on the same data set, but show different ranges of Δr and Δt.

the clusters in HIME JP and HIME DE, respectively, are calculated using their ToF and the distance from the target to their position of detection. Only events with $\beta_1 < \beta_2$ will be kept, because this inequality will not hold for particles that deposit energy in the first detector wall and get measured a second time.

Yet, a different problem arises when the energy deposition in the first wall is very small: in this case, the scattering angle is small as well and the velocities β_1 and β_2 are nearly identical. Therefore, as a consequence of the finite time and position resolution, the condition $\beta_1 < \beta_2$ could be fulfilled, although both clusters result from the same particle. To avoid this, an energy threshold of $14\,\mathrm{MeV}$ is applied to the maximal energy deposition of all hits of the cluster in the first detector wall. It is important to note that a velocity condition of that kind does not introduce a bias on relative energies, *i.e.*, no systematic suppression of certain relative-energy values is caused. In principle, it is possible as well that a particle is scattered off the second wall and only afterwards gets detected in the first one, but those events lead to very large relative energies outside the range of interest because of the large energy loss during scattering in backwards direction.

Besides the photon hits that are counted as secondary particles of primary neutrons, there exists photon background in the experimental area that has no correlation at all with the first interaction points of the neutrons. In order to exclude such hits from the data, one makes use of the fact that charged particles deposit on average more energy in a wall of HIME than photons do, by applying an additional threshold of $10\,\mathrm{MeV}$ on the hit with the largest energy deposition in the cluster in the second detector wall.

As an advantage of applying the energy thresholds on the hit with the largest energy deposition in each cluster only instead of all hits, it is less likely to remove the first interaction point of a neutron with the scintillation material from the data: directly after the scattering of a neutron off a proton, the proton's energy is largest, therefore the energy deposition is small. The largest energy deposition per path length is reached right before the thermalization of the particle, which is why a possible hit in a second scintillator bar might have a larger light output in comparison to the first one. Thus, it is advantageous to apply an energy threshold on the hit with the largest energy deposition only and to keep all hits of the corresponding cluster, if the threshold is reached. This way, one avoids losing the information about the first interaction point of the neutron with the scintillator material, which would otherwise significantly reduce time and position resolution.

If any of the two energy restrictions for clusters or the velocity condition $\beta_1 < \beta_2$ is violated, the current event is skipped. Otherwise, the relative energy is calculated with Eq. 3.9. In summary, the neutron reconstruction works as follows:

1. Remove all hits with an energy deposition below $2\,\mathrm{MeV}$.
2. Group all hits of the same detector wall in so-called clusters, which are close to each other in spatial distance and time difference, *i.e.*, check Eq. 3.10 for all pairs of hits.
3. Check if there is at least one cluster in each detector wall. If there are more clusters than just one, only keep the one with the smallest ToF.
4. Check if $\beta_1 < \beta_2$ is fulfilled for the two remaining clusters.
5. For the clusters in the first and second detector, check if there is at least one hit with an energy deposition of $14\,\mathrm{MeV}$ and $10\,\mathrm{MeV}$, respectively.

6. Calculate T_{rel} with Eq. 3.9.

This procedure is applied to each event separately. If any of the conditions in the steps 3, 4 and 5 is violated, the reconstruction algorithm will not calculate T_{rel} for the current event, but simply proceed with the next one, starting again with step 1. The results of the neutron reconstruction are shown and discussed in Sec. 3.5.

Still, even after this procedure there remain events that are mistakenly identified as two-neutron events. For instance, this can have the following reasons:

- Despite the requested high energy deposition in the first wall, the uncertainties in the time measurements can cause the measured succession of hits to differ from the real one, so that a single neutron could be misidentified as two different ones.

- In the neutron detector, reactions of the kind $(n,2n)$ can happen, resulting in two neutrons that did not emerge from the reaction of interest. An ideal neutron detector would consist of pure liquid hydrogen, where $(n,2n)$ reactions are not possible. Unfortunately, to this day, no such active detection system exists.

Consequently, some of the experimentally determined relative-energy values will be based on the analysis of unreal two-neutron events, which limits the accuracy of the resulting spectrum.

3.4. Comparison to Theoretical Calculations

Unfortunately, it is not possible to compare the experimentally determined relative-energy distribution with the hEFT spectra directly due to experimental limitations which systematically suppress certain relative-energy ranges, such as the detector resolution and the solid angle that the detector walls cover. In order to reach comparability, one can use one of the hEFT spectra $\rho_{a_{nn}^{(1)}}(T_{\text{rel}})$ for a certain scattering length $a_{nn}^{(1)}$ (see Fig. 1.4) to generate two-neutron events for the simulation. Then, after analyzing the simulation results, the agreement of the reconstructed spectrum $\tilde{\rho}_{a_{nn}^{(1)}}$ with the experimentally determined distribution can be checked, using for instance a χ^2 test.

If it is desired to extract continuous values of a_{nn}, at least one more calculated spectrum $\rho_{a_{nn}^{(2)}}(T_{\text{rel}})$ for a different value $a_{nn}^{(2)}$ of the scattering length is required. Then, the linear combination

$$\tilde{\rho}_{\text{fit}}(T_{\text{rel}}) = p_s \cdot \left(\tilde{\rho}_{a_{nn}^{(1)}}(T_{\text{rel}}) + p_m \cdot \left(\tilde{\rho}_{a_{nn}^{(2)}}(T_{\text{rel}}) - \tilde{\rho}_{a_{nn}^{(1)}}(T_{\text{rel}})\right)\right) \quad (3.11)$$

of the distorted spectra $\tilde{\rho}_{a_{nn}^{(1)}}(T_{\text{rel}})$ and $\tilde{\rho}_{a_{nn}^{(2)}}(T_{\text{rel}})$ can be fit to the experimentally determined distribution. While the *scaling parameter* p_s only accounts for the amount of statistics of the measurement and therefore has no further interesting physical meaning, the *mixing parameter* p_m is connected to the neutron-neutron scattering length via

$$a_{nn} = a_{nn}^{(1)} + p_m \cdot \left(a_{nn}^{(2)} - a_{nn}^{(1)}\right). \quad (3.12)$$

If there are multiple theoretical predictions to be compared with the measurement, it is useful to determine the *response matrix* from the simulated data, which correlates the reconstructed relative energies $T_{\text{rel}}^{\text{rec}}$

with the generated $T_{\text{rel}}^{\text{gen}}$. Then, the distorted spectrum is obtained with the matrix multiplication

$$\tilde{\rho}_j = \sum_{i=1}^{d_{\text{gen}}} \frac{R_{ij}}{N_i^{\text{gen}}} \rho_i, \quad j \in \{1, 2, \dots, d_{\text{rec}}\}, \tag{3.13}$$

where d_{gen} and d_{rec} are the dimensions of the generated and reconstructed spectrum, respectively. The response matrix is normalized with the number N_i^{gen} of generated events in $T_{\text{rel}}^{\text{gen}}$ bin i. Using Eq. 3.13, only a single simulation is required to obtain $\tilde{\rho}$ for multiple values of a_{nn}.

As an alternative to distorting the theoretical calculation, one can try to remove the effects caused by the setup response from the measured spectrum. A possible approach for that is given in Sec. 3.6.

3.5. Results and Discussion

In the following, the results of the neutron-reconstruction algorithm are presented and discussed. In Sec. 3.5.1, only the two detector walls of HIME are used for the analysis.

As NEBULA has a considerably higher efficiency due to its larger depth, but lower time and position resolution than HIME, as presented in Sec. 3.5.2, it is interesting to investigate the effect of the choice of neutron detectors on the expected statistical uncertainties of a_{nn}. Furthermore, the physics lists, which are responsible for the particle transport in the simulation, introduce systematical uncertainties. Both issues are discussed in Sec. 3.5.3.

3.5.1. HIME

Using a uniform distribution of $T_{\text{rel}}^{\text{gen}} \in [0\,\text{MeV}, 1.5\,\text{MeV}]$, a simulation with 1.2×10^9 two-neutron events was performed, leading to the response matrices shown in Fig. 3.2. Due to noise and the limited resolution, the reconstructed relative-energy values $T_{\text{rel}}^{\text{rec}}$ can be outside of the range of the generated $T_{\text{rel}}^{\text{gen}}$ spectrum. Therefore, the $T_{\text{rel}}^{\text{gen}}$ and $T_{\text{rel}}^{\text{rec}}$ axes have different ranges in Fig. 3.2.

Following the procedure presented in Sec. 3.3, all hits with an energy deposition below $2\,\text{MeV}$ are excluded from the analysis. In addition to that, energy thresholds of $14\,\text{MeV}$ and $10\,\text{MeV}$ are applied to the hit with the largest energy deposition in clusters of HIME JP and HIME DE, respectively. As expected, in the resulting response matrix shown in Fig. 3.2a, a strong correlation between the generated values $T_{\text{rel}}^{\text{gen}}$ and the reconstructed values $T_{\text{rel}}^{\text{rec}}$ is observable, which is the basis for the sensitivity of the measurement to the quantity of interest.

For comparison, another response matrix is shown in Fig. 3.2b, where no restriction on the energy deposition of clusters is applied. Consequently, there occurs a large number of two-neutron events resulting from cross talk at low reconstructed relative energies $T_{\text{rel}}^{\text{rec}} \lesssim 0.1\,\text{MeV}$. As these counts result from a single neutron being detected twice, the $T_{\text{rel}}^{\text{rec}}$ values show no correlation to the generated $T_{\text{rel}}^{\text{gen}}$, limiting the sensitivity of the reconstructed spectrum to the neutron-neutron scattering length.

By projecting the response matrix onto the $T_{\text{rel}}^{\text{rec}}$ axis, the reconstructed spectrum can be investigated (see Sec. 3.5.1.1) and the resolution can be determined (see Sec. 3.5.1.3). Furthermore, one can gain information about the acceptance and the efficiency of the experimental setup in combination with the neutron-reconstruction algorithm (see Sec. 3.5.1.2), by projecting the data onto the $T_{\text{rel}}^{\text{gen}}$ axis. Thus, the response matrix pro-

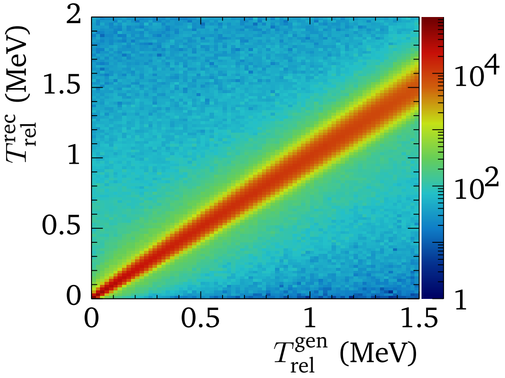

(a) Energy thresholds of $14\,\mathrm{MeV}$ and $10\,\mathrm{MeV}$ for clusters in HIME JP and HIME DE, respectively.

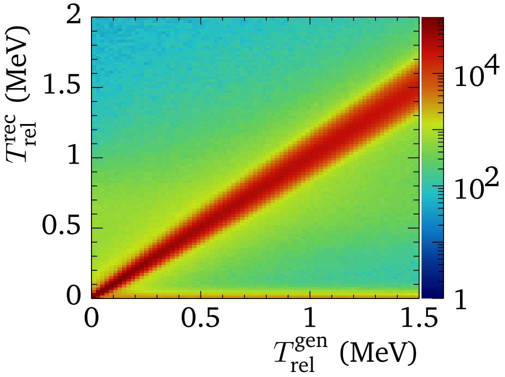

(b) No energy thresholds for clusters. At low $T_{\mathrm{rel}}^{\mathrm{rec}}$, there occurs a large amount of counts that show no correlation to $T_{\mathrm{rel}}^{\mathrm{gen}}$, resulting from cross talk.

Figure 3.2.: Response matrices obtained from HIME simulations.

vides an important benchmark for the coincident two-neutron detection.

3.5.1.1. Reconstructed Spectrum

The reconstructed spectrum is the projection of the complete response matrix onto the $T_{\mathrm{rel}}^{\mathrm{rec}}$ axis. In Fig. 3.3, several spectra are shown for different energy thresholds in the two detector walls. As mentioned in Sec. 3.3, there exists the problem of cross talk between the two HIME walls for low energy thresholds: particles are scattered off the first detector wall at small angles and are measured again in the second wall. Events of this type usually lead to small values of the reconstructed $T_{\mathrm{rel}}^{\mathrm{rec}}$. They show no correlation to the generated values $T_{\mathrm{rel}}^{\mathrm{gen}}$, which means it is impossible to draw conclusions about the true relative-energy distribution using information from these events. As the energy threshold in the first wall is increased, the spectrum becomes cleaner. At a certain point, in this case around a threshold of about $14\,\mathrm{MeV}$ or higher, the shape of the spectrum does not change anymore, but only the total amount of counts is reduced. Although a uniform $T_{\mathrm{rel}}^{\mathrm{gen}}$ distribution has been simulated, there are less counts in the first bin of the $T_{\mathrm{rel}}^{\mathrm{rec}}$ spectrum due to the limited resolution and at large $T_{\mathrm{rel}}^{\mathrm{rec}}$ as a result of the limited acceptance.

In the simulation, it is possible to check if cross talk appeared in an event: the two initially generated neutrons carry different identification numbers, which can be passed to all secondary particles that are created by them. If the reconstruction algorithm finds two clusters and their first hits carry the identification number of the same primary particle, the corresponding relative-energy value is calculated from hits that result from the same neutron. In Fig. 3.4, the probabilities for such a scenario are given for the two cases where only one or both neutrons have caused at least one hit in HIME. It should be noted however that the number of neutrons that interact with the scintillation material depends on the relative-energy distribution of the two-neutron system, which is why no probabilities are given for the first two branches “$1n$” and “$2n$” in Fig. 3.4. With a simulation based on the hEFT curve for $a_{nn} = -18.7\,\mathrm{fm}$, one finds a contribution of $0.51\,\%$ of unreal two-neutron events to the reconstructed spectrum in the range $[0\,\mathrm{MeV}, 1\,\mathrm{MeV}]$, when the energy threshold for clusters is set to $14\,\mathrm{MeV}$ and $10\,\mathrm{MeV}$ in HIME JP and HIME DE, respectively.

It is important to note that many of the events that result from cross talk between the two detector walls are located close to the region where the maximum of the relative-energy distribution is expected to be (compare Figs. 1.4 and 3.3). Therefore, these events can strongly affect the sensitivity of the measurement to the neutron-neutron scattering length, if they are not handled properly in the data analysis. Most probably, one will have to increase the thresholds until no contribution from cross talk is observed anymore and then accept the reduced efficiency that is left afterwards.

Fortunately, besides the data analysis, there are also parameters in the setup of the experiment that can be optimized to reduce cross talk: for instance, the distance between the two HIME walls can be increased in order to improve the velocity resolution, although the influence on the acceptance has to be kept in mind. Additionally, the time calibration of HIME (see Chapter 4) should be done very carefully, because its time resolution plays a crucial role.

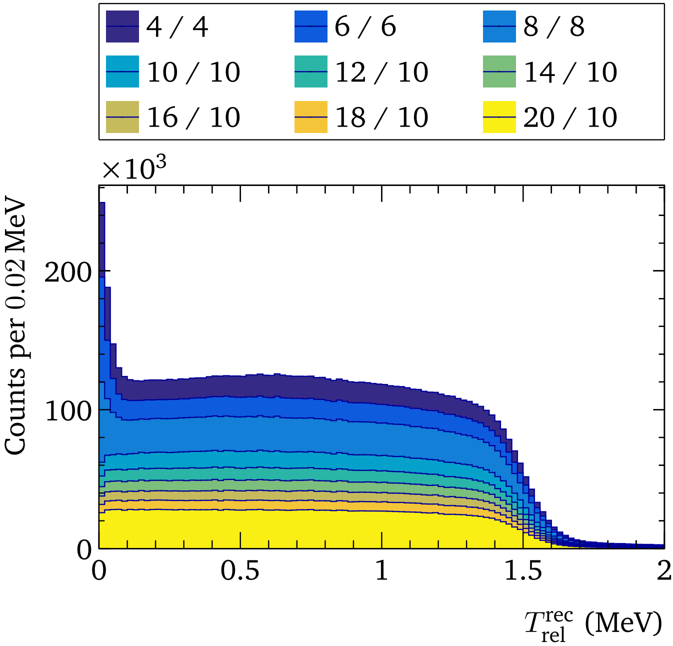

Figure 3.3.: Reconstructed relative-energy spectra from simulated data with different energy thresholds. The numbers in front of and behind the slash signs denote the energy thresholds in MeV for HIME JP and HIME DE, respectively. For thresholds in the first wall of about 14 MeV or higher, the shape of the spectra stops changing.

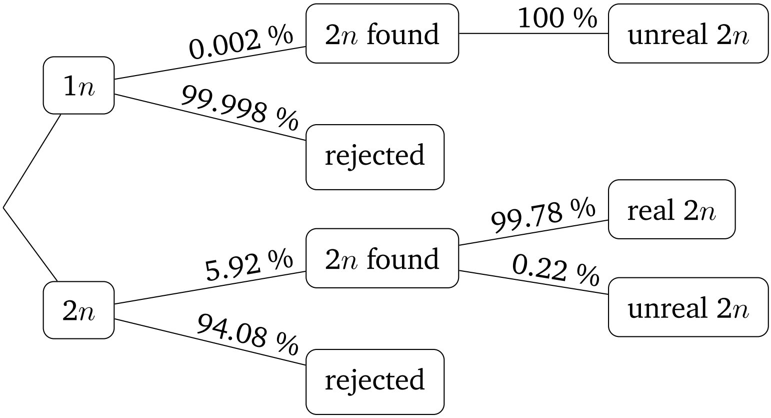

Figure 3.4.: Probabilities for the reconstruction or rejection of single-neutron and two-neutron events. The first column shows the number of neutrons that interacted with the detector in the simulation, no matter how much energy was deposited, and the second one shows if the reconstruction algorithm found two neutrons. In the last column, there is shown which percentages of reconstructed events result from cross talk. In these unreal two-neutron events, the first hits of both clusters result from the same generated primary neutron. The probabilities for the branches leading to “$1n$” and “$2n$” in the first column depend on the T_{rel} distribution, therefore no probabilities are given there.

3.5.1.2. Efficiency and Acceptance

The *two-neutron reconstruction efficiency* ϵ is defined via

$$\epsilon_i = \frac{N_i^{\text{rec}}}{N_i^{\text{gen}}} = \frac{1}{N_i^{\text{gen}}} \sum_{j=1}^{\infty} R_{ij}, \tag{3.14}$$

where R is the response matrix and N_i^{rec} denotes the number of successfully reconstructed two-neutron events, after N_i^{gen} events have been generated with $T_{\text{rel}}^{\text{gen}}$ values inside the range of the i-th bin of the relative-energy spectrum that is given to the simulation. This definition implies that ϵ includes the acceptance and the detection efficiency of the experimental setup, as well as the reconstruction efficiency of the neutron-reconstruction algorithm.

The relative-energy spectra predicted from hEFT, as depicted in Fig. 1.4, exhibit the largest sensitivity to the neutron-neutron scattering length below 1 MeV, which has been chosen as normalization point for that reason. In this $T_{\text{rel}}^{\text{gen}}$ range, ϵ is nearly constant for all energy cuts, as shown in Fig. 3.5, which is a consequence of the reactions $^6\text{He}(p,p\alpha)2n$ and $t(p,2p)2n$ being performed in inverse kinematics: since the neutrons move with beam velocity in the laboratory system, the relative energy is very small in comparison to the total kinetic energy. This is a major advantage of the experiment presented in this work, since the extremely small $T_{\text{rel}}^{\text{gen}}$-dependent efficiency corrections lead to lower systematic uncertainties of the invariant-mass measurements. Only at higher $T_{\text{rel}}^{\text{gen}}$ outside the range of interest, in this case above $T_{\text{rel}}^{\text{gen}} \approx 1$ MeV, the limited acceptance lowers ϵ considerably. Thus, in order to keep the solid angle covered by HIME sufficiently large, the detector walls should not be placed too far away from the target.

As mentioned above, there is a large contribution from unreal two-

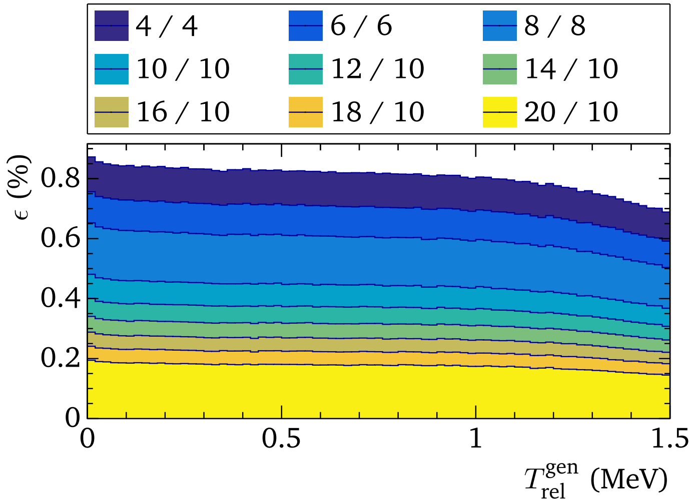

Figure 3.5.: Combined efficiency and acceptance ϵ of HIME for different energy cuts. The numbers in front of and behind the slash signs denote the energy cuts in MeV for HIME JP and HIME DE, respectively. At relative energies of about $1\,\mathrm{MeV}$ and higher, the decreasing acceptance reduces ϵ. Apart from that, the distributions are nearly uniform.

neutron events to the reconstructed spectra shown in Fig. 3.3 for low energy cuts. The shape of the spectra only stops changing for energy cuts of roughly $14\,\mathrm{MeV}$ or higher, which means for the efficiency in Fig. 3.5 to be on average $0.32\,\%$ in the range $T_{\mathrm{rel}}^{\mathrm{gen}} \in [0\,\mathrm{MeV}, 1\,\mathrm{MeV}]$ or smaller.

3.5.1.3. Resolution

The relative-energy resolution is limited by the dimensions of the scintillators as well as the intrinsic time resolution of the PMTs and the electronic readout system (see Sec. 4.1.3). Therefore, for a fixed $T_{\mathrm{rel}}^{\mathrm{gen}}$, one will obtain a distribution of $T_{\mathrm{rel}}^{\mathrm{rec}}$ values with nonzero width whose maximum is the most probable relative-energy value to be reconstructed. By projecting all vertical slices of the response matrix onto the $T_{\mathrm{rel}}^{\mathrm{rec}}$ axis, one can obtain the $T_{\mathrm{rel}}^{\mathrm{gen}}$-dependent resolution function.

The histogram in Fig. 3.6 shows the standard deviations of Gaussian curves that are fit to the individual projections. At low relative energies however, these distributions are highly asymmetric, which is why the histogram only starts at $0.1\,\mathrm{MeV}$. It is important to note that this result depends on the distance between HIME and the target.

In the experiment, the relative energy of the two-neutron system will be dominated by the transversal momentum p_t in most cases. If the difference of the longitudinal momenta of the two neutrons is zero, their transversal momenta are identical and the relative energy is simply given by

$$T_{\mathrm{rel}} = \frac{p_t^2}{m_n}, \tag{3.15}$$

where m_n is the neutron mass. The non-relativistic calculation is justified as the T_{rel} region of interest is below $1\,\mathrm{MeV}$. The neutrons move with relativistic velocity in the laboratory system, but their interaction takes place at low energies.

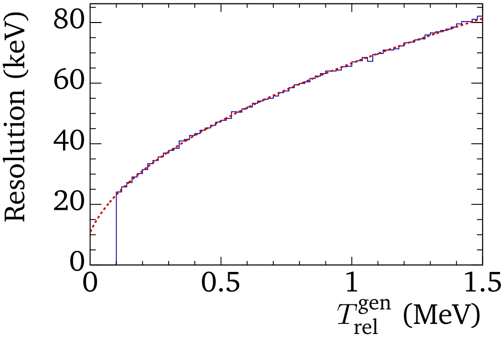

Figure 3.6.: Relative-energy resolution for two-neutron events in HIME simulations. The red curve represents the fit function defined in Eq. 3.17.

Corresponding to Eq. 3.15, the uncertainty of the T_{rel} measurement is

$$\Delta T_{\mathrm{rel}} = 2\,\Delta p_t \cdot \sqrt{\frac{T_{\mathrm{rel}}}{m_n}}. \tag{3.16}$$

The neutron momenta are determined from time and position measurements in HIME, so that the uncertainty of the transversal momentum Δp_t originates exclusively from the time resolution and the spatial extension of the plastic scintillator bars. Therefore, one can conclude from Eq. 3.16 that the shape of the resolution function $r\left(T_{\mathrm{rel}}^{\mathrm{gen}}\right)$ should correspond to a square-root curve, but should not drop to zero for $T_{\mathrm{rel}}^{\mathrm{gen}} \to 0$. For this reason, a function of the form

$$r\left(T_{\mathrm{rel}}^{\mathrm{gen}}\right) = p_0 \cdot \sqrt{T_{\mathrm{rel}}^{\mathrm{gen}} - p_1} + p_2 \tag{3.17}$$

is fit to the distribution of standard deviations, as shown in Fig. 3.6. At $0.1\,\mathrm{MeV}$, where the peak region of the T_{rel} distribution is expected to be (see Fig. 1.4), the resolution is $23.2\,\mathrm{keV}$.

3.5.2. Combination of HIME and NEBULA

An alternative to using HIME exclusively is to measure only one of the neutrons in HIME and the other one in NEBULA. With its extension to four detector walls, the total depth of the plastic-scintillation material of NEBULA amounts to $96\,\mathrm{cm}$, which is much more than a HIME wall of $12\,\mathrm{cm}$. However, both time and position resolution will be lower in NEBULA, though this problem is limited by the larger distance of NEBULA to the target: as shown in Eq. 3.9, the accuracies of velocity and angle measurements influence the $T_{\mathrm{rel}}^{\mathrm{rec}}$ distribution, which both profit from longer flight tracks of the neutrons. To decide if HIME should be used alone or in combination with NEBULA, the crucial criterion is the expected statistical uncertainty of the neutron-neutron scattering length (see Sec. 3.5.3), which depends on both the efficiency and the resolution of the setup.

These two quantities are shown in dependence of $T_{\mathrm{rel}}^{\mathrm{gen}}$ for the combination of HIME and NEBULA in Figs. 3.7 and 3.8, respectively. Analogous to Sec. 3.5.1, energy thresholds of $14\,\mathrm{MeV}$ and $10\,\mathrm{MeV}$ are applied to the hits with the highest energy deposition in clusters in HIME and NEBULA, respectively. The resulting efficiency amounts to an average of $2.0\,\%$ in the range $T_{\mathrm{rel}}^{\mathrm{gen}} \in [0\,\mathrm{MeV}, 1\,\mathrm{MeV}]$, which corresponds to an increase by a factor of 6.25 in comparison to Sec. 3.5.1.2 where HIME is used without NEBULA. Besides, the acceptance is larger than before and the contribution of unreal two-neutron events to the reconstructed spectrum is smaller: for the hEFT curve for $-18.7\,\mathrm{fm}$, it is only $0.023\,\%$

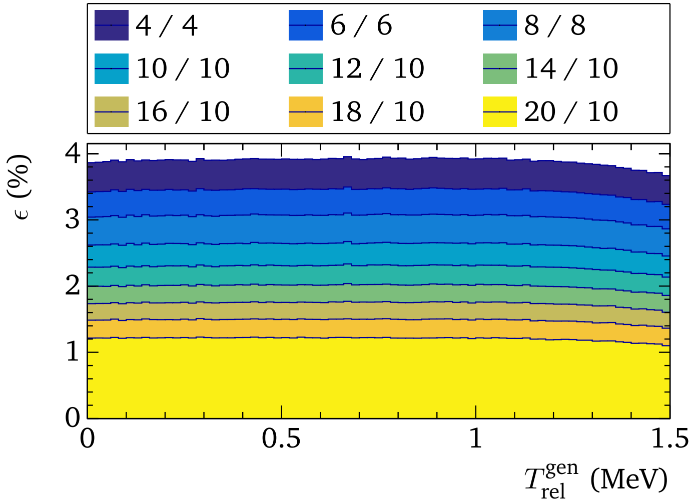

Figure 3.7.: Two-neutron reconstruction efficiency and acceptance for the combination of HIME and NEBULA for different energy cuts. The numbers in front of and behind the slash signs denote the energy thresholds in MeV for HIME and NEBULA, respectively.

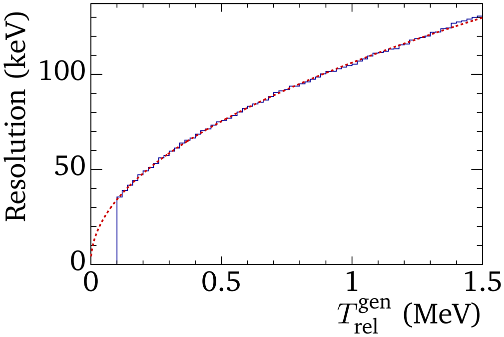

Figure 3.8.: Relative-energy resolution for two-neutron events in simulations with HIME and NEBULA. The red curve represents the fit function defined in Eq. 3.17.

in the range $[0\,\mathrm{MeV}, 1\,\mathrm{MeV}]$. However, the resolution is worse than for measurements with HIME alone (see Sec. 3.5.1.3): at $0.1\,\mathrm{MeV}$, it only reaches $34.2\,\mathrm{keV}$.

In Tab. 3.3, resolution, efficiency and the percentage of unreal $2n$ events that contribute to the reconstructed spectrum are listed for HIME alone and for the combination of the two neutron detectors.

3.5.3. Statistical and Systematical Uncertainties

In the previous Secs. 3.5.1 and 3.5.2, it has been pointed out in which way and to which extent the setup response is expected to influence the measurement results. As presented in Sec. 3.4, a possible method to account for these effects is to distort the theoretically calculated spectra and to fit a linear combination of two of them to the data using Eq.

Table 3.3.: Resolution, efficiency and percentage of unreal $2n$ events for the two-neutron reconstruction with HIME alone and in combination with NEBULA. The resolution is given at $T_{\text{rel}} = 100\,\text{keV}$, which is expected to be in the peak region of the relative-energy distribution. The efficiency and the percentage of unreal $2n$ events in the reconstruct spectrum are given as average values in the range $T_{\text{rel}}^{\text{rec}} \in [0\,\text{MeV}, 1\,\text{MeV}]$.

Detectors	Resolution (keV)	Efficiency (%)	Unreal $2n$ events (%)
HIME	23.2	0.32	0.51
HIME and NEBULA	34.2	2.0	0.023

3.11 in the range $T_{\text{rel}}^{\text{rec}} \in [0\,\text{MeV}, 1\,\text{MeV}]$. Due to Eq. 3.13, the distorted spectra $\tilde{\rho}$ will depend on the physics list that is used to determine the response matrix.

In order to study the influence of the chosen physics list on the result, a simulation with the list QGSP_BERT_XS is performed, using again HIME only without NEBULA. In the simulation, two-neutron events for $a_{nn} = -18.7\,\text{fm}$ are generated. The reconstructed spectrum, which is shown in Fig. 3.9, is filled such that there are 8×10^4 events in the range $[0\,\text{MeV}, 1\,\text{MeV}]$. To that spectrum, the function defined in Eq. 3.11 is fit with $a_{nn}^{(1)} = -18.7\,\text{fm}$ and $a_{nn}^{(2)} = -16.7\,\text{fm}$. The spectra $\tilde{\rho}_{-18.7\,\text{fm}}$ and $\tilde{\rho}_{-16.7\,\text{fm}}$ are obtained by application of the response matrix shown in Fig. 3.2a on hEFT calculations for the scattering lengths $-18.7\,\text{fm}$ and $-16.7\,\text{fm}$, respectively, using Eq. 3.13. Since the response matrix underlies statistical uncertainties, $\tilde{\rho}_{-18.7\,\text{fm}}$ and $\tilde{\rho}_{-16.7\,\text{fm}}$ do so as well. However, due to the large number of approximately 2.44×10^6 recon-

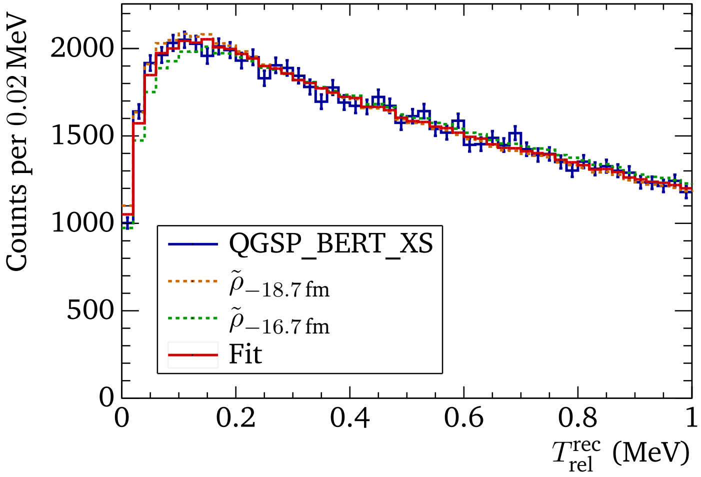

Figure 3.9.: A simulation using the physics list QGSP_BERT_XS is performed, which is based on two-neutron events following the hEFT relative-energy distribution $\rho_{-18.7\,\mathrm{fm}}$. To the reconstructed spectrum, a linear combination of the hEFT spectra $\tilde{\rho}_{-18.7\,\mathrm{fm}}$ and $\tilde{\rho}_{-16.7\,\mathrm{fm}}$ is fit (see Eq. 3.11), which result from the application of the setup-response matrix shown in Fig. 3.2a on and $\rho_{-18.7\,\mathrm{fm}}$ and $\rho_{-16.7\,\mathrm{fm}}$, respectively, using Eq. 3.13. The response simulation is performed using the physics list QGSP_INCLXX_XS, causing the reconstructed spectrum to systematically deviate from $\tilde{\rho}_{-18.7\,\mathrm{fm}}$.

structed two-neutron events with $T_{\text{rel}}^{\text{rec}} \in [0\,\text{MeV}, 1\,\text{MeV}]$ in comparison to the spectrum from the simulation with QGSP_BERT_XS, they are neglected in the fit procedure.

Inserting the fit result in Eq. 3.12 yields $a_{nn} = -17.91(19)\,\text{fm}$, which differs by $0.79(19)\,\text{fm}$ from the simulation input. Nevertheless, by eye, the blue spectrum shown in Fig. 3.9 seems to agree well with $\tilde{\rho}_{-18.7\,\text{fm}}$, which demonstrates that the experiment presented in this work aims at measuring a subtle effect.

In Ref. [93], the physics lists QGSP_INCLXX_XS and QGSP_BERT_XS are compared to experimental data with single neutrons at $110\,\text{MeV}$ and $250\,\text{MeV}$. The observed detection efficiencies often lie between the two different predictions of the physics lists, so that no conclusive statement can be given about which model to use preferentially.

As a benchmark for the precision of the physics lists reproducing the setup response, simple experimental observables of single-neutron events are most suitable, such as energy deposition per scintillator bar or per detector wall, multiplicities and efficiencies. Therefore, a high amount of statistics from the $d(p,2p)n$ reaction will allow to control systematic uncertainties, increasing the precision not only for the experiment presented in this work, but also for future experiments involving HIME.

The comparison of $\tilde{\rho}_{-18.7\,\text{fm}}$ and $\tilde{\rho}_{-16.7\,\text{fm}}$ to a simulation with QGSP_INCLXX_XS instead of QGSP_BERT_XS using Eq. 3.11 is trivial and obviously reproduces the value of $a_{nn} = -18.7\,\text{fm}$ that is inserted in the simulation within the range of the statistical uncertainty Δa_{nn}, as the setup response is obtained from the same physics list. However, Δa_{nn} itself in dependence on the number N_{rec} of reconstructed events is of high interest for the analysis. It can be obtained by applying the same fit procedure as for the QGSP_BERT_XS simulation.

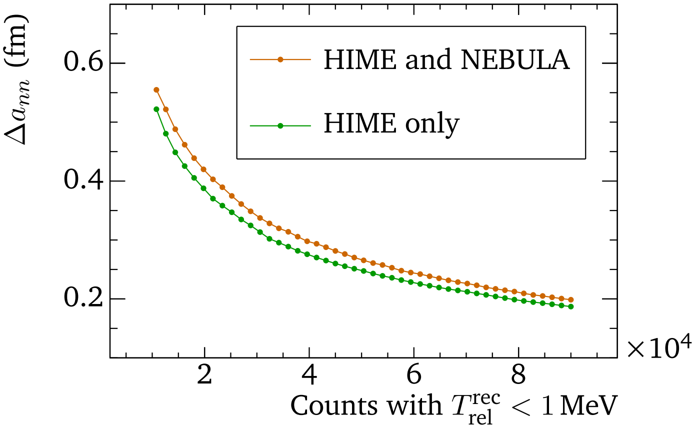

Figure 3.10.: Expected statistical uncertainties in dependence on the number of events with $T_{\mathrm{rel}} < 1\,\mathrm{MeV}$.

The results are shown in Fig. 3.10 for coincident two-neutron detection in HIME alone and in combination with NEBULA, respectively. In order to reach the same statistical uncertainty of a_{nn}, between $12\,\%$ and $20\,\%$ more two-neutron events in the range $T_{\mathrm{rel}}^{\mathrm{rec}} \in [0\,\mathrm{MeV}, 1\,\mathrm{MeV}]$ are required when one of the neutrons is detected in NEBULA, which results from the loss of resolution. However, the lower resolution is overcompensated by the gain of efficiency, amounting to factor of 6.25 (see Tab. 3.3), which suggests the usage of the two neutron-detection systems together. Still, it is important to note that the development and the construction of HIME are not finished yet, *i.e.*, resolution and efficiency of HIME will most probably be different from the corresponding parameters in the simulations of this work. For instance, the time resolution of the individual scintillation modules is $100\,\mathrm{ps}$ in the simulation, which is a conservative estimation.

If the two neutron-detection systems are used together, the distance between the HIME walls should be chosen as small as possible in order to maximize the resolution. Conveniently, this matches the proposal in Ref. [67] for another experiment that is part of the same campaign.

3.6. Deconvolution of a Measured Spectrum

The influence of the resolution r on the true probability distribution p of a quantity q can be described as the convolution

$$m(q) = \int_{-\infty}^{\infty} r(q - q') \cdot p(q') \, \mathrm{d}q'. \tag{3.18}$$

In many cases, the resolution r is modeled as a Gaussian with width σ. If p shows a sharp peak at a certain $q' = q'_0$, the resolution leads to a broadening of that structure.

This formula can be applied if the detector resolution does not change significantly around the peak at q'_0. In the case of a Gaussian, this would mean for σ to be constant. In some cases however, this assumption is not valid. Besides, in general, a measured spectrum is not only affected by the resolution, but also by the efficiency, the limited acceptance and other arbitrarily complicated distortions that result from the detection system. These effects are summarized in the term *setup response*. The distortion of the true distribution caused by the setup response can be described by

$$m(q) = \int_{-\infty}^{\infty} f_r(q, q') \cdot p(q') \, \mathrm{d}q', \tag{3.19}$$

where f_r denotes the response function. In contrast to the function r in Eq. 3.18, f_r does not simply depend on the difference $q - q'$, but can be an arbitrarily complicated function of q and q'.

Since it is impossible to measure an infinite number of values q, a different form of Eq. 3.19 is needed which can be applied to a discrete spectrum with a finite range. It is given by

$$m_j = \sum_{i=1}^{d_{\text{gen}}} \frac{R_{ij}}{N_i^{\text{gen}}} \cdot p_i, \quad j \in \{1, 2, \ldots, d_{\text{rec}}\}, \tag{3.20}$$

where d_{gen} and d_{rec} are the dimensions of the generated and the reconstructed spectrum, respectively. Corresponding to that, R is the response matrix of dimension $d_{\text{gen}} \times d_{\text{rec}}$. The slices of R are normalized with the number of events N_i^{gen} that were generated by the simulation in each bin i. The task of the experimentalist is to infer the true distribution p from the measurement m, in order to reach comparability to theoretical predictions or to experimental results that originate from other setups. Due to the similarities of Eqs. 3.18-3.20, this procedure is called *deconvolution* in the following, although it differs from the same-named mathematical operation.

From a purely mathematical point of view, the true distribution p could be obtained from Eq. 3.20 by matrix inversion. In practice however, R usually is determined with Monte Carlo methods, leading to statistical fluctuations. By inversion of R, the fluctuations are increased and often make it impossible to extract the desired information from the observed spectrum. Even negative entries in the resulting distribution can occur. Moreover, there is no guarantee for the inverse of R to exist.

3.6.1. Iterative Bayesian Deconvolution

A different deconvolution method, which is based on Bayes' theorem, has been proposed in Refs. [94, 95]. In this formalism, each matrix element of the response matrix is treated as the non-normalized probability that the value of a certain quantity is reconstructed within the range of an *effect* bin $j \in \{1, 2, \ldots, n_e\}$, under the condition that the true value has been within the range of *cause* bin $i \in \{1, 2, \ldots, n_c\}$. The quantities n_e and n_c denote the number of effect and cause bins, respectively.

As mentioned above, the response matrix usually is determined via Monte Carlo methods. With the number N_i^{gen} of generated $T_{\text{rel}}^{\text{gen}}$ values in cause bin i, the conditional probabilities

$$P\left(e_j|c_i\right) = \frac{R_{ij}}{N_i^{\text{gen}}} \tag{3.21}$$

can be calculated, expressing the probability for effect e_j to be reconstructed, under the condition that cause c_i has occurred. With summation over all effects, one obtains the reconstruction efficiencies

$$\tilde{\epsilon}_i = \sum_{j=1}^{n_e} P\left(e_j|c_i\right). \tag{3.22}$$

This definition is slightly different from the two-neutron reconstruction efficiency of Eq. 3.14, as the sum is cut at n_e. The efficiency is required here in the form of Eq. 3.22, because it is not possible to perform the deconvolution with a response matrix of infinite size. In Eq. 3.14 however, one simply counts the number of reconstructed events for each cause bin i.

The efficiency $\tilde{\epsilon}$ fulfills

$$0 \leq \tilde{\epsilon}_i = \sum_{j=1}^{n_e} P\left(e_j|c_i\right) \leq 1 \quad \forall i \in \{1, 2, \ldots, n_c\}, \tag{3.23}$$

i.e., sometimes events are generated that do not lead to a count in any of the effect bins.

With the conditional probabilities $P\left(e_j|c_i\right)$, the discrete convolution (Eq. 3.20) can be rewritten as

$$m_j = \sum_{i=1}^{n_c} P\left(e_j|c_i\right) \cdot p_i. \tag{3.24}$$

If the true distribution p was known, one could apply Bayes' theorem on $P\left(e_j|c_i\right)$ in order to determine the corresponding inverse conditional probabilities

$$P\left(c_i|e_j\right) = \frac{P\left(e_j|c_i\right) \cdot p_i}{\sum_{l=1}^{n_c} P\left(e_j|c_l\right) \cdot p_l}. \tag{3.25}$$

This expression gives the probability for each cause i of being responsible for a count in the measured spectrum, under the condition that effect j has been observed in this event. For each of the n_e effects, this equation simply represents Bayes' theorem generalized to an arbitrary number of disjoint events, *i.e.*, n_c causes in this case, with posterior $P\left(c_i|e_j\right)$, likelihood p_i, prior $P\left(e_j|c_i\right)$ and normalization factor $\sum_{l=1}^{n_c} P\left(e_j|c_l\right) \cdot p_l$.

Equation 3.25 implies

$$\sum_{i=1}^{n_c} P\left(c_i|e_j\right) = 1 \quad \forall j \in \{1, 2, \ldots, n_e\}, \tag{3.26}$$

i.e., there cannot be an entry in the reconstructed spectrum without a generated event[2].

When these inverse conditional probabilities as defined in Eq. 3.25 are known, it is possible to calculate

$$p_i = \frac{1}{\tilde{\epsilon}_i} \cdot \sum_{j=1}^{n_e} P\left(c_i|e_j\right) \cdot m_j = \sum_{j=1}^{n_e} D_{ji} \cdot m_j, \tag{3.27}$$

---

[2] Note the difference to Eq. 3.23.

where the deconvolution matrix D is introduced with the matrix elements

$$D_{ji} = \frac{P\left(c_i|e_j\right)}{\tilde{\epsilon}_i}. \tag{3.28}$$

At a first look, the approach of using Eqs. 3.25 and 3.27 does not seem helpful, because the true distribution p occurs in Eq. 3.25. However, if the deconvolution $p^{(n+1)}$ is closer to p than the spectrum $p^{(n)}$ of the current iteration n, an iterative solution can be applied that starts with a guessed distribution $p^{(0)}$:

1. Normalize the response matrix R with Eq. 3.21 in order to determine the conditional probabilities $P\left(e_j|c_i\right)$. Calculate the efficiencies $\tilde{\epsilon}_i$ using Eq. 3.22.

2. Choose a normalized probability distribution $p^{(0)}$ as an initial guess for the true distribution.

3. Calculate the deconvolution matrix $D^{(n)}$ of iteration n from $P(e_j|c_i)$ and $p^{(0)}$ using Eqs. 3.25 and 3.28.

4. Apply $D^{(n)}$ on the probability distribution m following Eq. 3.27 in order to obtain the deconvolution of the next iteration $p^{(n+1)}$.

5. Check if convergence is reached using a suitable exit condition. If that is not the case, go back to (3.) and replace $p^{(n)}$ by $p^{(n+1)}$. Otherwise, $p^{(n+1)}$ is the result of the iterative Bayesian deconvolution.

This leads to a sequence of distributions which can be defined recursively as

$$
\begin{aligned}
p^{(0)} &= \text{uniform distribution or an arbitrary model,} \\
p_i^{(n+1)} &= \frac{p_i^{(n)}}{\tilde{\epsilon}_i} \sum_{j=1}^{n_e} \frac{P\left(e_j|c_i\right) \cdot m_j}{\sum_{l=1}^{n_c} P(e_j|c_l) \cdot p_l^{(n)}}.
\end{aligned} \tag{3.29}
$$

Results and possible issues of applying this method on simulated data are presented and discussed in Sec. 3.7.

The Bayes formalism allows for a thorough analysis of statistical uncertainties. From Eq. 3.29, explicit formulas giving the covariance matrix of the deconvolution can be derived, which is shown in Sec. 3.6.2.

The deconvoluted spectrum can be compared directly to theoretical predictions, for instance with a χ^2 test. If the determination of continuous values of a_{nn} is desired, one can use the same principle as in Eq. 3.11, but with the original $\rho_{a_{nn}^{(1)}}\left(T_{\text{rel}}\right)$ and $\rho_{a_{nn}^{(2)}}\left(T_{\text{rel}}\right)$ as shown in Fig. 1.4 instead of the distorted spectra $\tilde{\rho}_{a_{nn}^{(1)}}\left(T_{\text{rel}}\right)$ and $\tilde{\rho}_{a_{nn}^{(2)}}\left(T_{\text{rel}}\right)$, *i.e.*,

$$
\rho_{\text{fit}}\left(T_{\text{rel}}\right) = p_s \cdot \left(\rho_{a_{nn}^{(1)}}\left(T_{\text{rel}}\right) + p_m \cdot \left(\rho_{a_{nn}^{(2)}}\left(T_{\text{rel}}\right) - \rho_{a_{nn}^{(1)}}\left(T_{\text{rel}}\right)\right)\right). \tag{3.30}
$$

The function ρ_{fit} is fit to the deconvoluted spectrum and a_{nn} can be determined as before with Eq. 3.12 using the mixing parameter p_m.

3.6.2. Calculation of Statistical Uncertainties

The fact that the count numbers of cause bins are correlated makes the calculation of their uncertainties more complicated. The correlations, resulting from the influence of the response matrix, can be taken into account by including covariance matrices in the uncertainty estimation.

This procedure follows Refs. [94–96] and is described in detail in this section and App. A.

The covariance matrix $\Sigma_{p^{(n+1)}}$ of the deconvoluted spectrum $p^{(n+1)}$ is given by

$$\Sigma_{p^{(n+1)}} = J_{p^{(n+1)}}\left(m, P\right) \cdot \Sigma_{m,P} \cdot J^{\mathrm{T}}_{p^{(n+1)}}\left(m, P\right), \tag{3.31}$$

where $\Sigma_{m,P}$ is the covariance matrix for all measured and generated values. In order to propagate them to $\Sigma_{p^{(n+1)}}$, the Jacobi matrix $J_{p^{(n+1)}}$ is required. It contains the derivatives

$$\frac{\partial p_i^{(n+1)}}{\partial m_y} \quad \text{and} \quad \frac{\partial p_i^{(n+1)}}{\partial P\left(e_y | c_x\right)},$$
$$\text{where } i \in \{1, 2, \ldots, n_c\} \quad \text{and} \quad x, y \in \{1, 2, \ldots, n_e\}.$$

These derivatives are calculated in App. A. In the present case, there are no correlations of entries of m or P, which means that $\Sigma_{m,P}$ is diagonal, *i.e.*, it contains variances only. However, this does not hold for $\Sigma_{p^{(n+1)}}$ in general, because the deconvolution matrix causes correlations of bin contents in the spectrum p. The results determine weights for the fit procedure of the theoretical calculation to the deconvoluted spectrum.

3.7. Results and Discussion

The iterative Bayesian deconvolution method is applied to simulated data with HIME JP and HIME DE. A first simulation has been performed with a uniform T_{rel} distribution to obtain a response matrix as shown in Fig. 3.2a, but with a larger range of reconstructed relative energies up to 3 MeV. Since no suitable experimental data is available from HIME up to now, a second simulation was done using the hEFT T_{rel} distribution for $a_{nn} = -18.7\,\mathrm{fm}$ (see Fig. 1.4). The spectrum that is reconstructed from the simulation results is inserted for m in Eq. 3.29 in order to replace a real measurement. Both simulations were performed with the QGSP_INCLXX_XS physics list. Thus, if the deconvolution procedure works correctly, it should reproduce $a_{nn} = -18.7\,\mathrm{fm}$ under consideration of the uncertainties.

If the amount of counts in the measurement or in the response matrix is too small, there can occur artifacts in the deconvolution procedure that get enhanced in each iteration, which can affect the convergence behavior of the iterative deconvolution. In the present case, the spectrum m contains 8×10^5 events in the range $T_{\mathrm{rel}} \in [0\,\mathrm{MeV}, 1\,\mathrm{MeV}]$, which caused the deconvolution results to diverge, as shown by the blue curve in Fig. 3.11. For $p^{(0)}$, the first n_c bins of m are inserted[3]. Since the response matrix (see Fig. 3.2a) shows such a strong correlation, this is a reasonable choice for $p^{(0)}$.

In Fig. 3.12, the deconvoluted spectrum of the 15th iteration is shown, *i.e.*, after application of Eq. 3.29 for 15 times on the spectrum m. Fitting the function defined in Eq. 3.30 to the deconvoluted spectrum using the hEFT curves $\rho_{-18.7\,\mathrm{fm}}$ and $\rho_{-16.7\,\mathrm{fm}}$ yields $a_{nn} = -18.42(26)\,\mathrm{fm}$. The correlations of bins were neglected in the fit procedure. Of course, without convergence, there arises the question of after how many iterations to exit the deconvolution loop, which cannot be answered conclusively at this point.

In order to reach convergence, one can flatten the deconvoluted spectra by fitting a model to them after each iteration and to insert the fit result

---

[3] As empty bins will remain empty during the deconvolution process, the most simple alternative distribution that could be passed to the deconvolution algorithm is a nonzero uniform one.

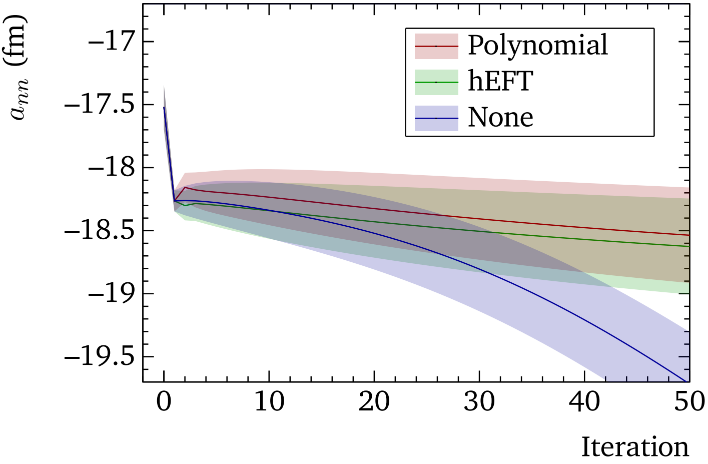

Figure 3.11.: Iterative Bayesian deconvolution with polynomial regularization (red), hEFT regularization (green) and without any regularization (blue). As initial guess $p^{(0)}$, the first n_c bins of the reconstructed spectrum from the simulation with $a_{nn} = -18.7\,\mathrm{fm}$ are used in all cases.

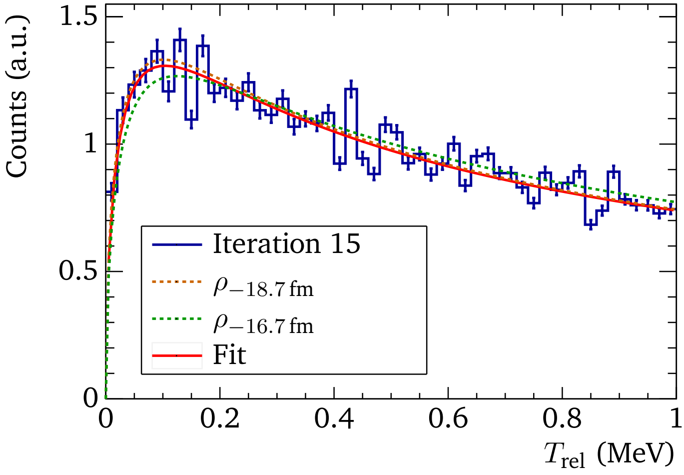

Figure 3.12.: Result of iteration 15 of the Bayesian deconvolution applied to a simulation that uses the hEFT spectrum for $a_{nn} = -18.7\,\text{fm}$ to generate T_{rel} values. The red curve represents the fit function defined in Eq. 3.30, where $\rho_{-18.7\,\text{fm}}$ and $\rho_{-16.7\,\text{fm}}$ are inserted for $\rho_{a_{nn}^{(1)}}$ and $\rho_{a_{nn}^{(2)}}$, respectively.

in the next iteration. This procedure, called *regularization*, can be done with a theoretical calculation, or for example a polynomial of low degree. In the present case (see Fig. 3.11), a linear combination of the hEFT calculations $\rho_{-18.7\,\mathrm{fm}}$ and $\rho_{-16.7\,\mathrm{fm}}$ is used as well as a polynomial[4] of the form $f(T_{\mathrm{rel}}) = \sum_{i=-1}^{3} a_i T_{\mathrm{rel}}^i$, where the a_i are fit parameters. It should be noted that the choice of such a model is ambiguous and introduces constraints on the possible shapes that the deconvoluted spectrum can have. In all cases, the last iteration is done without regularization.

As a result of the flatting in each iteration, a_{nn} changes only slowly above a small number of iterations. In the present case, after $a_{nn} = -18.7\,\mathrm{fm}$ is reached under consideration of the uncertainties, the deconvolution results stay consistent with that value when more iterations are performed.

Aside of the regularization method, the guessed spectrum leads to systematic uncertainties. Fig. 3.13 shows a comparison of three different choices for $p^{(0)}$, using polynomial regularization in all cases: a uniform distribution, the reconstructed spectrum resulting from a simulation with $a_{nn} = -18.7\,\mathrm{fm}$ and the hEFT calculation for $a_{nn} = -20.7\,\mathrm{fm}$. The differences between the individual deconvolution results are only significant in the first few iterations and do not affect the convergence behavior.

In Sec. 3.5.3, the theoretical spectra $\rho_{a_{nn}^{(1)}}$ and $\rho_{a_{nn}^{(2)}}$ are convoluted with the setup response and the results $\tilde{\rho}_{a_{nn}^{(1)}}$ and $\tilde{\rho}_{a_{nn}^{(1)}}$ are fit to the measurement. In this section, the opposite is done (compare Figs. 3.9 and 3.12): the effects of the setup response are removed from the measurement in order to obtain the original distribution, which $\rho_{a_{nn}^{(1)}}$ and $\rho_{a_{nn}^{(2)}}$ can be fit

---

[4] The function shown here is a Laurent polynomial. For the sake of simplicity, it is just referred to as polynomial.

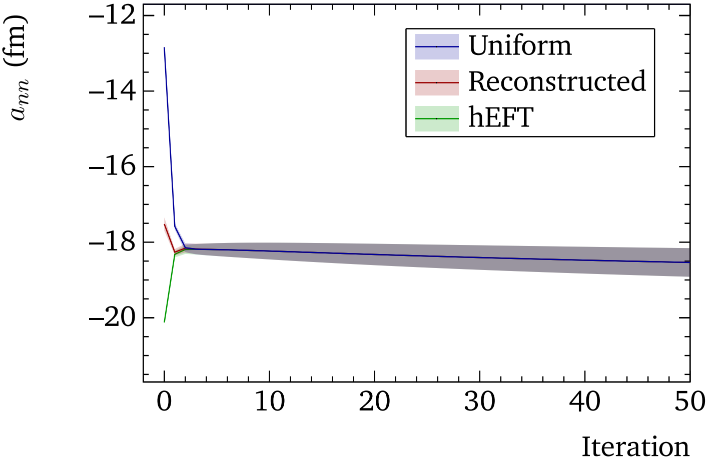

Figure 3.13.: Iterative Bayesian deconvolution using a uniform distribution as initial guess $p^{(0)}$ (blue), the reconstructed spectrum from a simulation with $a_{nn} = -18.7\,\mathrm{fm}$ in the range $T_{\text{rel}}^{\text{rec}} \in [0\,\mathrm{MeV}, 1.5\,\mathrm{MeV}]$ (red) and the hEFT calculation for $a_{nn} = -20.7\,\mathrm{fm}$ (green). In all cases, polynomial regularization is applied.

directly to.

Since for all simulations T_{rel} values are generated in the range $[0\,\mathrm{MeV}, 1.5\,\mathrm{MeV}]$ only, the deconvoluted spectrum is cut sharply at $1.5\,\mathrm{MeV}$, while the reconstructed spectrum decreases continuously around that point. In order to avoid effects on the fit results that originate from these cutoffs, only the range $T_{\mathrm{rel}} \in [0\,\mathrm{MeV}, 1\,\mathrm{MeV}]$ is fit. Due to the small sensitivity to a_{nn} above that range and the finite acceptance of the setup, the fit range is expected to be similar in the analysis of the experimental data.

For the two approaches presented in this section and Sec. 3.5.3, respectively, the determined statistical uncertainties are of comparable magnitudes. In both cases, systematic uncertainties appear as well.

However, since applying the setup response to a theoretical calculation is much simpler and can be more reliable than the deconvolution procedure, there arises the question why deconvoluting can be useful at all. In fact, in many cases the former method should be preferred, but there are counterexamples, such as:

- The deconvolution is useful for obtaining an estimate of how the true distribution should look like.
- If one wants to directly compare data from two experiments with different detector systems, there is no alternative.
- It is convenient to have a final experimentally obtained spectrum without the the need of keeping the detailed information about the setup response. This might be particularly useful if one wants to review experimental data after a longer period of time, for example when new theoretical advancements have been made. If theoretical predictions are compared to experimental data without corrections

for the response, misinterpretations can be the consequence.

In summary, the iterative Bayes formalism provides a versatile deconvolution method: it can be applied to different detector systems and keeps working if the detector parameters, such as resolution or dimensions, are changed. However, complications might be caused by the fact that the Bayesian deconvolution leads to correlated bins in the resulting spectrum, which is typical for deconvolution methods in general. If these correlations are non-negligible, they have to be accounted for in the comparison with a theoretical prediction or with different experimental data.

The Bayesian approach is able to give reliable results if statistics are large in both the measurement and the simulation, or if one knows at least roughly what shape the final spectrum should have. In the latter case, an appropriate function can be used for smoothing in each iteration and thereby prevent strong statistical oscillations to occur. If there is no such knowledge and the amount of events is too small, convergence cannot be guaranteed and one has to solve the problem of finding an appropriate exit condition for the deconvolution loop.

A consistent calculation of statistical uncertainties is possible with the calculations presented in Sec. 3.6.2 and App. A. In the present case, the correlations between individual bins have been neglected in the fit procedure. Besides the statistical uncertainties, systematic ones appear due to imprecisions in the simulation and the different choices for the initially guessed spectrum.

The deconvolution itself has very short computation times, because essentially it only applies Eq. 3.29 in each iteration. Besides, it does not need to process any information on an event-by-event basis, but operates on spectra and matrices only. However, the complexity of calculating Eq.

A.2d in the uncertainty calculation increases steeply with $n_c^3 \times n_e^2$.

Figures 3.11 and 3.12 show that the assumption of $a_{nn} = -18.7\,\mathrm{fm}$ can be reconstructed under consideration of the uncertainties using the analysis methods presented in this chapter, *i.e.*, based on simulations, the self-consistency of the neutron reconstruction in combination with the deconvolution method was validated successfully.

4. Setup and Testing of the Neutron Detector HIME

In order to reach sensitivity to the neutron-neutron scattering length, a determination of relative energies with high resolution in the small range from 0 MeV to 1 MeV is required. To this respect, the experimental method presented in this work has the following advantages: firstly, it is based on an invariant-mass analysis, since the momentum vectors of the neutrons after the reaction can be determined from direct ToF and position measurements. In comparison to the missing-mass method, this leads to a higher resolution: typically, an improvement by one order of magnitude can be achieved. Besides, the free two-neutron systems are created with high velocity in the laboratory system, so that no energy-dependent detection-efficiency corrections are necessary. Finally, the new neutron detector "high-resolution detector array for multi-neutron events" (HIME) will be used. At the SAMURAI setup of RIBF in Japan (HIME JP), a prototype of HIME has been built and an extension of the detector (HIME DE) is currently under construction at IKP.

This chapter focuses on the working principle, the assembly, the testing and the calibration of HIME and its modules. As a part of this work, the readout electronics (see Sec. 4.1), which have been developed at "Gesellschaft für Schwerionenforschung" (GSI) in Germany, were sent to Japan, where the full prototype was equipped with it and brought into operation. For HIME DE, several of the individual components were tested for the first time.

Data from cosmic particles were taken and analyzed, which allowed for position and energy calibrations (see Sec. 4.2 for HIME JP and Sec. 4.3 for HIME DE). The software used for the data analysis and the calibration of HIME is based on ROOT [89] and was developed in this work.

4.1. Neutron-Detection Principle

HIME will consist of two separate arrays of EJ-200 [75] plastic-scintillator bars that are based on polyvinyl toluene, called *detector walls* in the following. To each scintillator, two Hamamatsu PMTs [97] are connected.

In its current state (see Fig. 4.1a), HIME JP consists of two detector walls, each one containing five layers of ten scintillators. The individual layers are aligned vertically and horizontally in alternating order, resulting in a cross shape. For the final configuration, 96 of them will be rearranged to a single detector wall of four layers. Another detector wall, HIME DE, is under development and construction at IKP in Germany and will be shipped to Japan afterwards. In the simulation (see Sec. 3.1), HIME DE is implemented with seven layers, but corresponding to the most recent plannings, up to four additional ones might be added. Each layer will contain 24 plastic-scintillator bars and the two walls of HIME will have a cuboid shape. The orientation of the scintillator bars of different layers will also be alternately vertical and horizontal in the final setup, which has advantages with respect to the calibration of HIME (see Sec. 4.2).

The geometries of the plastic-scintillator bars of HIME JP and HIME DE

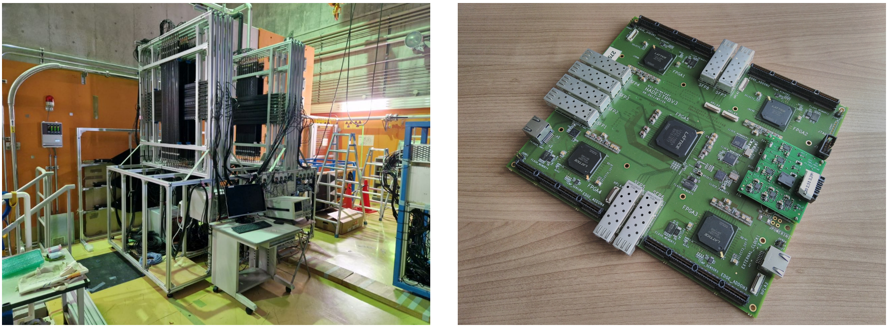

(a) HIME JP in October 2022.

(b) TRB3 board.

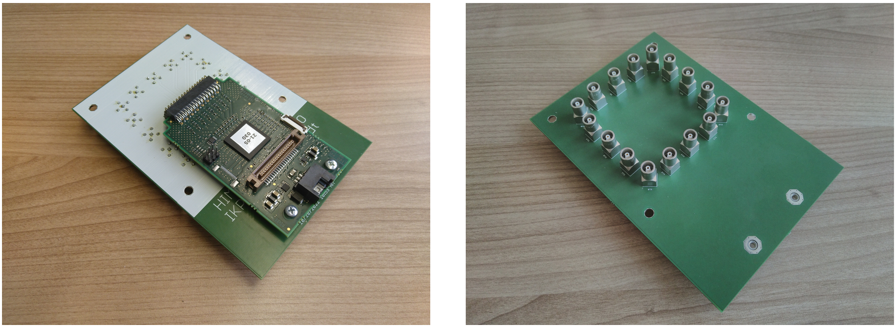

(c) LEMO-to-PaDiWa adapter board with a PaDiWa board attached to it.

(d) Bottom side of the LEMO-to-PaDiWa adapter board.

Figure 4.1.: HIME JP in October 2022 and HIME-readout electronics.

are slightly different. While the central cuboid-shaped central part is of the dimensions $100\,\mathrm{cm}$ (length) $\times\ 4\,\mathrm{cm}$ (width) $\times\ 2\,\mathrm{cm}$ (depth) in both cases, the joints that optically connect to the PMTs differ: in HIME JP, their cross section changes from rectangular to circular and they cannot create scintillation light. In HIME DE however, the joints and the cuboid-shaped part are made of a single piece of scintillation material. The cross section is rectangular everywhere, but is reduced linearly from $4\,\mathrm{cm} \times 2\,\mathrm{cm}$ to $2.2\,\mathrm{cm} \times 2\,\mathrm{cm}$ at the two joints (see Fig. 4.2). In both cases, the joints have a length of $5\,\mathrm{cm}$.

The scintillators of HIME JP are wrapped in black foil in order to prevent light sources around the detector from triggering the PMTs. The foil leads to a distance of $2\,\mathrm{mm}$ between neighboring plastic scintillators. The modules that are part of HIME DE are wrapped in two layers of aluminized Mylar foil of $6\,\mathrm{\mu m}$ thickness only, which prevents photons from entering neighboring modules, but is not sufficient to shield light from strong external sources. Therefore, the modules will be mounted inside a light-tight box.

In order to create a signal, a neutron needs to scatter off a charged particle and transfer a sufficiently large fraction of its kinetic energy, so that the charged particle can excite enough scintillation centers to lead to a detectable light flash. In the ideal case, the neutron centrally hits a proton, since protons have a particularly large penetration depth and cause the largest light output in comparison to heavier nuclides. The light flashes are converted to electrical pulses by the two PMTs of each scintillator bar. The voltages applied to the PMTs of HIME are typically between $-950\,\mathrm{V}$ and $-1500\,\mathrm{V}$, *i.e.*, the pulses have negative polarity.

The electric pulses are sent to the PaDiWa front-end boards [98] (see Fig. 4.1c), which serve as amplifiers and time-over-threshold (ToT) discriminators, *i.e.*, they convert the analogue signals to logical ones.

Each board detects both rising and falling signals in up to 16 channels. The front-end boards are meant to be spatially close to the PMTs in order to limit the influence of noise on the analogue signals. The PMTs can be connected to the LEMO-to-PaDiWa adapter boards as shown in Figs. 4.1c and 4.1d, which have been developed at the electronics workshop of IKP.

As time-to-digital converters (TDCs), "TDC readout boards" (TRB3) [99, 100] are used (see Fig. 4.1b), which have been developed by the TRB group at GSI in Darmstadt, Germany. The TRB3 board is equipped with five "field programmable gate arrays" (FPGAs) that allow for the programming of logic gates. In this work, they are used to implement the trigger logic for all incoming signals from the PMTs. On the FPGA in the center of each TRB3 board (called *central* FPGA), the "central trigger system" (CTS) is running. It coordinates the four other FPGAs (called *peripheral* FPGAs) and communicates with the DAQ "data acquisition backbone core" (DABC) [101, 102]. To each of the peripheral FPGAs, up to three PaDiWa front-end boards can be connected, resulting in 48 channels, which is the exact amount required to operate a complete layer of HIME.

In the current trigger scheme, a trigger signal will be sent when two PMTs of the same module detect a light flash coincidently. The size of the coincidence window is given by the ToT of the first signal, plus an additional time interval that can be set manually. All modules are read out when there is a coincidence in at least one of them. The software that currently runs on the FPGAs only allows to set this triggering scheme for 32 channels of each one, corresponding to 16 modules. To cover the remaining 16 channels per FPGA, an "or" trigger is implemented between all PMTs on the bottom or left side and all on the top or right side. In the future, the FPGAs software should be modified in order to avoid complications in the calibration or data analysis and to implement more complicated triggers, such as for combinations of modules or for entire detector walls.

The data arriving at the computer on which the DABC runs is written to files of the format “HADES list mode data” (HLD) [103]. In order to import the data into the ROOT data-analysis framework, they are converted to ROOT files using the “GSI object oriented on-line off-line system” (Go4) software [101, 102], which is called *unpacking*.

In Secs. 4.2 and 4.3, it is shown how information on position and energy deposition of particles in the detector as well as the corresponding uncertainties can be inferred from the data.

4.1.1. Position and ToF Measurements

Assume a scintillator bar of length L, where the two PMTs, denoted by PMT 0 and PMT 1, are located at the positions $-L/2$ and $L/2$, respectively (see Fig. 4.2). Then, the light flash caused by a hit at position $x_h \in [-L/2, L/2]$ has to cross the distances $L/2 + x_h$ and $L/2 - x_h$ in order to reach PMT 0 and 1, respectively. Consequently, it will be detected at the times

$$t_0 = \frac{L/2 + x_h}{v_\text{eff}} \quad \text{and} \tag{4.1a}$$

$$t_1 = \frac{L/2 - x_h}{v_\text{eff}} + t_\text{offs}, \tag{4.1b}$$

where v_eff is the effective velocity of light and t_offs accounts for the offset between the time measurements t_0 and t_1 in the two PMTs of a module. The size of t_offs depends among others on the lengths of the cables that connect the PMTs with the PaDiWa boards. The determination of the parameters v_{eff} and t_{offs} for all modules of HIME is done as a part of the position calibration (see Sec. 4.2.3).

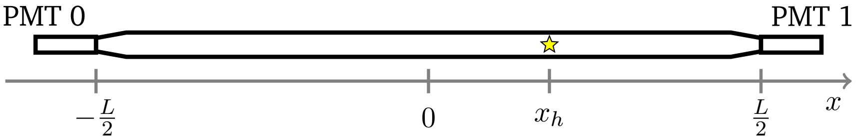

Figure 4.2.: Schematic drawing of a HIME DE module. The position x_h of a hit inside the module can be calculated from the time difference of the electric pulses that are emitted by the two PMTs 0 and 1 after the scintillation light has arrived there. The scintillator bar itself is drawn to scale. Its length is $L = 110\,\text{cm}$ and its width $4\,\text{cm}$.

By calculating the difference of the two time measurements in Eqs. 4.1a and 4.1b, one obtains

$$\Delta t := t_0 - t_1 = \frac{L/2 + x_h}{v_{\text{eff}}} - \frac{L/2 - x_h}{v_{\text{eff}}} - t_{\text{offs}} = 2\frac{x_h}{v_{\text{eff}}} - t_{\text{offs}} \quad (4.2a)$$

$$\Rightarrow \quad x_h\left(\Delta t\right) = \frac{v_{\text{eff}}}{2} \cdot \left(\Delta t + t_{\text{offs}}\right). \quad (4.2b)$$

Furthermore, the time of detection measured relative to a different detector such as one of the SBTs, is given by the average of the two time measurements

$$t_{\text{HIME}}\left(t_0, t_1\right) = \frac{t_0 + t_1}{2}. \quad (4.3)$$

Equations 4.2b and 4.3 show that after calibration, the time of detection essentially is given by the sum of the time measurements t_0 and t_1, while the position x_h along the orientation of a certain module can be determined by their difference. The remaining two spatial coordinates are constrained only by the dimensions of the scintillation module. Usually, the position variables that cannot be determined using time measurements are set to uniformly distributed random values that range over the dimensions of the module. This procedure serves to prevent artifacts from occurring in the data that result from the discreteness of two of the spatial coordinates.

The high granularity of the detector is advantageous for the resolution, which is important for the present experiment, where the sensitivity of the relative-energy spectrum on the neutron-neutron scattering length is contained in the small region from $0\,\text{MeV}$ to roughly $1\,\text{MeV}$.

4.1.2. Energy-Deposition Measurement

The time-over-threshold measurement serves for the determination of the energy deposition of charged particles in the scintillator bars. The energy deposition is a helpful information for identifying the primary interaction points of neutrons in HIME (see Sec. 3.3), but is not used to determine the kinetic energies of neutrons. Since neutrons leave HIME in close to all cases before being stopped, their momenta and kinetic energies are determined from position and ToF measurements instead.

When a charged particle traverses a scintillator bar, it deposits an energy E_dep and thereby creates a light flash that is attenuated exponentially with attenuation constant μ as it spreads through the scintillation material. If enough light remains at the position of PMT $i \in \{0, 1\}$, an electric signal is released.

The total charge q_i of this signal is proportional to the amount of light that has reached the PMT. Therefore, there exist calibration constants

c_0 and c_1 so that

$$q_0 = c_0 \cdot \exp\left(-\mu\left(\frac{L}{2} + x_h\right)\right) \cdot E_{\text{dep}} \quad \text{and} \tag{4.4a}$$

$$q_1 = c_1 \cdot \exp\left(-\mu\left(\frac{L}{2} - x_h\right)\right) \cdot E_{\text{dep}} \tag{4.4b}$$

(see Fig. 4.2), which yields

$$\begin{aligned} q_0 \cdot q_1 &= c_0 \cdot c_1 \cdot \exp\left(-\mu L\right) \cdot E_{\text{dep}}^2 \\ \Rightarrow E_{\text{dep}} &= \sqrt{\frac{q_0 \cdot q_1}{c_0 \cdot c_1}} \cdot \exp\left(\frac{\mu L}{2}\right) . \end{aligned} \tag{4.5}$$

Equation 4.5 shows that E_{dep} could be determined by measurement of the charges q_0 and q_1 with a charge-to-digital converter (QDC). Note that the remaining quantities μ, L and c_i are material and calibration constants. In particular, Eq. 4.5 is independent of the position x_h, despite of the attenuation of light in the scintillator. Moreover, E_{dep} is proportional to $\sqrt{q_0 \cdot q_1}$ up to very high light yields in the scintillators, where the PMTs start to saturate.

In the present case however, the energy deposition can be inferred only from ToT measurements. The combined ToT

$$T = \sqrt{T_0 \cdot T_1}, \tag{4.6}$$

where T_0 and T_1 are the ToT measurements in the respective PMTs, is not proportional to E_{dep}, but can exhibit a more complicated behavior instead which depends on the pulse shape. In Secs. 4.2.5 and 4.3.2, it is shown how polynomials can be determined that approximate the energy calibration functions $T(E_{\text{dep}})$ in certain ToT ranges.

4.1.3. Uncertainties

Following Eq. 4.2b, the uncertainty of the spatial coordinate measured parallel to the orientation of a certain module can be expressed in terms of the time resolution σ_t^{PMT} of a single PMT as

$$\sigma_{\parallel} = \frac{v_{\mathrm{eff}} \cdot \sigma_t^{\mathrm{PMT}}}{\sqrt{2}} \tag{4.7}$$

and with Eq. 4.3, the time resolution of a module is given by

$$\sigma_t^{\mathrm{mod}} = \frac{\sigma_t^{\mathrm{PMT}}}{\sqrt{2}}. \tag{4.8}$$

A conservative value for the time resolution of the scintillator modules is $\sigma_t^{\mathrm{mod}} = 100\,\mathrm{ps}$ and a typical value for the effective velocity of light in a plastic scintillator is $v_{\mathrm{eff}} \approx 0.5\,c$ (see Sec. 4.2.2 and 4.3.1 as well as App. B). Under these assumptions, one obtains

$$\sigma_{\parallel} = v_{\mathrm{eff}} \cdot \sigma_t^{\mathrm{mod}} \approx 1.50\,\mathrm{cm}. \tag{4.9}$$

The other two position coordinates are not available via time measurements, but are constrained exclusively by the dimensions of the scintillator bars. Therefore, the corresponding uncertainties $\sigma_{\perp,w}$ and $\sigma_{\perp,d}$ are given by the standard deviations of uniform distributions, *i.e.*,

$$\begin{aligned} \sigma_{\perp,w} &= \frac{4\,\mathrm{cm}}{\sqrt{12}} \approx 1.15\,\mathrm{cm} \quad \text{and} \\ \sigma_{\perp,d} &= \frac{2\,\mathrm{cm}}{\sqrt{12}} \approx 0.577\,\mathrm{cm}, \end{aligned} \tag{4.10}$$

where the indices w and d are for width and depth of the scintillator bars. Note that, although their origins are different, the uncertainties of the three spatial coordinates as given in Eqs. 4.9 and 4.10 are of comparable magnitudes.

Since the ToF (see Eq. 4.3), the energy deposition (see Eq. 4.6) and the spatial coordinate measured parallel to the orientation of a certain module (see Eq. 4.2b) all result from time measurements, the time resolution of the detector plays a crucial role. For the calibration of HIME, cosmic muons are measured, which can traverse the full detector on straight flight paths and create signals in many neighboring modules.

4.1.4. Cosmic Muons

The particles that are created at astrophysical sources and that travel through interstellar space are called *primary cosmic particles* [33, 104]. During the interaction with interstellar gas, *secondary cosmic particles* are produced. The primary cosmic radiation which arrives at earth often leads to disintegration of nuclei in the atmosphere and thereby to the creation of pions. The pions are not stable, but can decay to muons and muon neutrinos in the reactions

$$\pi^+ \to \mu^+ + \nu_\mu \quad \text{and} \tag{4.11a}$$

$$\pi^- \to \mu^- + \overline{\nu}_\mu . \tag{4.11b}$$

These reactions are responsible for the majority of cosmic muons in the earth's atmosphere. They typically take place at roughly $15\,\mathrm{km}$ above the ground.

At sea level, muons are the most numerous constituents of cosmic radiation. Their intensity is about $I \approx 70\,\mathrm{m}^{-2}\,\mathrm{s}^{-1}\,\mathrm{sr}^{-1}$.

Due to their high mean energy of roughly $4\,\mathrm{GeV}$ in comparison to their rest energy of $0.113\,428\,925\,7(25)\,\mathrm{u}\,c^2$ [33] (about $106\,\mathrm{MeV}$), the muons are highly relativistic: at $4\,\mathrm{GeV}$, the Lorentz factor is $\gamma \approx 38$. Only these high energies make it even possible for muons to reach the earth's ground, because they decay with a lifetime of $2.196\,981\,1(22)\,\mu\mathrm{s}$ [33] via

$$\mu^+ \to e^+ + \nu_e + \overline{\nu}_\mu \quad \text{and} \tag{4.12a}$$

$$\mu^- \to e^- + \overline{\nu}_e + \nu_\mu . \tag{4.12b}$$

Another implication of the typical energies of cosmic muons is that they become *minimum ionizing particles* (MIPs). An MIP has a kinetic energy that makes its energy deposition in matter minimal and nearly constant. In polyvinyl toluene, the polymer which the HIME scintillators are based on, cosmic muons deposit $2\,\mathrm{MeV\,cm^2\,g^{-1}}$ [105].

For the calibration of HIME, one can take advantage of the fact that the energy deposition and the velocity are known: by analyzing the trajectories of cosmic muons through the detector, time, position and energy calibrations can be performed for single modules and the effective velocity of light in the scintillator can be determined. Moreover, cosmic-muon events allow for the synchronization of all HIME modules.

4.2. HIME JP

In this work, HIME JP was taken into operation with the TRB3 electronics that have been sent from Germany. For testing purposes, cosmic muons have been measured. With the recorded data, some of the steps of the calibration procedure can be demonstrated exemplarily.

The full calibration includes the following:

1. Calibration of the TDCs.

2. Position calibration of all modules separately.
3. Synchronization of all modules.
4. Time calibration relative to a different detector that determines the start point of a ToF measurement.
5. Energy calibration.

The first step only involves the TRB3 boards themselves, since it makes use of their internal pulsers (see Sec. 4.2.1).

Step 2 can be done by measuring cosmic muons without beam. The properties that make cosmic muons useful for calibration purposes are described in Sec. 4.1.4. For the calibration procedure, two different approaches are given: a simple, but robust approach is presented in Sec. 4.2.2 and a more complex one relying on muon tracking in Sec. 4.2.3.

Since step 3, the synchronization of all modules, is tested with photons that are created by reactions of an ion beam with a heavy target, no experimental result can be discussed yet, but still the calibration method is outlined briefly in Sec. 4.2.4.

In order to determine neutron momenta, ToF measurements have to be performed. For this purpose, HIME has to be calibrated relative to another detector that defines a start time for each event, which is done in step 4. Usually, photons are used for that like in step 3, since their velocity is constant which leads to a sharp peak in the ToF spectrum.

The last step is the energy calibration (see 4.2.5), which makes use of cosmic muons again: for a given path length inside a scintillator module, the total energy deposition of a muon can be calculated (see Sec. 4.1.4). The results are correlated with the measured ToT, which allows for the determination of a calibration function.

In the following, the details of the individual steps of the calibration are discussed.

4.2.1. TDC Calibration

On each peripheral FPGA of the TRB3 boards of HIME, a TDC is implemented, serving to determine time differences between signals from the PaDiWa boards. The TDCs contain coarse and a fine time counters. The coarse time counter is incremented with a frequency of $500\,\text{MHz}$, *i.e.*, all steps of the fine counter sum up to $5\,\text{ns}$. However, these fine counter steps correspond to time steps of different sizes, which have to be determined in order to guarantee precise time measurements. For this purpose, the TDC internally creates randomly distributed signals for all channels. Then, the amount of signals in each time step is a direct measure for its size, which allows to determine a calibration function that maps time-counter values on time steps.

To measure the time precision of a TDC, one can create electrical pulses and split them in two different cables, where each one is connected to a PaDiWa channel. The time difference of these signals is non-zero in general due to different cable lengths, but it cannot change over time. Still, the distribution of time differences Δt has a non-zero width, as shown in Fig. 4.3, which is caused by imprecisions of the calibration function. The resulting uncertainty of time measurements is of systematic character and can be quantified with the standard deviation of the time-difference distribution. In the present example, a precision of $15\,\text{ps}$ was reached.

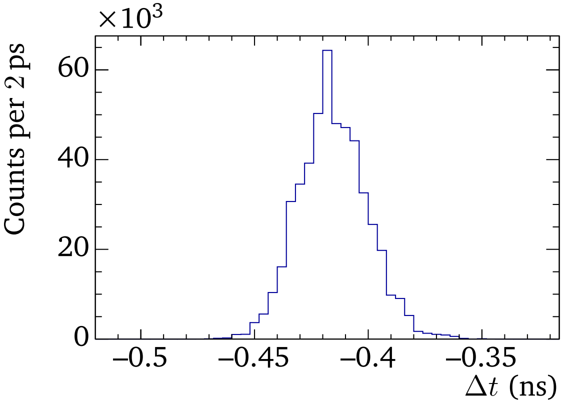

Figure 4.3.: Time-difference distribution of two channels of the same peripheral FPGA, resulting from a single pulser signal. The standard deviation, giving the time precision of the FPGA, is $15\,\mathrm{ps}$ in the present case.

4.2.2. Simple Position Calibration

The position of a hit inside of a HIME module can be determined by the measurement of the time difference between the signals that are detected in the two channels which the PMTs are connected to. The mapping of time differences to positions depends on the cable lengths of the corresponding channels and on the effective velocity of light in the scintillation material, which makes a calibration necessary.

A simple and robust approach of performing a position calibration is to measure background radiation and identify cosmic muon events in the data. For this purpose, the combined ToT is event-wise correlated with the time difference Δt of signals in the two channels of a certain module, which corresponds to the energy deposition and position of a hit, respectively.

The result of such a measurement is shown exemplarily in Fig. 4.4 for module 33 of HIME JP. Around a ToT of $21\,\mathrm{ns}$, the muon events are located, which typically deposit more energy than the terrestrial background radiation does. For low-energetic background, the uncertainty of time measurements is larger, because the influence of noise on the time of the electrical pulse reaching the threshold is larger. Consequently, the Δt distribution is broader at low ToT. Besides, the dependence time measurements on the signal height, called *walk effect*, could contribute to that, if the attenuation of light in the scintillation material is large enough. Otherwise, the walk effect would cancel out, as only differences of time measurements are shown.

The bent form of the correlation plot at lowest ToT values is a consequence of the attenuation of light signals as well: small signals that are created close to one of the ends of a scintillator bar will be attenuated below the threshold until they reach the opposite PMT.

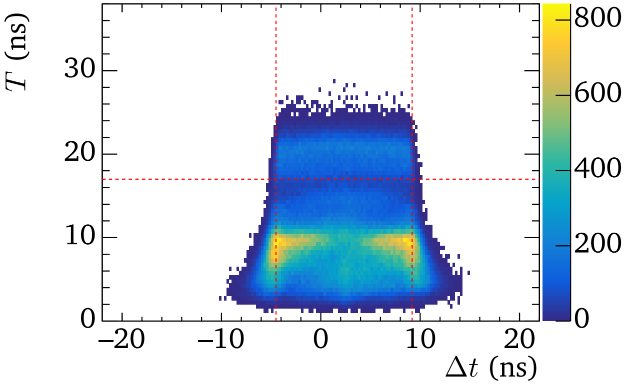

Figure 4.4.: ToT T vs. time difference Δt of module 33 of HIME JP, which is aligned horizontally. Above the horizontal dashed line, cosmic muon events are located. The two vertical lines show the edges of the Δt distribution of muons, which allows for a position calibration.

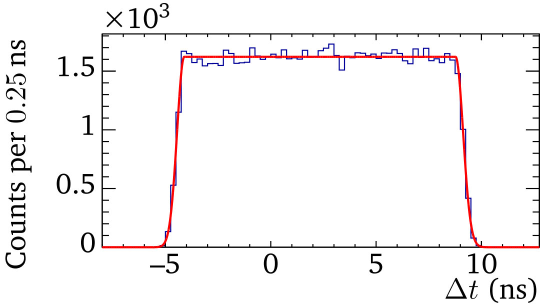

Figure 4.5.: Projection of the cosmic muon events, *i.e.*, the counts above the horizontal dashed line in Fig. 4.4, onto the Δt axis. The red curve represents the fit function defined in Eq. 4.13.

All counts above the horizontal dashed line at $T = 17\,\mathrm{ns}$ are projected onto the Δt axis. To the resulting distribution (see Fig. 4.5), a function of the form

$$f\left(\Delta t\right) = \begin{cases} p_0 \exp\left(-\left(\frac{\Delta t - p_1}{p_2}\right)^2\right), & \text{for } \Delta t < p_1 \\ p_0, & \text{for } p_1 \leq \Delta t \leq p_3 \\ p_0 \exp\left(-\left(\frac{\Delta t - p_3}{p_2}\right)^2\right), & \text{for } \Delta t > p_3, \end{cases} \tag{4.13}$$

is fit with the constraint $p_1 < p_3$. The fit function is composed of two Gaussians with the width p_2 for the edges of the distribution and a constant part for the plateau of height p_0 in the interval $[p_1, p_3]$.

The two vertical dashed lines in Fig. 4.4 show the width of the fit function defined in Eq. 4.13 at half of its maximum, which allows for a position calibration with Eq. 4.2b: the width is inserted for Δt and the corresponding values for x_h are given by $-\frac{L}{2}$ and $\frac{L}{2}$. With the spectrum shown in Fig. 4.5, an effective velocity of light of $146.01(38)\,\mathrm{mm\,ns^{-1}} \approx 0.49\,c$ is found.

This calibration procedure is applied to both walls of HIME JP. The effective velocities of light in the scintillation material are shown in Fig. 4.6 for the first wall of HIME JP and the corresponding distribution of muon hits is depicted in Fig. 4.7. The corresponding results for the second wall can be found in App. B.

4.2.3. Position Calibration using Muon Tracking

A more complicated approach of position calibration makes use of the alternating orientation of the layers of scintillator bars in HIME to re-

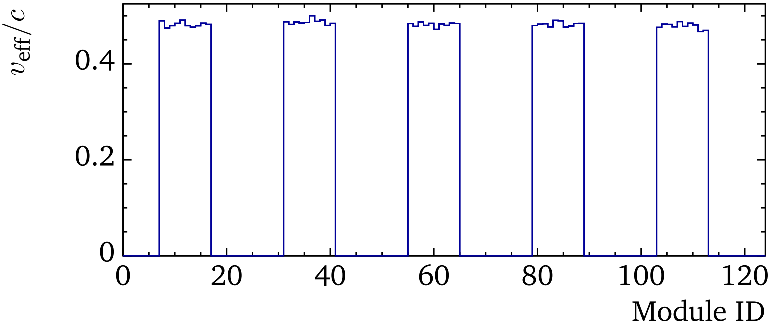

Figure 4.6.: Effective velocities of light in the scintillators of the first wall of HIME JP. Each group of entries corresponds to a layer of plastic scintillators.

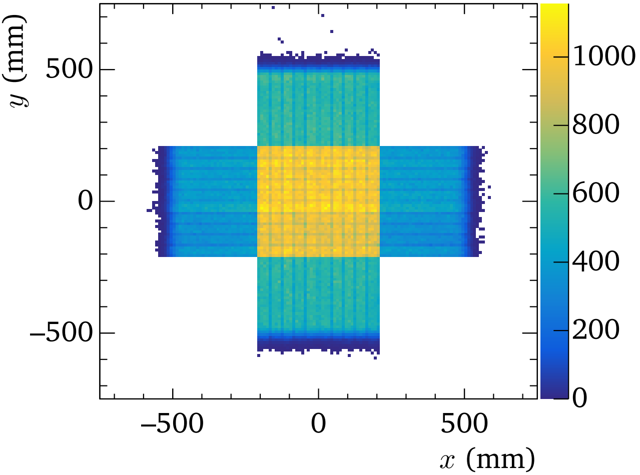

Figure 4.7.: Detection positions of cosmic muons in the first wall of HIME JP.

construct the flight paths of cosmic muons through the detector, called *muon tracking*.

When cosmic muons traverse the detector wall, they can create signals in multiple modules that are located in different layers at different positions z along the beam axis. As already mentioned in Sec. 4.1.1, two of the spatial coordinates of these hits are not measured directly, but are constrained only by the dimensions of the scintillator bars. Therefore, since the positions of all modules are known, one will obtain two sets of points (x_i, z_i) and (y_j, z_j), where $i \in \{1, 2, \ldots, N_v\}$ and $j \in \{1, 2, \ldots, N_h\}$ for N_v hits in vertical modules and N_h hits in horizontal ones. To all coordinates, random values are assigned that are distributed uniformly over the width and the depth of the scintillators. To these points, linear functions are fit, resulting in a complete trajectory $(x(z), y(z))$. For each module that registered a hit in a specific event, the trajectory is evaluated at its position coordinate z and the result is correlated with the time difference Δt of light-signal detection in the two respective PMTs.

The data resulting from this procedure are shown exemplarily for the modules 8 and 32 of the first wall of HIME JP in Fig. 4.8. The former is aligned vertically, the latter horizontally. To these data points, the linear position-calibration function defined in Eq. 4.2b is fit, which allows for the determination of the effective velocity of light in the scintillation material. For the modules 8 and 32, the results are $0.464(25)\,c$ and $0.456(34)\,c$, respectively.

For the position-calibration method presented in this section, the arrangement of scintillators is not optimal, due to the rather small amount of layers in each detector wall: to determine the linear functions $x(z)$ and $y(z)$, there are only 3 and 2 layers, respectively, in the first wall of HIME JP and vice versa for the second wall. Furthermore, the area in which horizontal and vertical modules overlap is only about $420\,\mathrm{mm}$

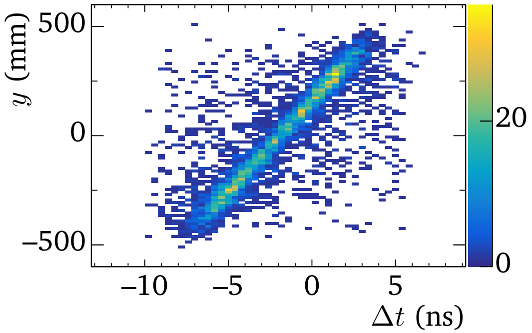

(a) Module 8, aligned vertically.

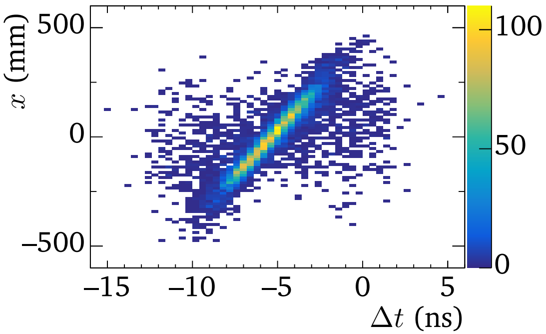

(b) Module 32, aligned horizontally.

Figure 4.8.: Correlations of detection position and time difference of detection in the two PMTs of a vertical (a) and a horizontal (b) module of the first wall of HIME JP.

$\times 420$ mm, including wrapping and gaps between individual scintillators, which limits the range of the correlated data shown in Figs. 4.8a and 4.8b. Therefore, the position calibration from Sec. 4.2.2 is applied to the data for the further analysis.

4.2.4. Synchronization of All Modules

It was mentioned in Sec. 4.1.1 that there exists an offset between the time measurements of the two PMTs of each module, for instance as a consequence of different cable lengths. The same applies for time measurements in different modules, which makes an additional synchronization necessary.

Just like the position calibration method in Sec. 4.2.3, the synchronization of modules can be achieved with muon tracking: at first, an arbitrary module of each detector wall is selected as reference. Then, one calculates the time differences that muons need to travel from one module to another and subtracts them from the measured time differences on an event-by-event basis. The subtraction results will give the calibration constants.

Typically, the quality of synchronization is checked by directing the beam onto a target with a large charge number, such as lead, which creates photons by nuclear excitation and subsequent de-excitation: due to their well-defined velocity, the photons create sharp peaks in the velocity spectra of the neutron detectors, if the synchronization is successful.

4.2.5. Energy Calibration

For the energy calibration, again muon tracking is required. However, since the data is calibrated in position already, one can directly fit linear functions to the previously calculated data points (x, z) and (y, z) for all modules, independent of their alignment inside HIME.

If a muon track is reconstructed successfully in a certain event, its points of intersection with all modules that registered a hit are calculated. Then, from the path length l inside each scintillator, the total energy deposition is calculated via

$$E_{\text{dep}} = l \cdot \frac{\mathrm{d}E}{\mathrm{d}d_p} \cdot \rho, \tag{4.14}$$

where $\frac{\mathrm{d}E}{\mathrm{d}d_p} \approx 2\,\mathrm{MeV\,cm^2\,g^{-1}}$ [105] is the energy deposition per penetration depth d_p (see Sec. 4.1.4) and $\rho \approx 1\,\mathrm{g\,cm^{-3}}$ [75] is the density of the scintillation material EJ-200.

In Figs. 4.9a and 4.9b, the correlation of the calculated energy deposition E_{dep} and the measured ToT T is shown for muons that enter and leave a module on opposite sides. For muons that cross two sides of a module with a common edge, no sufficiently strong correlation is found, most probably since in this case, small uncertainties of the track reconstruction lead to comparably large uncertainties of E_{dep}.

Due to that restriction, the minimal path length inside each scintillator given by its depth, which is $2\,\mathrm{cm}$, resulting in a minimal energy deposition of $4\,\mathrm{MeV}$. In addition to that, thresholds on the ToT are set for the individual modules, which are $2\,\mathrm{ns}$ smaller than for the position calibration. This serves to remove most of the low-energetic terrestrial background without losing information on the correlation of E_{dep} and ToT.

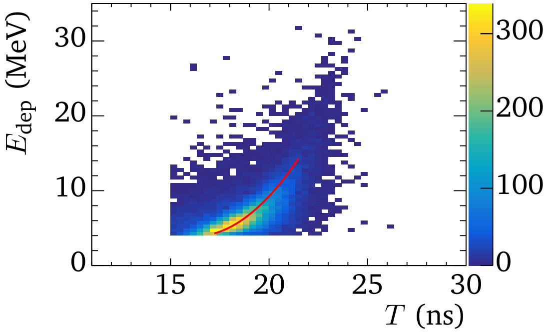

(a) Module 8, aligned vertically.

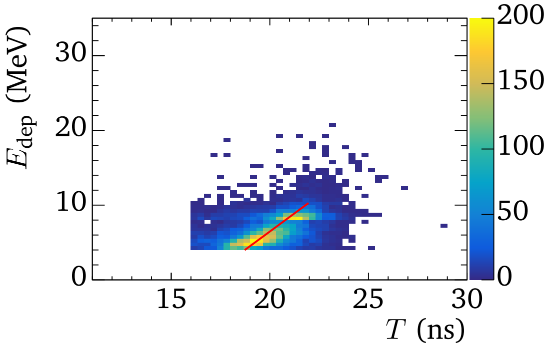

(b) Module 32, aligned horizontally.

Figure 4.9.: Deposited energy E_{dep} vs. ToT T for a vertical (a) and a horizontal (b) module of HIME JP. Depending on their orientation, the modules measure different energy-deposition distributions. The red lines represent the polynomial fits defined in Eq. 4.15.

Since most cosmic muons enter the detector at steep angles relative to the ground (see Sec. 4.3.2), the path length inside vertically aligned scintillators is strongly dependent on only small changes of the angle. Thus, the correlation covers larger ranges of ToT and E_{dep} for vertical modules (see Fig. 4.9a) than for horizontal ones (see Fig. 4.9b).

To the individual one-dimensional distributions of constant E_{dep} in the correlation shown in Figs. 4.9a and 4.9b, Gaussian functions are fit. The positions of their maxima are approximated with the polynomials

$$E_{\mathrm{dep}}\left(T\right) = \sum_{i=0}^{N_{\mathrm{deg}}} p_i T^i, \tag{4.15}$$

where the degree N_{deg} is 2 for vertical modules and 1 for horizontal ones. Estimating the uncertainty of energy deposition $\Delta E_{\mathrm{dep},m}$ with standard deviation of the $E_{\mathrm{dep},m}$ distribution for constant T for a given module m, the corresponding relative resolution is

$$\Delta E^{\mathrm{rel}}_{\mathrm{dep},m} = \frac{\Delta E_{\mathrm{dep},m}}{E_{\mathrm{dep},m}}. \tag{4.16}$$

Evaluating this expression for the modules 8 and 32 at $E_{\mathrm{dep}} = 10\,\mathrm{MeV}$ yields $\Delta E^{\mathrm{rel}}_{\mathrm{dep},8} \approx 23\,\%$ and $\Delta E^{\mathrm{rel}}_{\mathrm{dep},32} \approx 17\,\%$, respectively. It should be noted that all parameters of Eq. 4.15 and the resolution depend on the gain of the respective PMTs, the voltage and the thresholds of the PaDiWa board. Besides, the values given for $\Delta E^{\mathrm{rel}}_{\mathrm{dep},m}$ include all uncertainties of the track reconstruction.

Figures 4.9a and 4.9b show that the response of the scintillation modules to cosmic muons depends on their orientation: in vertically aligned modules, the cosmic muons are better separated in the E_{dep} spectrum from the terrestrial background radiation and cover a wider E_{dep} range, which the energy calibration takes profit from. While for vertical modules, the calibration functions nicely cover the energy range that is relevant for the neutron reconstruction (see Sec. 3.3), a higher upper limit for the horizontal modules is desirable.

The energy resolution of plastic scintillators is comparably low, but it is important to note that the neutron energies are determined via ToF measurements, *i.e.*, the calculation of T_{rel} with Eq. 3.9 does not rely directly on the determination E_{dep}. However, the information about the energy deposition is used in the neutron-reconstruction algorithm as described in Sec. 3.3. As the muon-track reconstruction profits from a higher packing density and a larger total number of scintillator bars, the energy calibration will most probably be improved with respect to both accuracy and covered E_{dep} range when HIME is complete. Besides, for future calibrations of HIME, longer measurements can be conducted than for the first tests with HIME JP.

4.3. HIME DE

In this section, data from test measurements at IKP are presented, which were taken with a single or two of the new modules. Since there exists no mechanical holding structure for a full wall yet, muon tracking is not yet possible as presented for HIME JP in Sec. 4.2.3. Still, using the simple approach introduced in Sec. 4.2.2, the effective velocity of light inside the new scintillators is determined and a position calibration is performed in Sec. 4.3.1 with HIME DE. Even a rough energy calibration is feasible by measuring cosmic muons twice and changing the orientation of the modules in between the two measurements, which is presented in Sec. 4.3.2.

4.3.1. Coincidence Measurement with Cosmic Rays

One of the most simple measurements can be done with a single HIME DE module that detects cosmic radiation only, without any beam or radioactive source. In order to suppress background from the measurement (such as the dark rate of the two PMTs), one can implement a simple “and” trigger for the two PMTs in one of the peripheral FPGAs.

In the present case, a setup with two modules on top of each other is used, as schematically shown in Fig. 4.10. Since most cosmic muons hit the earth’s ground at steep angles, this arrangement suppresses terrestrial gamma background relative to muon events (compare Figs. 4.11 and 4.4), if only coincidences of all four PMTs are selected in the analysis.

In order to perform a position calibration for the coordinate x (see Fig. 4.10), the same procedure as in Sec. 4.2.2 is applied: the data around $T = 20\,\mathrm{ns}$ in Fig. 4.11 are associated with cosmic muons and projected onto the Δt axis. To the resulting projection, the function defined in Eq. 4.13 is fit, which allows to calculate the coordinate x for a given time difference Δt. As before, the other two coordinates are constrained only by the spatial extension of the scintillator bars. The effective velocities of light determined for module 0 and 1 are $0.4672(5)\,c$ and $0.4513(5)\,c$, respectively.

4.3.2. Simple Energy Calibration

The measurement of Sec. 4.3.1 is conducted twice and in between, the scintillator modules are rotated by 90° around themselves such that their orientation stays parallel to the x axis (see Fig. 4.10). Thereby, the muons which approach the setup on flight tracks perpendicular to the

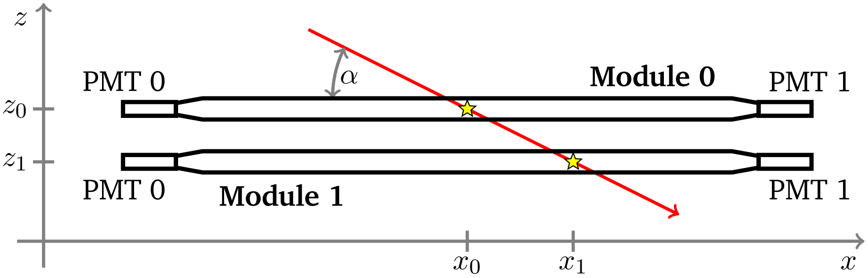

Figure 4.10.: Schematic drawing of two HIME DE modules with a cosmic muon traversing them at the angle of incidence α.

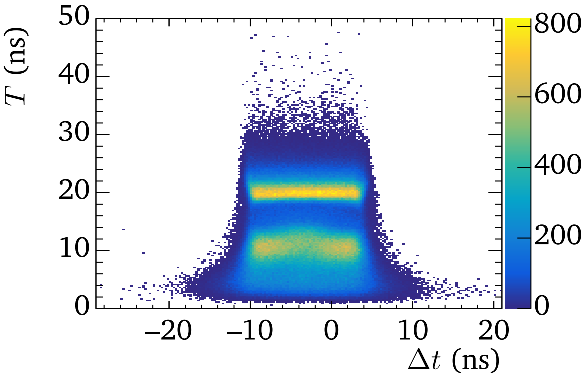

Figure 4.11.: Correlation plot of ToT and time difference of two PMTs for one of the first HIME DE modules taken into operation. To suppress low-energetic terrestrial background radiation, two modules were placed above each other and only coincidences between both were kept for the analysis.

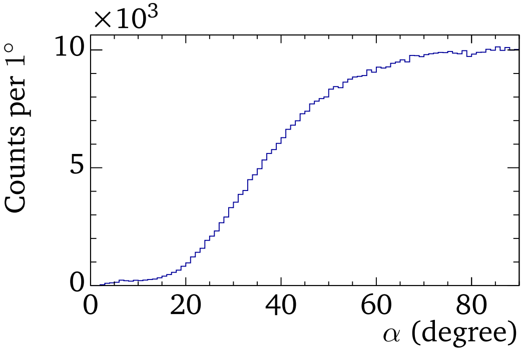

Figure 4.12.: Distribution of angles of muon tracks through the HIME DE modules, measured relative to the scintillator bars and to the desk they were lying on, as shown schematically in Fig. 4.10.

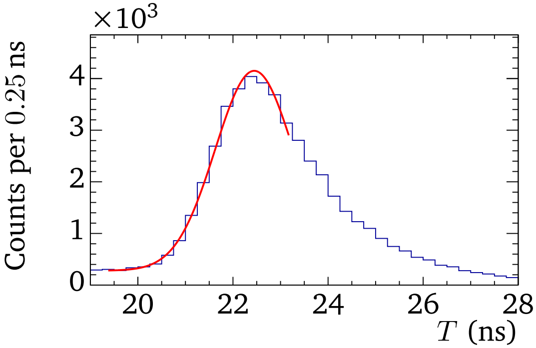

Figure 4.13.: ToT distribution for module 1 of HIME DE around the muon peak.

ground cross $2\,\mathrm{cm}$ of EJ-200 per module in the first measurement and $4\,\mathrm{cm}$ in the second one.

In order to exclude muon hits with larger d_p than $2\,\mathrm{cm}$ or $4\,\mathrm{cm}$ from the calibration, events with $\alpha > 85°$ (see Figs. 4.10 and 4.12) are selected. Mainly to the left edge of the muon peak in the resulting ToT distribution, a Gaussian is fit, as shown exemplarily for module 1 in Fig. 4.13. From the fit parameters, one obtains two values for the ToT T per module, each one corresponding to an E_{dep} obtained from Eq. 4.14. This allows to determine the offset parameter T_{offs} and the slope parameter $\frac{\mathrm{d}E_{\text{dep}}}{\mathrm{d}T}$ of the linear calibration function

$$E_{\text{dep}}\left(T\right) = \left(T - T_{\text{offs}}\right) \cdot \frac{\mathrm{d}E_{\text{dep}}}{\mathrm{d}T}. \tag{4.17}$$

The results are $T_{\text{offs}} = 15.9(16)\,\mathrm{ns}$, $\frac{\mathrm{d}E_{\text{dep}}}{\mathrm{d}T} = 0.99(30)\,\mathrm{MeV\,ns^{-1}}$ for module 0 and $T_{\text{offs}} = 18.5(16)\,\mathrm{ns}$, $\frac{\mathrm{d}E_{\text{dep}}}{\mathrm{d}T} = 0.97(29)\,\mathrm{MeV\,ns^{-1}}$ for module 1.

4.4. Discussion

All 100 modules of HIME JP, as shown in Fig. 4.1a, have been tested with the TRB3 electronics that were brought from Germany. In the current arrangement of HIME JP, there are two separate cross-shaped walls, each one containing 5 layers of 10 scintillator bars. For a precise position calibration with muon tracking however, as described in Sec. 4.2.3, a cuboid-shaped wall with a higher number of layers and bars per layer is more advantageous. Therefore, a more simple approach of position calibration was chosen (see Sec. 4.2.2), which only uses two points in each module to calculate a linear calibration function. Based on the simple position calibration, a second attempt of muon tracking was done, which was used in Sec. 4.2.5 to exemplarily perform an energy calibration for a vertically and a horizontally aligned module.

In the second detector wall, four modules were found that did not work as expected (see App. B). The respective correlation plots of ToT and Δt show structures which lead to imprecisions in the position calibration and cannot be explained from the interaction of cosmic muons or terrestrial background with the scintillation material. There remain 96 working modules, which is exactly the amount that is required for the reassembly of HIME JP to a single wall of four layers. To be prepared if replacements become necessary, the defect ones will still be investigated and repaired if possible.

Two modules of HIME DE were taken in operation with the TRB3 electronics as well and showed promising results from the measurements of cosmic radiation. Since they are not yet integrated in a mechanical holding structure, it was possible to perform an energy calibration just by rotating the scintillators.

The calibration results of HIME JP and HIME DE, shown in Secs. 4.2 4.3, respectively, as well as in App. B demonstrate the fitness of the components of HIME in combination with the electronics from GSI and IKP for a complete neutron-detection system.

5. Summary and Outlook

In this work, a new approach to determine the ${}^1S_0$ neutron-neutron scattering length a_{nn} was presented, which is based on the determination of the two-neutron relative-energy spectra from the ${}^6\mathrm{He}(p{,}p\alpha)2n$ and $t(p{,}2p)2n$ knockout reactions via invariant-mass measurements. Furthermore, the reaction $d(p{,}2p)n$ will serve for calibration and validation purposes. In Chapter 1, the motivation for conducting the experiment was given and the theoretical framework of hEFT was outlined briefly. The experimental details were discussed in Chapter 2, including the beam production, an overview on the components of the setup, the reaction kinematics and the rate estimation.

In Chapter 3, a method to event-wise reconstruct coincident two-neutron events was presented and validated with simulations. For the combination of the simulated setup and the reconstruction algorithm, important properties such as resolution and efficiency were determined.

As a result of the strong constraints that are applied by the reconstruction algorithm on the data, the efficiency for coincident two-neutron detection in the two walls of HIME, without usage of NEBULA, amounts to $0.32\,\%$ only. However, a highly reliable neutron reconstruction is achieved thereby, with only $0.51\,\%$ of unreal two-neutron events in the range $[0\,\mathrm{MeV}, 1\,\mathrm{MeV}]$, which is of high importance for the experiment presented in this work. This percentage can be further reduced by increasing the distance between the two HIME walls. Moreover, a high resolution of the relative energy T_{rel} of $23.2\,\mathrm{keV}$ at $T_{\mathrm{rel}} = 100\,\mathrm{keV}$ is achieved, which still is a conservative estimate resulting from the time resolution of $100\,\mathrm{ps}$ that is chosen for each module in the simulation.

The simulation results suggest that a smaller statistical uncertainty can be reached by moving the two walls of HIME close together and detecting the second neutron in NEBULA, instead of measuring both neutrons in HIME. With NEBULA, the relative-energy resolution is reduced to $34.2\,\mathrm{keV}$ at $T_{\mathrm{rel}} = 100\,\mathrm{keV}$, but this disadvantage is overcompensated by the increased efficiency of $2.0\,\%$ and a cross-talk contribution of only $0.021\,\%$ to the reconstructed spectrum as a result of the large distance between HIME and NEBULA. At this level, the influence of cross-talk on the measurement result is completely negligible.

Still, the question in which configuration to use the individual neutron-detector walls should be reevaluated once the assembly of HIME is completed and its final properties are known, such as the detector geometry and the resolution parameters.

It was shown that the choice of the physics list that models the particle transport in the simulation has a non-negligible influence on the quantity of interest. For that reason, the $d(p,2p)n$ reaction plays a crucial role, as it allows to compare basic observables of single-neutron detection with the simulation, such as multiplicities, energy deposition and efficiency, providing a benchmark for the physics lists. Calibration measurements of that kind will allow to control the systematic uncertainties, which will not only improve the precision of the experiment presented in this work, but also of future experiments with HIME.

The physics-list dependency enters through the setup-response: to compare theoretical calculations with experimental data, one either has to distort the hEFT spectra with the setup response, or remove the effects of the experimental limitations from the measurement. For both methods, solutions were presented exemplarily. Based on simulated data, the self-consistency of the full analysis was demonstrated, including coincident two-neutron identification, determination of the setup response and extraction of values for a_{nn} from the data by comparison of the reconstructed spectra to hEFT calculations.

Chapter 4 focused on the development and the testing of the neutron detector HIME, which will consist of two separate arrays of plastic-scintillator modules. The general neutron-detection principle was presented, which will be realized with the complete HIME. Furthermore, the sources for the uncertainties of time and position measurements were given and the calibration procedure was presented.

A prototype of HIME, HIME JP, has already been built at RIKEN in Japan, while the second one, HIME DE, still is under construction at IKP in Germany. In its current configuration, HIME JP has a cross-shaped active area. In order to increase its acceptance, the modules will be reassembled to form a full cuboid shape.

As a further part of this work, HIME JP was taken in operation with the TRB3 electronics that were brought from Germany after extensive tests of the readout system at IKP. All scintillators and PMTs of HIME JP were tested by detection of cosmic radiation. Out of 100 scintillator modules in total, four were found not to work correctly. Still, the recorded data allowed for position and energy calibrations. The reassembly of the detector will give the opportunity to sort out the defective ones and to investigate them later separately and in more detail.

Using the same type of TRB3 electronics, the first scintillators and PMTs of HIME DE were tested and first data were taken, again with cosmic radiation that was used for calibration purposes. The individual modules will be mounted as soon as the mechanical holding structure is available.

In both HIME JP and HIME DE, the overall data are promising for the construction of a complete high-resolution neutron-detection system. The setup and testing of all components of HIME with the TRB3 electronics will allow for their integration in the same DAQ, which will guarantee consistent digitizing and triggering for all channels.

A. Statistical Uncertainties of the Bayesian Deconvolution

In the following, the derivatives

$$\frac{\partial p_i^{(n+1)}}{\partial m_y} \quad \text{and} \quad \frac{\partial p_i^{(n+1)}}{\partial P\left(e_y|c_x\right)},$$

where $i \in \{1, 2, \ldots, n_c\}$ and $x, y \in \{1, 2, \ldots, n_e\}$, are calculated following Refs. [94–96]. These calculations are required to determine the covariances of the deconvoluted spectra that result from the iterative Bayesian approach as introduced in Sec. 3.6.1. The notation is the same as in Secs. 3.6.1 and 3.6.2.

$$\begin{aligned}\frac{\partial p_i^{(n+1)}}{\partial m_y} = \sum_{j=1}^{n_e} \Bigg[&\frac{P\left(e_j|c_i\right)}{\tilde{\epsilon}_i f_j} p_i^{(n)} \frac{\partial m_j}{\partial m_y} + \frac{P\left(e_j|c_i\right)}{\tilde{\epsilon}_i f_j} m_j \frac{\partial p_i^{(n)}}{\partial m_y} \\ &+ \frac{P\left(e_j|c_i\right)}{\tilde{\epsilon}_i} p_i^{(n)} m_j \frac{\partial f_j^{-1}}{\partial m_y} \Bigg]\end{aligned} \tag{A.1a}$$

$$
\begin{aligned}
&= \sum_{j=1}^{n_e} \left[\frac{P\left(e_j|c_i\right)}{\tilde{\epsilon}_i f_j} p_i^{(n)} \delta_{jy} + \frac{P\left(e_j|c_i\right)}{\tilde{\epsilon}_i f_j} m_j \frac{\partial p_i^{(n)}}{\partial m_y} \right. \\
&\quad \left. - \frac{P\left(e_j|c_i\right)}{\tilde{\epsilon}_i} \frac{p_i^{(n)} m_j}{f_j^2} \cdot \sum_{l=1}^{n_c} P\left(e_j|c_l\right) \frac{\partial p_l^{(n)}}{\partial m_y} \right]
\end{aligned} \tag{A.1b}
$$

$$
= D_{yi} + \sum_{j=1}^{n_e} \left[D_{ji} \frac{m_j}{p_i^{(n)}} \frac{\partial p_i^{(n)}}{\partial m_y} - \sum_{l=1}^{n_c} \frac{m_j \tilde{\epsilon}_l}{p_l^{(n)}} D_{ji} D_{jl} \frac{\partial p_l^{(n)}}{\partial m_y} \right] \tag{A.1c}
$$

$$
= D_{yi} + \frac{p_i^{(n+1)}}{p_i^{(n)}} \frac{\partial p_i^{(n)}}{\partial m_y} - \sum_{j=1}^{n_e} \sum_{l=1}^{n_c} \frac{m_j \tilde{\epsilon}_l}{p_l^{(n)}} D_{ji} D_{jl} \frac{\partial p_l^{(n)}}{\partial m_y} \tag{A.1d}
$$

$$
\begin{aligned}
\frac{\partial p_i^{(n+1)}}{\partial P\left(e_y|c_x\right)} &= \sum_{j=1}^{n_e} \left[\frac{p_i^{(n)} m_j}{\tilde{\epsilon}_i f_j} \frac{\partial P\left(e_j|c_i\right)}{\partial P\left(e_y|c_x\right)} \right. \\
&\quad + \frac{P\left(e_j|c_i\right) p_i^{(n)} m_j}{f_j} \frac{\partial \tilde{\epsilon}_i^{-1}}{\partial P\left(e_y|c_x\right)} \\
&\quad + \frac{P\left(e_j|c_i\right) p_i^{(n)} m_j}{\tilde{\epsilon}_i} \frac{\partial f_j^{-1}}{\partial P\left(e_y|c_x\right)} \\
&\quad \left. + \frac{P\left(e_j|c_i\right) m_j}{\tilde{\epsilon}_i f_j} \frac{\partial p_i^{(n)}}{\partial P\left(e_y|c_x\right)} \right]
\end{aligned} \tag{A.2a}
$$

$$
\begin{aligned}
&= \sum_{j=1}^{n_e} \left[\frac{p_i^{(n)} m_j}{\tilde{\epsilon}_i f_j} \delta_{jy} \delta_{ix} - \frac{P\left(e_j|c_i\right) p_i^{(n)} m_j}{f_j} \frac{\delta_{ix}}{\tilde{\epsilon}_i^2} \right. \\
&\quad - \frac{P\left(e_j|c_i\right) p_i^{(n)} m_j}{\tilde{\epsilon}_i f_j^2} \delta_{jy} p_x^{(n)} \\
&\quad - \frac{P\left(e_j|c_i\right) p_i^{(n)} m_j}{\tilde{\epsilon}_i} \sum_{l=1}^{n_c} \frac{P\left(e_j|c_l\right)}{f_j^2} \frac{\partial p_l^{(n)}}{\partial P\left(e_y|c_x\right)} \\
&\quad \left. + \frac{P\left(e_j|c_i\right) m_j}{\tilde{\epsilon}_i f_j} \frac{\partial p_i^{(n)}}{\partial P\left(e_y|c_x\right)} \right]
\end{aligned}
\tag{A.2b}
$$

$$
\begin{aligned}
&= \frac{\delta_{ix}}{\tilde{\epsilon}_i} \cdot \left(\frac{p_i^{(n)} m_y}{f_y} - p_i^{(n+1)} \right) - \frac{m_y}{f_y} D_{yi} p_x^{(n)} \\
&\quad + \sum_{j=1}^{n_e} \left[- \sum_{l=1}^{n_c} \frac{\tilde{\epsilon}_l m_j}{p_l^{(n)}} D_{jl} D_{ji} \frac{\partial p_l^{(n)}}{\partial P\left(e_y|c_x\right)} + \frac{m_j}{p_i^{(n)}} D_{ji} \frac{\partial p_i^{(n)}}{\partial P\left(e_y|c_x\right)} \right]
\end{aligned}
\tag{A.2c}
$$

$$
\begin{aligned}
&= \frac{\delta_{ix}}{\tilde{\epsilon}_i} \cdot \left(\frac{p_i^{(n)} m_y}{f_y} - p_i^{(n+1)} \right) - \frac{m_y p_x^{(n)}}{f_y} D_{yi} \\
&\quad - \sum_{j=1}^{n_e} \sum_{l=1}^{n_c} \frac{\tilde{\epsilon}_l m_j}{p_l^{(n)}} D_{jl} D_{ji} \frac{\partial p_l^{(n)}}{\partial P\left(e_y|c_x\right)} \\
&\quad + \frac{p_i^{(n+1)}}{p_i^{(n)}} \frac{\partial p_i^{(n)}}{\partial P\left(e_y|c_x\right)}
\end{aligned}
\tag{A.2d}
$$

B. Measurements with the Second Wall of HIME JP

In the following, the results of the test measurements with the second wall of HIME JP (see Fig. 4.1a) are shown. In the correlation plots of ToT T vs. time difference Δt of detection in the PMTs, the four modules 34, 86, 104 and 111 show irregularities. For one of them (see Fig. B.1a), light leakage is the most probable issue. At low ToT, there is a high amount of counts that shows no correlation to Δt.

In the other three cases, the origin of these irregularities is not known yet. The corresponding data, as shown exemplarily for one of the affected modules in Fig. B.1b, strongly differ from the measurement results of the correctly working modules (see Fig. B.1c) and cannot be explained by cosmic radiation or background.

The position calibration is applied to all modules, including the defective ones. The resulting effective velocities of light v_{eff} are shown in Fig. B.2 and the detection positions of cosmic muons in Fig. B.3. The defective modules lead to non-uniform time-difference spectra, which can cause imprecisions in the position calibration functions (see Eq. 4.13), affecting the determination of v_{eff}. These imprecisions propagate to the data shown in Fig. B.3.

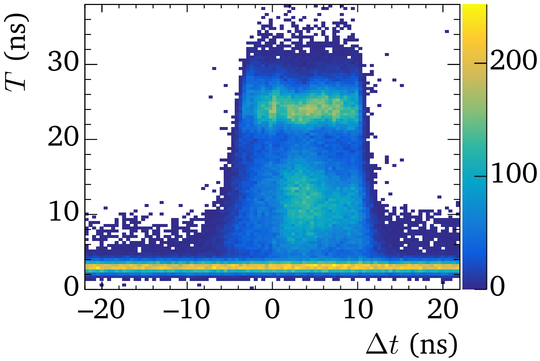

(a) Module 34.

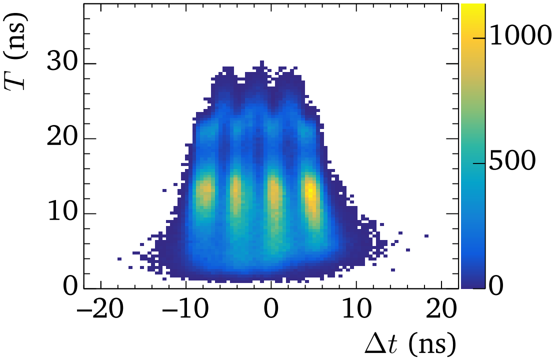

(b) Module 111.

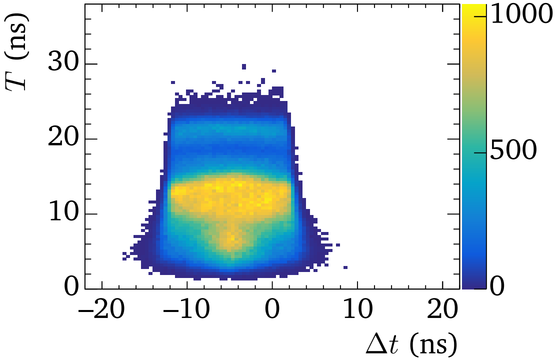

(c) Module 106.

Figure B.1.: ToT T vs. time difference Δt for the two defective modules 34 (a) and 111 (b), as well as for the correctly working module 106 (c).

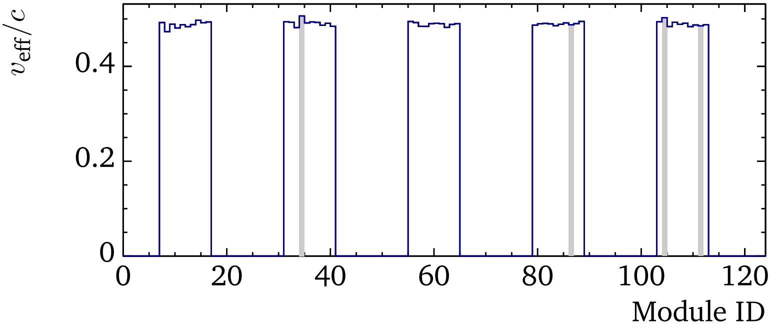

Figure B.2.: Effective velocities of light in the scintillators of the second wall of HIME JP. The defective modules are marked in gray and the corresponding velocities might be imprecise.

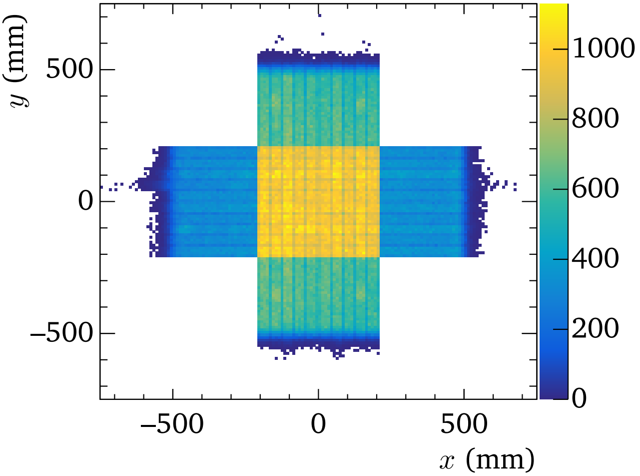

Figure B.3.: Detection positions of cosmic muons in the second wall of HIME JP.

Bibliography

[1] W. Bothe and H. Becker. “Künstliche Erregung von Kern-γ-Strahlen”. In: *Zeitschrift für Physik* 66 (1930). URL: `https://doi.org/10.1007/BF01390908`.

[2] E. Amaldi. “From the discovery of the neutron to the discovery of nuclear fission”. In: *Physics Reports* 111 (1984). URL: `https://doi.org/10.1016/0370-1573(84)90214-X`.

[3] V. V. Nesvizhevsky and J. Villain. “The discovery of the neutron and its consequences (1930–1940)”. In: *Comptes Rendus Physique* 18 (2017). URL: `https://doi.org/10.1016/j.crhy.2017.11.001`.

[4] J. Chadwick. “Possible Existence of a Neutron”. In: *Nature* 129 (1932). URL: `https://dx.doi.org/10.1038/129312a0`.

[5] W. Heisenberg. “Über den Bau der Atomkerne”. In: *Zeitschrift für Physik* 77 (1932). URL: `https://doi.org/10.1007/BF01342433`.

[6] O. Bochkarev *et al.* ““Dineutron” emission from an excited state of the ^{6}He nucleus”. In: *Jetp Letters - JETP LETT-ENGL TR* 42 (1985). URL: `https://www.researchgate.net/publication/253014949_Dineutron''_emission_from_an_excited_state_of_the_6He_nucleus`.

[7] P. G. Hansen and B. Jonson. “The Neutron Halo of Extremely Neutron-Rich Nuclei”. In: *Europhysics Letters* 4 (1987). URL: `https://doi.org/10.1209/0295-5075/4/4/005`.

[8] K. K. Seth. and B. Parker. “Evidence for Dineutrons on Extremely Neutron-Rich Nuclei”. In: *Physical Review Letters* 66 (1991). URL: `https://doi.org/10.1103/PhysRevLett.66.2448`.

[9] A. Spyrou *et al.* “First Observation of Ground State Dineutron Decay: ^{16}Be”. In: *Physical Review Letters* 108 (2012). URL: `https://doi.org/10.1103/PhysRevLett.108.102501`.

[10] F. M. Marqués *et al.* “Comment on “First Observation of Ground State Dineutron Decay: ^{16}Be””. In: *Phys. Rev. Lett.* 109 (2012). URL: `https://doi.org/10.1103/PhysRevLett.109.239201`.

[11] A. Spyrou *et al.* “Spyrou *et al.* Replies”. In: *Phys. Rev. Lett.* 109 (2012). URL: `https://doi.org/10.1103/PhysRevLett.109.239202`.

[12] D. W. Glasgow and D. G. Foster. “$n-d$ Total Cross Section, Three-Nucleon Problem, and the Dineutron”. In: *Phys. Rev.* 157 (1967). URL: `https://doi.org/10.1103/PhysRev.157.764`.

[13] B. L. Cohen and T. H. Handley. “An Experimental Search for a Stable Dineutron”. In: *Phys. Rev.* 92 (1953). URL: `https://doi.org/10.1103/PhysRev.92.101`.

[14] D. Nguyen *et al.* “Search for a bound di-neutron by comparing ^{3}He(e,$e'p$)d and ^{3}H(e,$e'p$)X measurements”. In: *Physics Letters B* 831 (2022). URL: `https://doi.org/10.1016/j.physletb.2022.137165`.

[15] H.-W. Hammer and S. König. "Constraints on a possible dineutron state from pionless EFT". In: *Physics Letters B* 736 (2014). URL: `https://doi.org/10.1016/j.physletb.2014.07.015`.

[16] F. M. Marqués and Jaume Carbonell. "The quest for light multineutron systems". In: *The European Physical Journal A* 57 (2021). URL: `https://doi.org/10.1140/epja/s10050-021-00417-8`.

[17] A. V. Belozyorov *et al.* "Search for the tri- and tetra-neutron in reactions induced by ^{11}B and ^{9}Be ions on ^{7}Li". In: *Nuclear Physics A* 477 (1988). URL: `https://doi.org/10.1016/0375-9474(88)90365-X`.

[18] H. G. Bohlen *et al.* "Study of light neutron-rich nuclei with ^{14}C-induced reactions". In: *Nuclear Physics A* 583 (1995). URL: `https://doi.org/10.1016/0375-9474(94)00757-E`.

[19] D. V. Aleksandrov *et al.* "Search for resonances in the three-and four-neutron systems in the ^{7}Li(^{7}Li, ^{11}C)3n and ^{7}Li(^{7}Li, ^{10}C)4n reactions". In: *Journal of Experimental and Theoretical Physics Letters* 81 (2005). URL: `https://doi.org/10.1134/1.1887912`.

[20] I. Tanihata. "Nuclear Physics with RIB's: How it all started". In: *The European Physics Journal Plus* 131 (2016). URL: `https://doi.org/10.1140/epjp/i2016-16090-x`.

[21] F. M. Marqués *et al.* "Detection of neutron clusters". In: *Phys. Rev. C* 65 (2002). URL: `https://doi.org/10.1103/PhysRevC.65.044006`.

[22] F. M. Marqués *et al.* "On the possible detection of 4n events in the breakup of ^{14}Be". In: *arXiv:nucl-ex/0504009v1* (2005).

URL: https://doi.org/10.48550/arXiv.nucl-ex/0504009.

[23] K. Kisamori *et al.* “Candidate Resonant Tetraneutron State Populated by the ^{4}He(^{8}He,^{8}Be) Reaction”. In: *Physical Review Letters* 116 (2016). URL: https://doi.org/10.1103/PhysRevLett.116.052501.

[24] M. Duer *et al.* “Observation of a correlated free four-neutron system”. In: *Nature* 606 (2022). URL: https://doi.org/10.1038/s41586-022-04827-6.

[25] R. Lazauskas, E. Hiyama, and J. Carbonell. “Low Energy Structures in Nuclear Reactions with $4n$ in the Final State”. In: *Phys. Rev. Lett.* 130 (2023). URL: https://doi.org/10.1103/PhysRevLett.130.102501.

[26] J. R. Taylor. *Scattering Theory: The Quantum Theory of Nonrelativistic Collisions*. Dover Publications, Inc., 2006.

[27] C. S. Wu *et al.* “Experimental Test of Parity Conservation in Beta Decay”. In: *Phys. Rev.* 105 (1957). URL: https://doi.org/10.1103/PhysRev.105.1413.

[28] M. R. Schindler and R. P. Springer. “The theory of parity violation in few-nucleon systems”. In: *Progress in Particle and Nuclear Physics* 72 (2013). URL: https://doi.org/10.1016/j.ppnp.2013.05.002.

[29] J. Schwinger. “Minutes of the Meeting at Stanford University, California July 11-12, 1947”. In: *Phys. Rev.* 72 (1947). Section: A Variational Principle for Scattering Problems. URL: https://doi.org/10.1007/BF01342433.

[30] J. M. Blatt. “On the Neutron-Proton-Force”. In: *Physical Review C* 74 (1948). URL: https://doi.org/10.1103/PhysRev.74.92.

[31] Q. Chen *et al.* “Measurement of the neutron-neutron scattering length using the $\pi^- d$ capture reaction”. In: *Physical Review C* 77 (2008). URL: `https://doi.org/10.1103/PhysRevC.77.054002`.

[32] A. V. Manohar, L. P. Lellouch, and R. M. Barnett. “Quark Masses”. In: *Review of Particle Physics* (2019). URL: `https://doi.org/10.1093/ptep/ptaa104`.

[33] P. A. Zyla *et al.* “Review of Particle Physics”. In: *Prog. Theor. Exp. Phys.* 2020 (2020). URL: `https://doi.org/10.1093/ptep/ptaa104`.

[34] A. Gårdestig. “Extracting the neutron–neutron scattering length—recent developments”. In: *Journal of Physics G: Nuclear and Particle Physics* 36 (2009). URL: `https://doi.org/10.1088/0954-3899/36/5/053001`.

[35] G. Breit and E. Feenberg. “The Possibility of the Same Form of Specific Interaction for All Nuclear Particles”. In: *Phys. Rev.* 50 (1936). URL: `https://doi.org/10.1103/PhysRev.50.850`.

[36] G. A. Miller and W. T. H. van Oers. “Charge Independence and Charge Symmetry”. In: *Symmetries and Fundamental Interactions in Nuclei* (1995). URL: `https://doi.org/10.1142/9789812831446_0005`.

[37] R. Machleidt and I. Slaus. “The nucleon-nucleon interaction”. In: *Journal of Physics G: Nuclear and Particle Physics* 27 (2001). URL: `https://doi.org/10.1088/0954-3899/27/5/201`.

[38] J. R. Bergervoet *et al.* “Phase shift analysis of 0–30 MeV pp scattering data”. In: *Phys. Rev. C* 38 (1988). URL: `https://doi.org/10.1103/PhysRevC.38.15`.

[39] G. A. Miller, B. M. K. Nefkens, and I. Šlaus. “Charge symmetry, quarks and mesons”. In: *Physics Reports* 194 (1990). URL: `https://doi.org/10.1016/0370-1573(90)90102-8`.

[40] C. R. Howell. “Review of Indirect Methods Used to Determine the $^1S_0$ Neutron-Neutron Scattering Length”. In: *arXiv:1010.0632v1* (2008). URL: `https://doi.org/10.48550/arXiv.0805.1177`.

[41] B. Gabioud *et al.* “$n - n$ Scattering Length from the Photon Spectra of the Reactions $\pi^- d \to \gamma nn$ and $\pi^- p \to \gamma n$”. In: *Phys. Rev. Lett.* 42 (1979). URL: `https://doi.org/10.1103/PhysRevLett.42.1508`.

[42] B. Gabioud *et al.* “nn Scattering parameters a_{nn} and r_{nn} from the photon spectrum of the reaction $\pi^- d \to \gamma nn$”. In: *Nuclear Physics A* 420 (1984). URL: `https://doi.org/10.1016/0375-9474(84)90669-9`.

[43] O. Schori *et al.* “Measurement of the neutron-neutron scattering length a_{nn} with the reaction $\pi^-\mathrm{d} \to \mathrm{nn}\gamma$ in complete kinematics”. In: *Phys. Rev. C* 35 (1987). URL: `https://doi.org/10.1103/PhysRevC.35.2252`.

[44] C. R. Howell *et al.* “Toward a resolution of the neutron-neutron scattering-length issue”. In: *Physics Letters B* 444 (1998). URL: `https://doi.org/10.1016/S0370-2693(98)01386-0`.

[45] D. E. González Trotter *et al.* “New Measurement of the $^1S_0$ Neutron-Neutron Scattering Length Using the Neutron-Proton Scattering Length as a Standard”. In: *Phys. Rev. Lett.* 83 (1999). URL: `https://doi.org/10.1103/PhysRevLett.83.3788`.

[46] D. E. González Trotter *et al.* “Neutron-deuteron breakup experiment at $E_n = 13\,\text{MeV}$: Determination of the ${}^1S_0$ neutron-neutron scattering length a_{nn}”. In: *Physical Review C* 736 (2006). URL: `https://doi.org/10.1103/PhysRevC.73.034001`.

[47] V. Huhn *et al.* “New Attempt to Determine the $n{-}n$ Scattering Length with the ${}^2\text{H}(n, np)n$ Reaction”. In: *Phys. Rev. Lett.* 85 (2000). URL: `https://doi.org/10.1103/PhysRevLett.85.1190`.

[48] V. Huhn *et al.* “New investigation of the neutron-neutron and neutron-proton final-state interaction in the n-d breakup reaction”. In: *Phys. Rev. C* 63 (2000). URL: `https://doi.org/10.1103/PhysRevC.63.014003`.

[49] W. von Witsch, X. Ruan, and H. Witała. “Neutron-neutron final-state interaction in the ${}^2\text{H}(n, p)2n$ reaction at $E_n = 17.4$ MeV”. In: *Phys. Rev. C* 74 (2006). URL: `https://doi.org/10.1103/PhysRevC.74.014001`.

[50] T. Aumann. *Determination of the nn scattering length from a high-resolution measurement of the nn relative-energy spectrum produced in the* ^{6}*He(p,p*α*)*^{2}*n, t(p,2p)*^{2}*n and d(*^{7}*Li,* ^{7}*Be)* ^{2}*n reactions*. Proposal for an experiment at RIBF, Proposal No. NP2012-SAMURAI55R1. 2020.

[51] M. Göbel *et al.* “Neutron-neutron scattering length from the ${}^6\text{He}(p,p\alpha)nn$ reaction”. In: *Phys. Rev. C* 104 (2021). URL: `https://doi.org/10.1103/PhysRevC.104.024001`.

[52] P. F. Bedaque, H.-W. Hammer, and U. van Kolck. “Effective theory of the triton”. In: *Nuclear Physics A* 676 (2000). URL: `https://doi.org/10.1016/S0375-9474(00)00205-0`.

[53] H.-W. Hammer, C. Ji, and D. R. Phillips. “Effective field theory description of halo nuclei”. In: *Journal of Physics G: Nuclear and Particle Physics* 44 (2017). URL: `https://doi.org/10.1088/1361-6471/aa83db`.

[54] D. R. Tilley, H. R. Weller, and G. M. Hale. “Energy levels of light nuclei $A = 4$”. In: *Nuclear Physics A* 541 (1992). URL: `https://doi.org/10.1016/0375-9474(92)90635-W`.

[55] M. Wang *et al.* “The AME 2020 atomic mass evaluation (II). Tables, graphs and references”. In: *Chinese Physics C* 45 (2021). URL: `https://doi.org/10.1088/1674-1137/abddaf`.

[56] I. J. Thompson, F. M. Nunes, and B. V. Danilin. “FaCE: a tool for three body Faddeev calculations with core excitation”. In: *Computer Physics Communications* 161 (2004). URL: `https://doi.org/10.1016%2Fj.cpc.2004.03.007`.

[57] Wang M. *et al.* “The AME 2012 atomic mass evaluation”. In: *Chinese Physics C* 36 (2012). URL: `https://dx.doi.org/10.1088/1674-1137/36/12/003`.

[58] P. F. Bedaque *et al.* “Low energy expansion in the three body system to all orders and the triton channel”. In: *Nuclear Physics A* 714 (2003). URL: `https://doi.org/10.1016/S0375-9474(02)01402-1`.

[59] H. Sakurai. “RI Beam Factory Project at RIKEN”. In: *Nuclear Physics A* 805 (2008). URL: `https://doi.org/10.1016/j.nuclphysa.2008.02.291`.

[60] Website about technical information of the RIBF accelerator. URL: `https://www.nishina.riken.jp/RIBF/accelerator/tecinfo.html`. Visited: 2022-04-01.

[61] T. Ohnishi *et al.* “Identification of New Isotopes ^{125}Pd and ^{126}Pd Produced by In-Flight Fission of 34 MeV/nucleon ^{238}U: First Results from the RIKEN RI Beam Factory”. In: *Journal of the Physical Society of Japan* 77 (2008). URL: `https://doi.org/10.1143/JPSJ.77.083201`.

[62] Y. Yano. “The RIKEN RI Beam Factory Project: A status report”. In: *Nuclear Instruments and Methods in Physics Research Section B: Beam Interactions with Materials and Atoms* 261 (2007). URL: `https://doi.org/10.1016/j.nimb.2007.04.174`.

[63] Schematic drawing of RIBF at RIKEN. URL: `https://ribf.riken.jp/intds2014/location/images/CG_bird.jpg`. Visited: 2022-06-15.

[64] T. Kubo. “In-flight RI beam separator BigRIPS at RIKEN and elsewhere in Japan”. In: *Nuclear Instruments and Methods in Physics Research Section B: Beam Interactions with Materials and Atoms* 204 (2003). URL: `https://doi.org/10.1016/S0168-583X(02)01896-7`.

[65] T. Kobayashi *et al.* “SAMURAI spectrometer for RI beam experiments”. In: *Nuclear Instruments and Methods in Physics Research Section B* 317 (2013). URL: `https://doi.org/10.1016/j.nimb.2013.05.089`.

[66] Y. Shimizu *et al.* “SAMURAI Project at RIBF”. In: *Journal of Physics: Conference Series* 312 (2011). URL: `https://doi.org/10.1088%2F1742-6596%2F312%2F5%2F052022`.

[67] K. Miki. *Correlations in multi-neutron systems*. Proposal for an experiment at RIBF, Proposal No. NP2022-SAMURAI74. 2022.

[68] K. Kusaka *et al.* “Prototype of superferric quadrupole magnets for the BigRIPS separator at RIKEN”. In: *IEEE Transactions on

Applied Superconductivity 14 (2004). URL: `https://doi.org/10.1109/TASC.2004.829102`.

[69] T. Uesaka and J. Zenihiro. *TOGAXSI: a new setup for inverse-kinematics cluster and nucleon knock-out reaction experiments*. Construction proposal. 2021.

[70] L. V. Chulkov *et al.* "Quasi-free scattering with ^{6,8}He beams". In: *Nuclear Physics A* 759 (2005). URL: `https://doi.org/10.1016/j.nuclphysa.2005.05.148`.

[71] H. Sato *et al.* "Superconducting Dipole Magnet for SAMURAI Spectrometer". In: *IEEE Transactions on Applied Superconductivity* 23 (2013). URL: `https://doi.org/10.1109/TASC.2012.2237225`.

[72] Y. Shimizu *et al.* "Vacuum system for the SAMURAI spectrometer". In: *Nuclear Instruments and Methods in Physics Research Section B: Beam Interactions with Materials and Atoms* 317 (2013). URL: `https://doi.org/10.1016/j.nimb.2013.08.051`.

[73] Y. Kondo *et al.* "NEBULA (Neutron Detection System for Breakup of Unstable Nuclei with Large Acceptance)". In: *RIKEN Accelerator Progress Report* 44 (2011). URL: `https://www.nishina.riken.jp/researcher/APR/Document/ProgressReport_vol_44.pdf`.

[74] Y. Kondo *et al.* "Calibration methods of the neutron detector array NEBULA". In: *RIKEN Accelerator Progress Report* 45 (2012). URL: `https://www.nishina.riken.jp/researcher/APR/Document/ProgressReport_vol_45.pdf`.

[75] *Eljen Technology, 1300 W. Broadway, Sweetwater, TX 79556, USA*. URL: `https://eljentechnology.com/`.

[76] *Saint-Gobain Crystals, 17900 Great Lakes Parkway, Hiram, OH 44234-9681, USA*. URL: `https://www.crystals.saint-gobain.com/#`.

[77] O. B. Tarasov and D. Bazin. "LISE++: Radioactive beam production with in-flight separators". In: *Nuclear Instruments and Methods in Physics Research Section B: Beam Interactions with Materials and Atoms* 266 (2008). URL: `https://doi.org/10.1016/j.nimb.2008.05.110`.

[78] G. A. Moss *et al.* "Proton-^{4}He elastic scattering at intermediate energies". In: *Phys. Rev. C* 21 (1980). URL: `https://doi.org/10.1103/PhysRevC.21.1932`.

[79] A. A. Galyuzov and M. V. Kosov. "Approximation of Differential Cross Sections for Elastic Proton-Nucleus Scattering". In: *Physics of Atomic Nuclei* 84 (2021). URL: `https://doi.org/10.1134/S1063778821040128`.

[80] P. Schwaller *et al.* "Proton total cross sections on 1H, 2H, 4He, 9Be, C and O in the energy range 180 to 560 MeV". In: *Nuclear Physics A* 316 (1979). URL: `https://doi.org/10.1016/0375-9474(79)90040-X`.

[81] M. Göbel. *Private communication*. 2023.

[82] T. Isobe. *Anaroot webpage*. URL: `https://ribf.riken.jp/RIBFDAQ/index.php?Tools%2FAnalysis%2FANAROOT`. Visited: 2021-12-14.

[83] S. Agostinelli *et al.* "Geant4—a simulation toolkit". In: *Nuclear Instruments and Methods in Physics Research Section A: Accelerators, Spectrometers, Detectors and Associated Equipment* 506 (2003). URL: `https://doi.org/10.1016/S0168-9002(03)01368-8`.

[84] J. Allison *et al.* “Geant4 developments and applications”. In: *IEEE Transactions on Nuclear Science* 53 (2006). URL: `https://doi.org/10.1109/TNS.2006.869826`.

[85] J. Allison *et al.* “Recent developments in Geant4”. In: *Nuclear Instruments and Methods in Physics Research Section A: Accelerators, Spectrometers, Detectors and Associated Equipment* 835 (2016). URL: `https://doi.org/10.1016/j.nima.2016.06.125`.

[86] S. Leray *et al.* “Extension of the Liège Intra Nuclear Cascade model to light ion-induced collisions for medical and space applications”. In: *Journal of Physics: Conference Series* 420 (2013). URL: `https://dx.doi.org/10.1088/1742-6596/420/1/012065`.

[87] D. H. Wright and M. H. Kelsey. “The Geant4 Bertini Cascade”. In: *Nuclear Instruments and Methods in Physics Research Section A: Accelerators, Spectrometers, Detectors and Associated Equipment* 804 (2015). URL: `https://doi.org/10.1016/j.nima.2015.09.058`.

[88] J. Apostolakis *et al.* “Geometry and physics of the Geant4 toolkit for high and medium energy applications”. In: *Radiation Physics and Chemistry* 78 (2009). URL: `https://doi.org/10.1016/j.radphyschem.2009.04.026`.

[89] R. Brun and F. Rademakers. “ROOT - An Object Oriented Data Analysis Framework”. In: *Nuclear Instruments and Methods in Physics Research Section A* 389 (1997). URL: `https://root.cern.ch`.

[90] SAMURAI magnet field maps. URL: `https://ribf.riken.jp/SAMURAI/index.php?Magnet`. Visited: 2023-05-11.

[91] M. Knösel. “Investigation of the Dineutron System via Quasi-Free ^{4}He-Knockout Reactions at ^{6}He”. MA thesis. TU Darmstadt, 2019.

[92] T. Nakamura and Y. Kondo. “Large acceptance spectrometers for invariant mass spectroscopy of exotic nuclei and future developments”. In: *Nuclear Instruments and Methods in Physics Research Section B* 376 (2016). URL: `https://doi.org/10.1016/j.nimb.2016.01.003`.

[93] J. Mayer. “Charting NeuLAND: Towards multi-neutron reconstruction with the New Large Area Neutron Detector and The virtual γ-ray spectrometer G4Horus”. PhD thesis. Universität zu Köln, 2018. URL: `https://kups.ub.uni-koeln.de/id/eprint/24865`.

[94] G. D’Agostini. “A multidimensional unfolding method based on Bayes’ theorem”. In: *Nuclear Instruments and Methods in Physics Research Section A: Accelerators, Spectrometers, Detectors and Associated Equipment* 362 (1995). URL: `https://doi.org/10.1016/0168-9002(95)00274-X`.

[95] G. D’Agostini. “Improved iterative Bayesian unfolding”. In: *arXiv:1010.0632v1* (2010). URL: `https://doi.org/10.48550/arXiv.1010.0632`.

[96] *Proceedings of the PHYSTAT 2011 Workshop on Statistical Issues Related to Discovery Claims in Search Experiments and Unfolding: CERN, Geneva, Switzerland 17 - 20 Jan 2011. PHYSTAT 2011 Workshop on Statistical Issues Related to Discovery Claims in Search Experiments and Unfolding*. CERN, 2011. URL: `https://doi.org/10.5170/CERN-2011-006`.

[97] *Hamamatsu Photonics K. K., 325-6, Sunayama-cho, Naka-ku, Hamamatsu City, Shizuoka Pref., 430-8587, Japan*. URL: `https://www.hamamatsu.com/`.

[98] A. Rost *et al.* “A flexible FPGA based QDC and TDC for the HADES and the CBM calorimeters”. In: *Journal of Instrumentation* 12 (2017). URL: `https://doi.org/10.1088/1748-0221/12/02/c02047`.

[99] M. Traxler *et al.* “A compact system for high precision time measurements ($<$ 14 ps RMS) and integrated data acquisition for a large number of channels”. In: *Journal of Instrumentation* 6 (2011). URL: `https://doi.org/10.1088/1748-0221/6/12/c12004`.

[100] C. Ugur *et al.* “A novel approach for pulse width measurements with a high precision (8 ps RMS) TDC in an FPGA”. In: *Journal of Instrumentation* 11 (2016). URL: `https://doi.org/10.1088/1748-0221/11/01/c01046`.

[101] J. Adamczewski-Musch *et al.* “Data acquisition and online monitoring software for CBM test beams”. In: *Journal of Physics: Conference Series* 396 (2012). URL: `https://dx.doi.org/10.1088/1742-6596/396/1/012001`.

[102] J. Adamczewski-Musch, B. Bellenot, and S. Linev. *Web interface for online ROOT and DAQ applications*. 2014. URL: `https://doi.org/10.1109/RTC.2014.7097456`.

[103] J. Adamczewski-Musch *et al.* “HADES trbnet data formats for DABC and Go4”. In: *GSI Report* 2013-1 (2013). URL: `https://repository.gsi.de/record/52192`.

[104] J. J. Beatty, J. Matthews, and S. P. Wakely. “Cosmic Rays”. In: *Review of Particle Physics* (2021). URL: `https://doi.org/10.1093/ptep/ptaa104`.

[105] D. E. Groom, N. V. Mokhov, and S. I. Striganov. “Muon stopping power and range tables 10 MeV–100 TeV”. In: *Atomic Data and*

Nuclear Data Tables 78 (2001). URL: `https://doi.org/10.1006/adnd.2001.0861`.

List of Acronyms

BDC	Beam drift chamber
BigRIPS	Big RIKEN projectile fragment separator
CM	Center of mass
CPVeto	Charged particle veto detector
CS	Charge symmetry
CSB	Charge symmetry breaking
CTS	Central trigger system
DABC	Data acquistion backbone core
DAQ	Data acquisition
DFG	Deutsche Forschungsgemeinschaft
ECR	Electron cyclotron resonance
EFT	Effective field theory
ERE	Effective range expansion
FaCE	Faddeev with core excitation
FDC	Forward drift chamber
FPGA	Field programmable gate array
fRC	Fixed-frequency ring cyclotron

FSI	Final state interaction
GAGG:Ce	Gadolinium aluminium gallium garnet doped with cerium
Geant	Geometry and tracking
Go4	GSI object oriented on-line off-line system
GSI	Gesellschaft für Schwerionenforschung
hEFT	Halo effective field theory
HGS-HIRe	Helmholtz Graduate School for Hadron and Ion Research
HIME	High-resolution detector array for multi-neutron events
HIME DE	German part of HIME
HIME JP	Japanese part of HIME
HLD	HADES list mode data (*HADES is the “high-acceptance dielectron spectrometer” at GSI.*)
IKP	Institut für Kernphysik
IRC	Intermediate ring cyclotron
ISOL	Isotope separation on line
LISE^{++}	Ligne d’ions super epluchés; *Software package named after an achromatic spectrometer at the “Grand Accélérateur National d’Ions Lourds” (GANIL)*
MIP	Minimum ionizing particle

NEBULA	Neutron detection system for breakup of unstable nuclei with large acceptance
PaDiWa	PANDA DIRC WASA (*experimental setups at GSI*)
PMT	Photomultiplier tube
QDC	Charge-to-digital converter
QFS	Quasi-free scattering
QGSP_BERT_XS	Quark gluon string model, Geant4 precompound de-excitation model, Bertini cascade; *XS indicates additional libraries for neutron propagation*
QGSP_INCLXX_XS	Quark gluon string model, Geant4 Precompound de-excitation model, Liège intranuclear cascade model, C++; *XS indicates additional libraries for neutron propagation*
RIB	Radioactive ion beam
RIBF	Radioactive Ion Beam Factory
RIKEN	Rikagaku Kenkyūjo
RILAC	RIKEN linear accelerator
RRC	RIKEN ring cyclotron
SAMURAI	Superconducting analyzer for multi particles from radioisotope beams
SBT	Scintillators for beam time-of-flight
SFB	Sonderforschungsbereich
SRC	Superconducting ring cyclotron
SSD	Silicon strip detector

STQ	Superconducting triplet quadrupole
TDC	Time-to-digital converter
ToF	Time of flight
TOGAXSI	Total energy measurement by GaGG and vertex measurement by Si strips
ToT	Time over threshold
TRB	TDC readout board
TUNL	Triangle Universities National Laboratory

Acknowledgements

The final chapter is dedicated to my colleagues, friends, and family members, who all supported me and thereby made this work possible in the first place. Thus, I would like to thank:

- **Prof. Dr. Thomas Aumann** for giving me the opportunity to follow my Master's degree and later my doctorate in the highly interesting and aspiring research field of nuclear structure physics. I am thankful for all the support and helpful discussions that accompanied my work over the past years, as well as for giving me the possibility to travel to conferences and experiments to various places around the world, which widened my perspective on both scientific and cultural aspects.

- **Priv.-Doz. Dr. H. Scheit** for the support concerning computer and server infrastructure, thereby strongly increasing my productivity and simplifying my work.

- **Dr. Dominic Rossi** and **Dr. Meytal Duer**, as I could not have wished for a better working atmosphere in our small HIME team. I always enjoyed the common work, even (or, especially) during extensive debugging sessions at our test setups. Furthermore, the proofreading was highly valuable for the development of this thesis.

I see forward very much to our future work on and with HIME.

- **Dr. Vadim Wagner** for his valuable IT and programming tips that helped me to increase my productivity and to write more efficient and better readable code.
- the other members of AG Aumann for the friendly working atmosphere.
- **Prof. Alexandre Obertelli, Ph.D.,** for taking so much interest in the development of my work, for good questions and challenging discussions that made me think more clearly about many details.
- **Matthias Göbel** from the theory center of IKP for our discussions about non-relativistic quantum mechanical scattering, as well as for providing results of his hEFT calculations and the helpful explanations that always came along with the data, which gave me interesting insights in the theoretical counterpart of my work and made it possible to learn more from my simulations.
- **Dr. Michael Traxler** from GSI for his comprehensive support concerning the setup and the usage of the versatile TRB3 system.
- **Dr. Jan Michel** from Goethe Universität Frankfurt for helping us to set up the trigger system on our TRB3 boards.
- our colleagues from the SAMURAI team in Japan for the collaborative work as well as the welcoming and friendly support at RIKEN.
- my friends who distracted me from work whenever necessary.
- my parents **Gabriele** and **Friedrich** as well as my brother **Daniel** for

their unrelenting support since so many years, making it possible for me to follow and enjoy my academic career until today.

Funding

This work is supported by:

- the Deutsche Forschungsgemeinschaft (DFG) through grant No. “Sonderforschungsbereich (SFB) 1245”, Project-ID 279384907, and
- the “Helmholtz Graduate School for Hadron and Ion Research” (HGS-HIRe).